Doctoral Dissertation

Investigation on bulk-scale synthesis and application of randomly stacked multilayer graphene with high crystallinity

Zizhao Xu

May 2023

Department of Applied Physics

Graduate School of Engineering

Osaka University

Supervisor: Prof. Yoshihiro Kobayashi

Abstract

Since the strong interlayer interaction of AB-stacked graphene in bulk form degrades the superior property of single-layer graphene, the formation of randomly stacked graphene is required to apply the high performance of graphene to macroscopic devices. However, conventional methods to obtain bulk-scale graphene suffer from a low crystallinity and/or the formation of a thermodynamically stable AB-stacked structure.

The first part of this dissertation develops a novel approach to produce bulk-scale graphene with a high crystallinity and high fractions of random stacking by utilizing the porous morphology of graphene oxide (GO) sponge and an ultrahigh temperature treatment of 1500−1800 °C with ethanol vapor. Raman spectroscopy indicates that the obtained bulk-scale graphene sponge possesses a high crystallinity and a high fraction of random stacking of 80%. The large difference in the random-stacking fraction between the sponge and the aggregate samples confirms the importance of the accessibility of ethanol-derived species into the internal area. By investigating the effect of treatment temperature, a higher random-stacking fraction is obtained at 1500 °C. Moreover, the AB-stacking fraction was reduced to less than 10% by introducing cellulose nanofiber as a spacer to prevent direct stacking of graphene.

The second part of this dissertation provided a promising approach to prevent the strong interlayer interaction is the staking order reduction of graphene, where the graphene layers are rotated in-plane to form a randomly stacking structure. To effectively decrease the stacking order of multilayer graphene, nanospacers, cellulose nanofibers or nano-diamonds (NDs), was incorporated in a formation process of porous graphene sponges and formed mixed-dimensional heterostructures. This study conducted an ultrahigh temperature treatment at 1500 ℃ with ethanol vapor for the reduction and structural repair of graphene oxide sponges with different concentrations of the nanospacers. Raman spectroscopy indicated an obvious increase in the random-stacking fraction of graphene by adding nanospacers. The X-ray diffraction (XRD) analysis revealed that a small amount of the nanospacers induced a remarkable decrease of ordered graphene crystalline size in the stacking direction. It was also confirmed that a layer-number increase during the thermal treatment was suppressed by the nanospacers. The increase in the random stacking fraction is attributed to the efficient formation of randomly rotated graphene through the ethanol-mediated structural

restoration of relatively thin layers induced by the nanospacers. This stacking-order-reduced graphene with bulk scale is expected to be used in macroscopic applications, such as electrode materials and wearable devices.

In the third part of this dissertation, the reduced graphene oxide (rGO) and the rGO/ND sponge were employed as strain sensors. Graphene shows promise as an alternative material for strain sensors, due to its excellent properties, which can overcome the limitations of conventional metal ones. However, current graphene-based strain sensors were fabricated from chemically rGO and suffered from low linearity and large hysteresis in sensor response as well as high initial resistance. These issues should be caused by functional groups and defects remaining on the rGO. Herein, highly crystalline rGO is employed for the fabrication of the strain sensor. The porous rGO sponge with low defect density is prepared in bulk scale via the ethanol-associated thermal process at ultra-high temperature. The obtained rGO sensor exhibits improved linearity, low initial resistance, and very small hysteresis owing to the high crystallinity of the rGO. Composite of rGO with ND, which has a role as nanospacer to separate the rGO layers, is found to be very effective to enhance the sensitivity.

Table of Contents

Chapter 1: Introduction

1.1 Properties of graphene

This decade witnesses that graphene has attracted worldwide attention for its various excellent properties, such as high carrier mobility, electrochemical performance [1], optical transparency [2], thermal conductivity [3], and mechanical strength [4-6]. A number of these properties can be attributed to a honeycomb lattice of one-atom-thick single-layer graphene. In this honeycomb lattice, each carbon atom was first connected by a σ-bonds to each of the three adjacent carbon atoms and then formed a π-bond outside the plane.

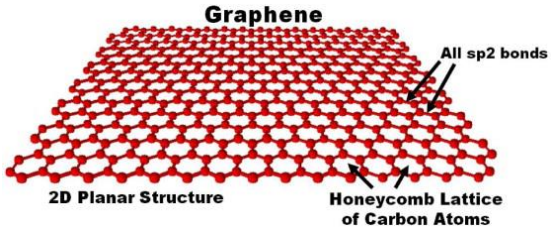

Figure 1.1 Graphene is an atomic-scale honeycomb lattice consisting of sp^2-hybridized carbon atoms [7].

Graphene is a two-dimensional material, which is easy to stack into multilayer graphene. There are two main types of stacking structures: AB stacking and random stacking [8, 9]. AB stacking is a stable structure for multilayer graphene [10], in which the carbon atoms in the lower layer are overlapped by the center of the honeycomb of the upper layer [11]. However, the AB stacking causes the degradation of excellent electronic properties of single-layer graphene, because a band gap emerges, which is similar to that of graphite [12]. On the other hand, the random stacking structure is the upper and lower layers of graphene are overlapped with a random angle. It has been reported that random stacking graphene can maintain the electronic properties of single-layer graphene and its excellent electrical properties, as its electrons have a linear distribution around the Dirac point [11].

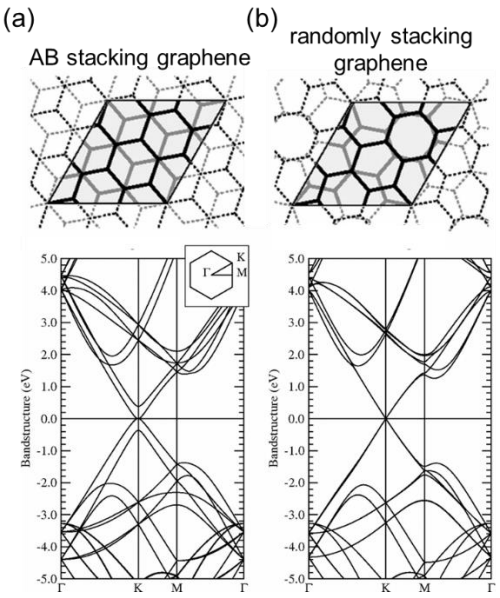

Figure 1.2 2D electronic band structures of (a) AB-stacked multilayer graphene and (b) randomly stacked multilayer graphene [11].

1.2 Application of bulk-scale graphene

In recent years, graphene has gained considerable attention due to its exceptional physical properties, which are attributed to its unique electronic structure. Due to its structure, graphene is a material with excellent electrical and mechanical properties [1, 6], making it an ideal material for a wide range of applications. As research on graphene properties and applications advances, its potential is increasingly being explored, particularly in strain sensors [13, 14], as well as in batteries [15, 16], supercapacitors [17, 18], and others.

1.2.1 Strain sensor

The conventional strain sensors suffer from low sensitivity and insufficient stretching rates [19], making them incapable of meeting the demands of modern life. Graphene and its derivatives have been extensively studied for application in the conductor in sensors, because of their high flexibility, sensitivity, and lightweight [20].

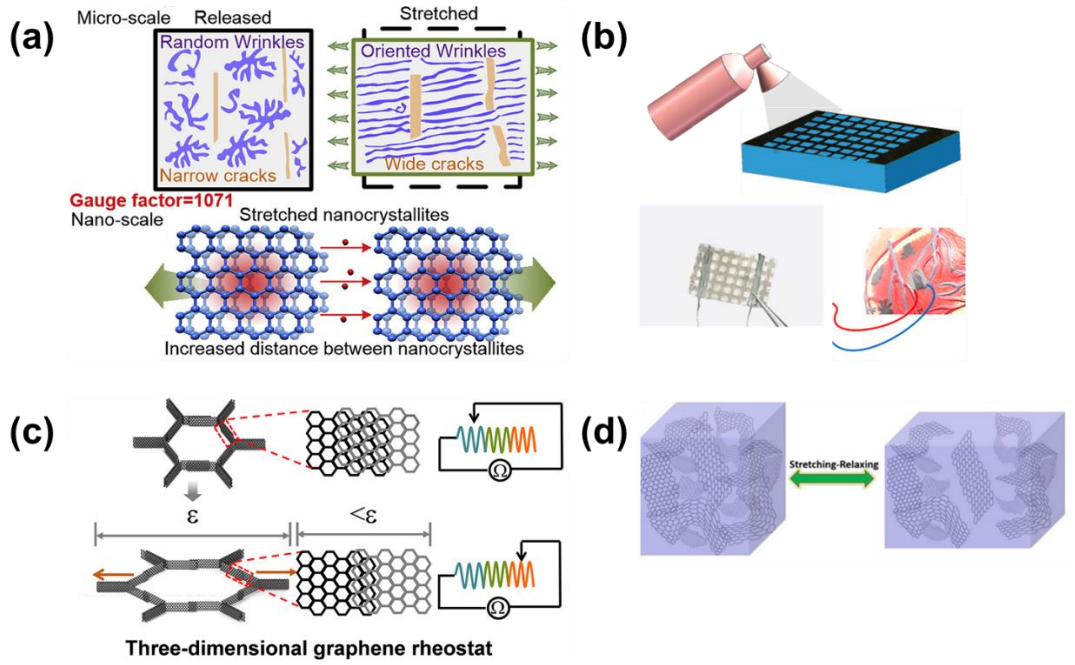

Figure 1.3 Graphene-based strain sensor with (a) film-shape [21], (b) pattern-shape [22], (c) sponge-shape [23], and (d) block-shape [24].

Peidong X. et al. [21] have developed a highly flexible and ultra-sensitive film-shape strain sensor that can detect various movements of the human body, as shown in Fig. 1.3 (a). This was achieved through the use of a graphene nanocrystallite carbon film with a wrinkled structure, which resulted in an ultra-high gauge factor (GF) of 1071 and a maximum strain of 15%. Also, the sensor has a fast response time. This strain sensor is supposed to be applied in monitoring human movements.

Wei X. et al. [22] have proposed a simple method for fabricating highly sensitive and fast-responding flexible graphene strain sensors with pattern-shape, as shown in Fig. 1.3 (b). They achieved high performance by enhancing the interface interaction of graphene with the substrate and patterning the sensitive layer of graphene on flexible PETs. The flexible strain sensor achieved high sensitivity (GF of about 100 at 1% strain), fast response (response time: 400−700 ms), and good stability (1000 cycles). These properties make it ideal for application in human health assessment, flexible electronics, and monitoring human movements.

Jing R. et al. [23] have fabricated a sponge-shape strain sensor by assembling partially overlapped graphene flakes, as shown in Fig. 1.3 (c). The key to achieving exceptional stability of the strain sensor is controlling the local sliding of the graphene

flakes to control the change in electrical resistance, as a dynamic structure resembling a sliding resistor. The strain sensor was tested for durability up to 300,000 cycles, and showed stability over a temperature range of -45 °C to 180 °C and a frequency range of 0.1 to 5 Hz, with a stretchability of 70% of the human activity range. The "sliding resistor" mechanism of graphene provides a direct route for tailoring sensing properties to meet the requirements of different applications. The methodologies developed in this study for materials preparation and strain sensor device construction/integration can be applied to the development of various new multifunctional sensing devices, including robotic skins, prosthetics, and wearable electronics.

Jinhui L. et al. [24] have reported on a highly stretchable and sensitive strain sensor with block-shape, based on a composite material consisting of graphene foam and infiltrated polydimethylsiloxane (PDMS), as shown in Fig. 1.3 (d). The composite material is characterized by excellent mechanical properties, which can be attributed to the penetration of PDMS monomers into the foam. It has a GF of 98.66 at 5% strain, and can be stretched up to 30% of its original length. Moreover, long-term stability tests have confirmed the durability of the sensor. These results indicate that the sensor has promising applications, particularly in biomechanical systems and human-computer interaction applications.

Accordingly, the strain sensors with sponge shape are the most promising method for the high stretchability, but the issues of high initial resistance, high hysteresis, and low sensitivity are required to solve. These problems can be addressed by the production of bulk-scale graphene with low defect density. However, they are hard to be simultaneously achieved by conventional graphene preparation methods, such as chemical vapor deposition and reduction of graphene oxide.

1.2.2 Other applications

Graphene also has some other potential applications, such as battery, supercapacitor, conductive ink, shielding effect, and organic contaminant removal, as listed in Table 1.1.

Table 1.1 Applications of graphene and its advantages.

Application	Properties	Advantages	ref
Na-ion battery	227.8 mAh g^{-1} at 5 A g^{-1}	sodium ion diffusion in the stacking direction of graphene	[25]
Supercapacitor	A specific area capacitance of 36.46 mF cm^{-2}	layer-by-layer microelectrodes with mechanical properties	[26]
Conductive ink	a maximum conductivity of 2.0×10^5 S m^{-1}	Reduce the cost of silver	[27]
Shielding effect	36 dB	High durability and less reflection of waves	[28]
Thermal conductive material	Thermal conductivity of 41.2 W m^{-1} K^{-1}	Heat dissipation and heating capability	[29]
Organic contaminant removal	-	High adsorption, which is not hindered by co-contamination.	[30]

Tao L. et al. [25] have resolved the difficulty of sodium ion diffusion in the vertical direction within the battery by pore-forming engineering in the graphene and using in situ growth of Co_3Se_4 nanoparticles, as shown in Fig. 1.4 (a). This design also prevents the aggregation of Co_3Se_4 nanoparticles on the graphene due to their high affinity. In subsequent full-cell tests, the battery of Co_3Se_4/holey graphene exhibited remarkable rate performance of 227.8 mAh g^{-1} at 5 A g^{-1} and ideal cycling stability (446.7 mAh g^{-1} over 500 cycles at 1.0 A g^{-1}), as shown in Fig. 1.4 (b).

Lifeng W et al. [26] have created a spatial-interleaving supercapacitor (SI-SC) that addresses the issue of limited mechanical properties in conventional supercapacitors by using a layer-by-layer stacking method of graphene microelectrodes, as shown in Fig. 1.4 (c) and (d). The narrow spacing between the microelectrodes allows for effective ion transport throughout the device. The SI-SC has a high specific area capacitance of 36.46 mF cm^{-2} and an energy density of 5.34 μWh cm^{-2} on a 100-μm-thick device, due to its increased thickness and linear capacitance. The spatial-interleaving structure also provides excellent stability, with approximately 98.7% performance retention after 104 bending tests. Therefore, the capacitor can be utilized as a power supply in wearable electronic devices such as wristwatches, light-emitting diodes, and calculators.

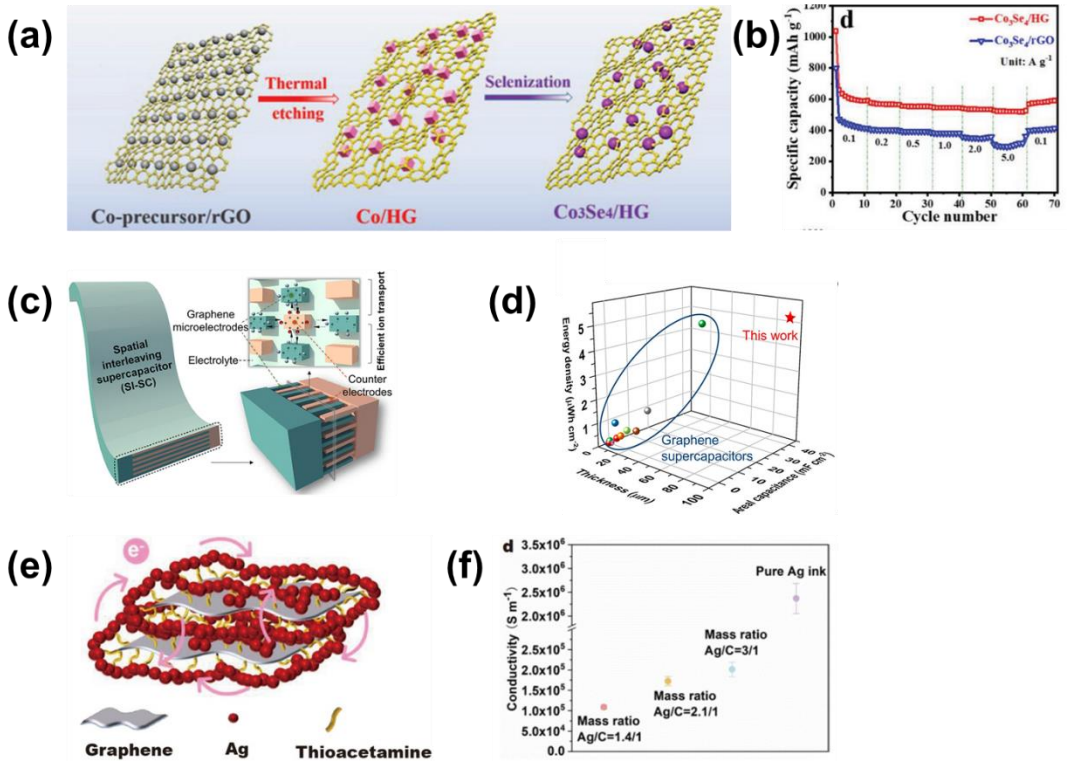

Figure 1.4 (a) Schematic illustration of the synthetic process of the electrode material (Co_3Se_4/HG), and (b) cycling performance of Na-ion battery [25]. (c) A schematic of the SI-SC and the cross-section structure, and (d) a performance comparison with recent graphene-based supercapacitors [26]. (e) Conductivenetwork diagram of conductive ink MB-G/A, and (f) conductivity comparison of patterns based on different inks [27].

Weixin L. et al. [27] have developed paper-based electronic devices with a composite of molecule-bridged graphene/Ag (MB-G/A), which are highly conductive and cost-effective, thereby solving the issue of the high cost of noble silver in conductive ink, as shown in Fig. 1.4 (e) and (f). The high conductivity of MB-G/A is achieved through the formation of a percolation network via graphene. The costs can be reduced, because some of the silver nanoparticles were replaced with graphene. The surface of graphene was linked with silver atoms using cystamine to create a molecular bridge between graphene and silver, which facilitates electron transfer between silver and graphene. As a result, MB-G/A inks can achieve a maximum conductivity of 2.0×10^5 S m^{-1} at less than half the cost of pure silver inks, demonstrating the great potential of MB-G/A inks for commercial electronic devices.

Yu-Hong Y. et al. [28] have fabricated a three-dimensional (3D) carbon-based network using a combination of few-layer graphene (FLG) and carbon nanotubes

(CNTs), as shown in Fig. 1.5 (a). The 3D carbon-based network was used for electromagnetic interference (EMI) shielding application, which overcomes the drawbacks of conventional metallic materials, such as poor durability and secondary reflected electromagnetic waves. Through freeze-drying and composition optimization, the results showed that the 3D-FLG/CNT composite exhibited a high EMI shielding effect of 36 dB, as shown in Fig. 1.5 (b). Therefore, the 3D-FLG/CNT composite can be a potential candidate material for EMI shielding.

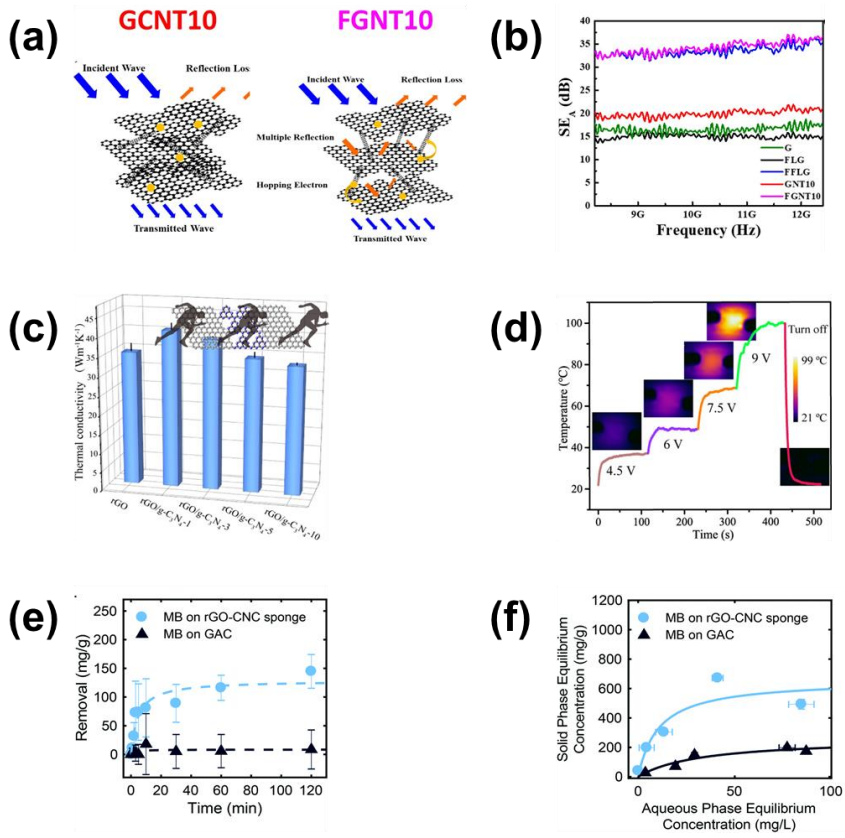

Figure 1.5 (a) Schema of electromagnetic wave shielding by GNT10 and FGNT10, and (b) electromagnetic shielding effect of graphene [28]. (c) In-plane thermal conductivity of rGO and rGO/g-C_3N_4 films, and (d) temperature evolution of an rGO/g-C_3N_4-1 film with different applied voltages [29]. (e) Kinetics of methylene blue adsorption and (f) adsorption isotherms with the respective Langmuir fit on the rGO–CNC sponge and on the GAC [30].

Yanyan W. et al. [29] expands size of the graphene films by using two-dimensional g-C_3N_4 as a linker to connect adjacent reduced graphene oxide (rGO) sheets and form an in-plane rGO/g-C_3N_4 heterostructure. This fabricates the rGO/g-

C_3N_4 thin films, aiming to address the problem of degraded thermal conductivity caused by the phonon scattering of graphene at grain boundaries. The rGO/g-C_3N_4 films achieved an increased in-plane thermal conductivity of 41.2 W m^{-1} K^{-1}, compared to pristine rGO, as shown in Fig. 1.5 (c). Additionally, the rGO/g-C_3N_4 film exhibits excellent solar-thermal and electro-thermal conversion properties, as shown in Fig. 1.5 (d), enabling the chip to operate in an extremely cold environment. This heat dissipation and heating capability shows its potential as a thermal management material in future electronics.

Raphaela A. et al. [30] have developed a sponge of rGO-cellulose nanocrystals that is capable of adsorbing both organic and inorganic ions simultaneously, which is comparable to that of granular activated carbon (GAC), as shown in Fig. 1.5 (e). The initial adsorption rate of methylene blue is as high as 17.0 mg g^{-1} s^{-1}, which is three times that of the commonly used commercial GAC. Moreover, due to differences in surface chemistry and pore structure, the adsorption of GAC can be hindered by organic co-contamination, whereas this sponge is not, as shown in Fig. 1.5 (f). The excellent performance of this sponge indicates great potential for future applications in treating the co-contamination of multiple pollutants.

In spite that graphene has numerous applications, the majority of these applications require that graphene possessing both high quality as well as large quantities. However, due to the limitations of preparation methods, it is usually difficult to produce graphene with both high quality and large quantities, which negatively affects its promotion and use in practical applications. In section 1.3, the current mainstream graphene production methods and their advantages and disadvantages will be detailed, to illustrate the effects of different production methods on graphene quality and yield.

1.3 Preparation methods of graphene

Professor Graphene has been successfully prepared for the first time by a team of scientists led by A. Geim and K. Novoselov, who won the 2010 Nobel Prize in Physics for the first time in 2010. Due to recent advancements in graphene research, there has been a rise in the development of new methods of preparing graphene in recent years. In general, graphene may be prepared in four different ways, all of which have

their own advantages. These methods are as follows: physical exfoliation, chemical vapor deposition (CVD), and reduction of graphene oxide [31].

1.3.1 Physical exfoliation

Through the physical exfoliation process, monolayer graphene is separated from multilayer graphene, graphite, or carbon sources that already contain graphene structures. In order to prepare graphene, the method mentioned previously is typically physical exfoliation, where adhesive tape is used to exfoliate graphite monolayers from graphene monolayers. Furthermore, there are many other physical exfoliation methods that can also be used to produce monolayer and few-layer graphene, such as ball-mill [32], mechanical cleavage [33], and so on [34, 35].

1.3.2 Chemical vapor deposition

The CVD technique is known for its high quality in the preparation of graphene. This process involves heating the metal substrate to a high temperature, about 1000 °C, and then exposing it to a vapor phase carbon source. In this case, the carbon source material is in the vapor phase and undergoes pyrolysis, which generates carbon atoms and allows them to be adsorbed on the surface of the substrate [36, 37]. There are two different mechanisms that can be applied depending on the selected substrate material. For one thing, carbon atoms that adsorb on a substrate, such as copper, are difficult to disperse within the substrate, so they will nucleate on the surface and form graphene [38, 39]. For another, if the substrate exhibited high hydrophilicity of carbon atoms, such as nickel, the adsorbed carbon atoms could be dispersed into the interior area of the substrate at high temperatures [40, 41]. In the subsequent cooling-down process, carbon atoms were precipitated on the substrate surface and grew into graphene.

1.3.3 Reduce graphene oxide

The reduction of graphene oxide is considered to be a feasible method of producing graphene oxide in mass quantities [42-44]. It begins with GO, which is

obtained by oxidizing graphite, and then reducing it into rGO. In most cases, the reduction is accomplished by using a hydrothermal method or using reducing agents, such as hydrogen iodide and ascorbic acid [45, 46]. However, this results in rGO containing a high density of defects, including vacancies [47, 48], which are formed during GO production and are persisted even after reduction.

1.3.4 Graphene oxide reduced by ethanol-associated ultra-high temperature process

Alternatively, the defect problem of rGO can be solved by high-temperature treatment [5, 49], because rearrangement reactions take place on the carbon atoms, and form a stable structure with a honeycomb lattice. On the other hand, this introduces a problem with regard to the stacking structure of multilayer graphene. At high temperatures, AB-stacked structures can be spontaneously formed, which are thermodynamically stable structures. Because of this AB stacking structure, there is a strong interlayer interaction between graphene layers, which results in the degradation of the superior properties of single-layer graphene [50].

In an attempt to circumvent the mentioned issue, theoretical calculations have shown that the properties of single-layer graphene can still be preserved when adjacent graphene layers are randomly rotated or translated, since it has an electronic structure similar to that of single-layer graphene [11]. It has been found through experimental researches that randomly stacked graphene maintains an electronic structure similar to that of single-layer graphene [51], as well as possesses superior properties in comparison with AB-stacked graphene. Richter et al. [52] realized a high mobility of 7×10^4 $cm^2 \cdot V^{-1} \cdot s^{-1}$ for individual flakes of multilayer graphene with a rotationally stacked structure, while Liu et al. [50] found that AB-stacked bilayer graphene films exhibited a mobility of 4.4×10^3 $cm^2 \cdot V^{-1} \cdot s^{-1}$.

In order to reduce the formation of AB-stacked structures during high temperature processes, studies have shown that an ultrahigh temperature (1500−1800 °C) process with the association of ethanol vapor can significantly reduce the fraction of AB-stacked structures. Ethanol vapor at high temperatures generates carbon containing species and reactive oxygen species (hereafter called “ethanol-derived species”), which respectively function as a carbon-supplying source and an

etchant for unstable defective structures in GO during the reduction process. During this process, the ethanol has to be decomposed into different species, and then it has to undergo a series of chemical reactions in the gas phase to transform it into the desired product [53, 54]. There has also been the successful use of this reduction method for few-layer rGO on substrates, and high carrier mobility was achieved [55].

In spite of the benefits offered by these methods, some disadvantages of these methods led to a lack of balance between quantity and quality. Particularly, physical exfoliation, CVD, and epitaxial growth methods have not been able to prepare graphene in bulk scale, while methods for chemical reduction of GO have not been able to prepare graphene with low defect density. The ultrahigh temperature method may be useful for repairing rGO, but at high temperatures, it forms an AB-stacked structure, which degrades its superior properties [50]. With respect to the ethanol-associated ultrahigh temperature process, bulk-scale graphene was only analyzed on the surface of an rGO aggregate [55], and the internal stacking structure was not clarified. These mentioned methods did not meet the needs of macroscopic applications of graphene. Therefore, a novel method was eager to be developed to tackle these problems of high crystallinity, high random stacking fraction, and bulk scale.

1.4 Amelioration of the ethanol-associated ultra-high temperature process

In section 1.3, it is known that the random-stacking fraction can be increased by the participation of ethanol-derived specie in the ultrahigh temperature process, compared to that of using Ar gas [50]. To improve the accessibility of ethanol-derived specie to bulk-scale graphene, increasing the surface area and avoiding the stacking of graphene was considered to be effective methods. In other words, the random-stacking fraction was expected to be improved by preparing rGO as a porous structure and adding spacers between graphene layers.

1.4.1 Sponge rGO with porous structure prepared by freeze-drying

The preparation of a GO sponge with a highly porous structure by freeze-drying is a viable solution for the inaccessibility problem of GO flakes [56]. The mechanism of freeze-drying was explained in section 2.1.

GO dispersions dried by freeze-drying do not aggregate, but can be dried into GO sponges in which GO flakes maintain separation, as in the dispersion. The GO flakes rotate randomly in three dimensions and are less influenced by nearby GO flakes than aggregates or thin films. As a result, the obtained GO sponges are porous and have a large surface area, which makes them ideal for further reduction reactions, as shown in Fig. 1.6. Contrary to the AB stacking fraction, the random stacking fraction of the rGO sponge involves the in-plane rotation and translation of graphene layers, as well as the out-of-plane random rotation in three dimensions.

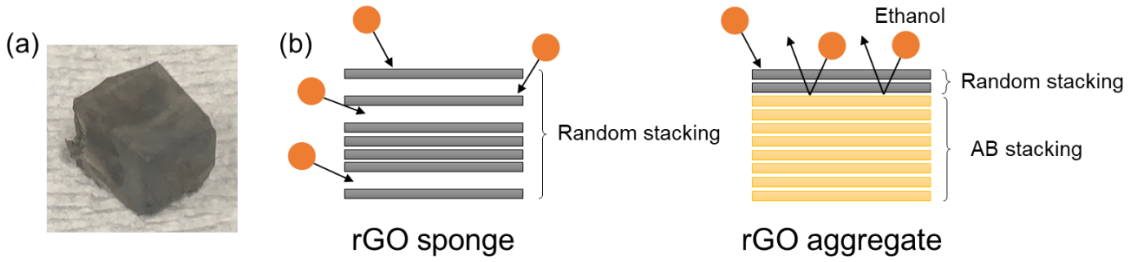

Figure. 1.6 (a) Photograph of graphene sponge, which is 1×1×1 cm, and (b) the large surface area of GO for the following ethanol-associated ultrahigh temperature process.

1.4.2 Reducing the stacking order of graphene by spacers

As well as using porous structures in the ethanol-associated ultrahigh temperature process, other nanomaterials can be used as spacers to prevent graphene layers from stacking, thereby reducing the interlayer interactions caused by ordered stacking.

CNF, a natural cylindrical polymer with plenty of resources, possesses many outstanding properties, including renewability [57], high strength, high stiffness [58-61], and low weight [62], which makes it widely used in many areas [63-65]. (2,2,6,6-

tetramethylpiperidin-1-yl)oxidanyl can be used to prepare CNF, which is known as the TEMPO method. In this process, some of the groups on the surface of CNF are oxidized to carboxyl groups, which increases its water solubility. As a result, CNF is expected to be thoroughly mixed with GO. The material could also be transformed into inert materials at high temperatures without reacting with GO [64, 66]. This composite sponge, which is based upon the two-dimensional (2D) structure of graphene and the one-dimensional (1D) structure of CNF, can be viewed as a mixed-dimensional heterostructure in which material properties are designed by combining different building blocks [67]. In comparison to the pure rGO sample, the rGO/CNF sample was supposed to have a higher random stacking fraction than the pure rGO sample.

The nano-diamond (ND), a zero-dimension (0D) material, serves as a nanospacer. It has received a many of attention for its potential applications in catalysis [68], biosensors [69], and other fields [70]. ND is typically prepared by detonation, followed by an oxidation process to remove impurities [71-73]. ND particles, prepared by the detonation method, exhibited a three-layered structure. The central region of ND consists of a cubic diamond crystal (sp^3-hybridization) as the core, surrounded by partial layers of a fullerene-like shell (sp^2-hybridization) [74], as the intermediate shell of ND. The surface layer of ND contains oxygen-containing groups, which are obtained by the mentioned oxidation process and enhance hydrophilicity [73]. It is important to note that ND differs from CNF in that it is a 0D material with a low aspect ratio, making it more difficult to form micrometer-scale agglomerates [75]. Additionally, at high temperatures, ND transforms into nested sp^2 carbon shells [76], known as carbon nano onions (CNO). This CNO is an inert material and does not react with graphene when the thermal treatment. In view of these advantages, ND appears to be a promising candidate for use as a spacer between graphene layers in order to produce 2D/0D mixed-dimensional heterostructures with a low stacking order. During the ethanol-associated ultrahigh temperature process, the accessibility of ethanol-derived species in the samples can be improved, resulting in the suppression of AB-stacked structures.

1.5 Motivation and challenges

The preparation method of graphene has different drawbacks, resulting in it being hard to use in daily applications. Graphene produced by CVD and exfoliation methods were limited by low yield. On the other hand, although chemical reduction and

high-temperature methods can produce rGO with bulk scale, they still face challenges. The chemical reduction method led to high defect density, while the high-temperature method led to AB stacking of graphene flakes, resulting in a degradation of the excellent properties of graphene. In contrast, the ethanol-associated ultrahigh temperature method can produce bulk-scale graphene with high crystallinity and high random stacking fraction.

However, one limitation of the ethanol-associated ultrahigh temperature method is that ethanol was hard to access into the internal area of the rGO aggregates, leading to a randomly stacked structure on the surface but AB stacked structure in the internal area of the rGO aggregate. To address this issue, GO sponges were prepared through freeze-drying in this study, allowing ethanol vapor to access the internal area of the GO sponge during the ultrahigh temperature process. As a result, a high randomly stacked fraction was achieved on both the surface and internal area of the GO sponge.

Although ethanol-associated ultrahigh temperature treatment can reduce AB stacking fraction in both the internal and surface area of GO sponge, it can also lead to an increase in the crystalline size in the stacking direction during the process. The crystalline size in the stacking direction corresponds to the thickness of multilayer graphene, as shown in Fig. 1.7, named as the L_c in this research. Therefore, the random stacking fraction can be further increased by reducing the crystalline size in the stacking direction of graphene. In this study, the further stacking of GO flakes during ultrahigh temperature treatment was restrained by the addition of nanospacers. Moreover, the nanospacers made it easier for ethanol vapor to access rGO flakes with lower thickness, which resulted in an increase in the random stacking fraction.

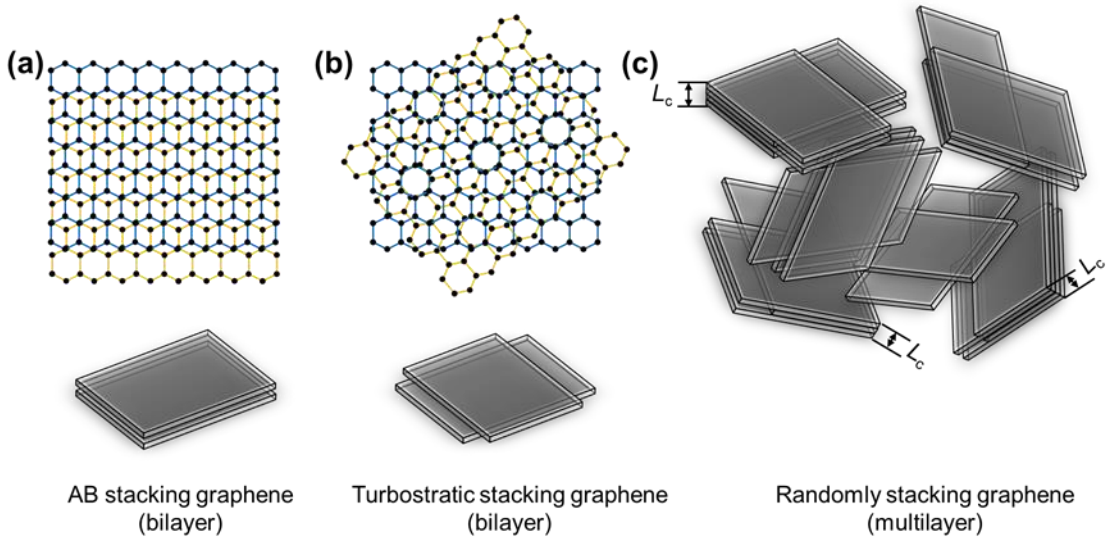

Figure 1.7 Schematic images of (a) AB stacking graphene, (b) turbostratic stacking graphene, and (c) randomly stacking graphene with the length of L_c.

Besides, graphene shows promise as an alternative material for strain sensors, due to its excellent properties, which can overcome the limitations of conventional metal ones. However, current graphene-based strain sensors were fabricated from chemically rGO and suffered from low linearity and large hysteresis in sensor response as well as high initial resistance. These issues should be caused by functional groups and defects remaining on the rGO. Furthermore, the addition of a small amount of ND can further enhance the sensitivity of the strain sensor.

Graphene shows promise as an alternative material for strain sensors, due to its excellent properties, which can overcome the limitations of conventional metal ones. However, current graphene-based strain sensors were fabricated from chemically reduced graphene oxide and suffered from low linearity and large hysteresis in sensor response as well as high initial resistance. These issues should be caused by functional groups and defects remaining on the rGO.

1.6 Organization of the thesis

This thesis consists of six chapters.

Chapter 1 first introduced monolayer graphene, the electronic structure of AB-stacked and random-stacked graphene. Then, it presented the various applications research of graphene, followed by the synthesis methods of graphene with their advantages and disadvantages.

Chapter 2 expressed experimental and characterization methods. The experiment apparatus used for sample preparation includes a lab-made vacuum drying system for freeze-drying, an infrared radiation furnace, and two tubular electric furnaces. The testing methods include Raman spectroscopy, scanning electron microscopy (SEM), X-ray diffraction (XRD), and a lab-made set for testing the performance of the strain sensor.

Chapter 3 first focused on the comparison of the random-stacking fraction of the internal and surface area of rGO aggregates and rGO sponges treated with the ethanol-associated ultra-high temperature process. The temperature was then reduced to 1500 °C to increase the $I(G')/I(G)$ of the rGO sponge. Finally, the overall random-stacking fraction was increased by adding CNF as a nanospacer to reduce stacking.

In Chapter 4, two types of sponges, rGO/CNF and rGO/ND, were produced, and their random-stacking fraction was compared. The crystalline size variations in their stacking direction were analyzed by XRD, and the changes in the first component and the second component of the rGO flakes were analyzed. Finally, the reason for the variation in the random-stacking fraction of the rGO/CNF and the rGO/ND was explained.

Chapter 5 focused on the fabrication of strain sensors using the obtained rGO and rGO/ND sponges under different reduction conditions and the performance testing of the strain sensors. The obtained rGO sensors were compared on their linearity, initial resistance, and hysteresis, to understand the influence of crystallinity of rGO. By analyzing the changes in the ND concentration in rGO and rGO/ND sponges and the thickness of rGO flakes, the reason for the sensitivity of the strain sensor changing with the ND concentration was inferred.

In the final chapter, a summary was provided of the previous five chapters, and a future perspective was offered based on the bulk-scale, high crystallinity, and high random-stacking fraction of the rGO sponge.

Chapter 2 Experimental

2.1 Experiment procedure

2.1.1 Preparation of rGO and rGO/spacer sponge

The 1 wt% GO/water dispersion was prepared from bulk graphite by a modified Hummers' method [77]. The GO flake size was evaluated to be around 10 μm by optical microscopy. The diluted GO dispersion weight percentage was 0.8 wt%, which was equal to that of the GO/spacer composite samples. The CNFs were prepared by the TEMPO method and used as received from DKS Co. They featured a high aspect ratio of 4–10 nm in diameter and 1 μm in length. The GO dispersion was blended with CNFs in water [5]. The NDs were prepared by the detonation method and used as received from Nippon Kayaku Co. They featured an average of 5 nm in diameter. The GO dispersion was blended with NDs in water.

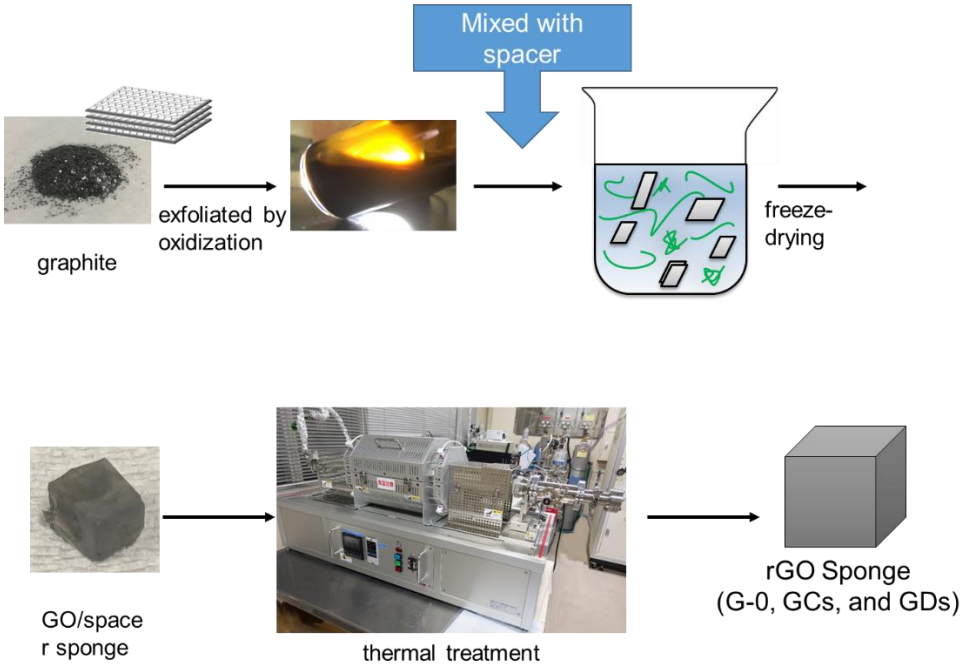

Figure 2.1 Schematic illustrations of the fabrication process of the rGO sponge.

A lab-made vacuum drying system was used for the freeze-drying process [5]. To prepare 1 cm^3 cube sponges of GO and GO/spacer, the dispersion was poured into an ice tray and then frozen using liquid nitrogen. The tray was installed in the vacuum drying system, and its chamber was pumped for 72 hours.

The GO and composite sponges were thermally treated in ethanol/Ar under ultra-high temperature conditions for repairing and reduction. The ultrahigh temperature process was performed using the tubular electric furnace or the infrared radiation furnace.

2.1.2 Preparation of strain sensor

To prepare a strain sensor, the obtained sponges were cut into 5×5×5 mm cubes. After adding the initiator to dimethylsiloxane and stirring, the obtained PDMS was poured into the mould and heated at 80 °C for 7 minutes, and the partially cured PDMS film was prepared with about 35×25×2 mm. The cut sponge, silver paste, and copper wire were placed on the PDMS film and covered with another PDMS film, as shown in Fig. 2.2. By pressure and further heat treatment (80 °C for 10 minutes), strain sensors are obtained for the sensor performance testing.

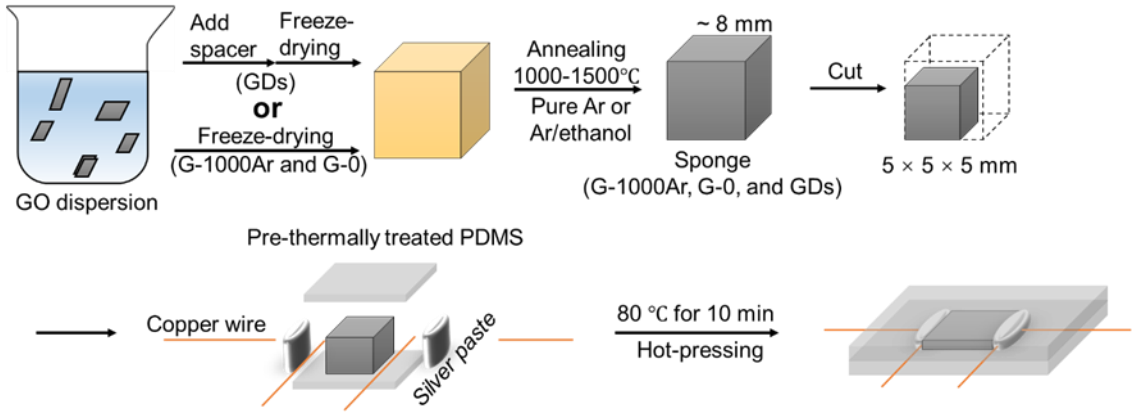

Figure 2.2 Schematic illustrations of the fabrication process of the rGO strain sensor.

2.2 Experiment apparatus

2.2.1 Mixing and freeze-drying

The preparation of rGO and rGO/spacer dispersion began with the 1 wt% GO/water dispersion, which was prepared from bulk graphite by a modified Hummers' method [77] and used as received. The received GO dispersion was diluted or blended with nanospacer in water by a blender operating at 10,000 RPM for 2 minutes, and the target GO dispersion was obtained. The blender was made up of the electric motor and container, as shown in Fig. 2.3 (a) and (b), respectively.

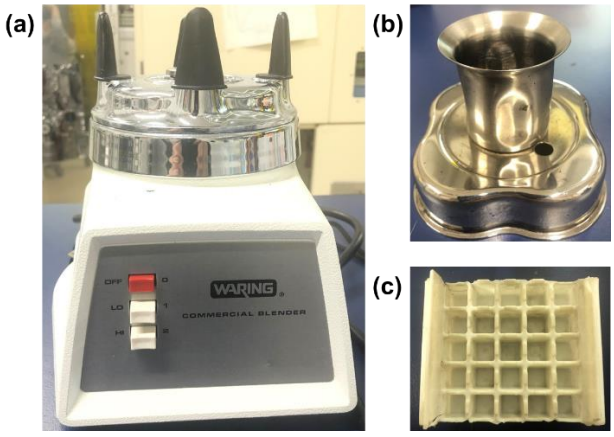

Figure 2.3 (a) Electric motors and (b) container of the blender. (c) Ice tray with 1×1×1 cm^3 size.

A lab-made vacuum drying system was used for the freeze-drying process [5, 75] to prepare 1-cm^3 cube sponges of GO with or without spacers from the obtained dispersion. The dispersion was poured into an ice tray, as shown in Fig. 2.3 (c), and then frozen using a freezer or liquid nitrogen. The tray was installed in the vacuum drying system, and its chamber was pumped for 48−72 hours. With chamber pressures of about 100 Pa, pumping causes the water in the frozen dispersion to sublimate, leaving the network structure as a GO or composite sponge for the following thermal treatment.

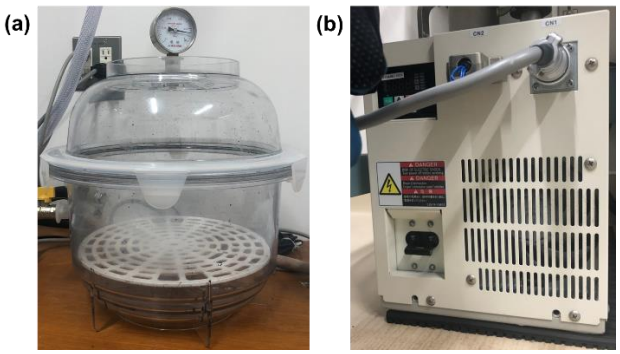

Figure 2.4 (a) Chamber and (b) dry pump of the lab-made vacuum drying system.

Freeze-drying is a drying method in which material containing liquid is firstly frozen below freezing point and triple phase point. Then, the solvent sublimates to vapor and is removed under vacuum conditions. In this process, the solvent in the solid phase sublimates directly into the gas phase. In contrast to heat drying and vacuum drying, which cause deformation during evaporation, freeze-drying can preserve the original structure and shape of the material. GO dried by freeze-drying can maintain separation, as that in the dispersion.

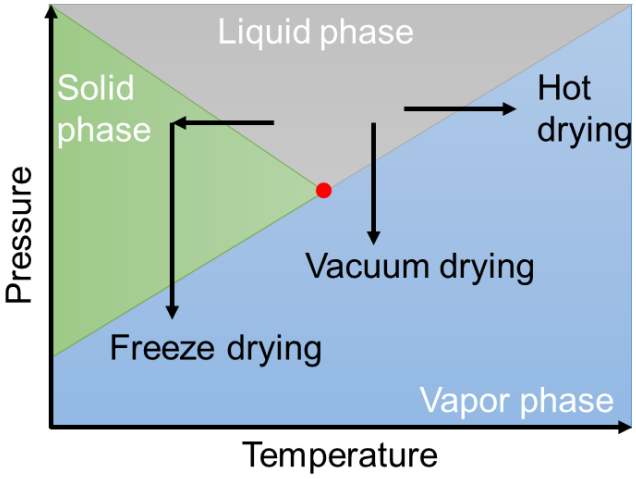

Figure 2.5 Mechanism of heat drying, vacuum drying, and freeze-drying. The red dot is the triple point.

2.2.2 Furnaces used in ultra-high temperature process

The ultra-high temperature process was conducted by an infrared radiation furnace (SR1800G-S, THERMO RIKO Co.), and two tubular electric furnaces (HT1500-50-32P, HEAT TECH Co. and FT-01VAC-1650, FULL-TECH Co.). Note that the infrared radiation furnace has its ventilation system, and the two tubular electric furnaces share the same ventilation system.

The infrared radiation furnace is a device that uses infrared radiation technology for heating. It can rapidly heat up and reach high temperatures within a very small area. In the furnace, the light source and the sample are placed on two foci of the ellipsoidal reflector. The infrared light emitted by the infrared lamp is focused on other foci of the ellipsoidal reflector, enabling the sample to quickly reach the aimed temperatures, up to 1800 °C. The furnace also features a radiometric thermometer for temperature measurement, with a range of 160 °C to 2000 °C and an emissivity of 0.78.

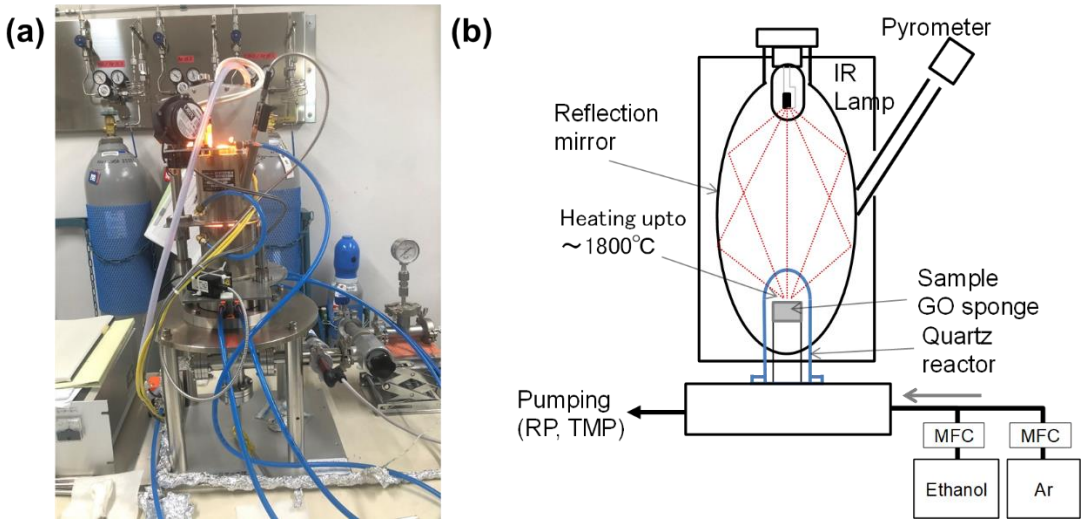

Figure 2.6 (a) Infrared radiation furnace and (b) its schematic diagram of internal structure.

A lab-made ventilation system was connected to the infrared radiation furnace, as shown in Fig. 2.7 (a) and (b). This ventilation system is able to not only control the flow rate but also achieve gas line switching. By utilizing this ventilation system, the feeding of carbon source can be accurately controlled within the reaction time, while avoiding significant changes in gas flow and pressure. To clarify, during the temperature increase in the infrared furnace, only carrier gas can be introduced into the

reactor. The carbon source gas should only be introduced into the reactor once the desired temperature has been reached.

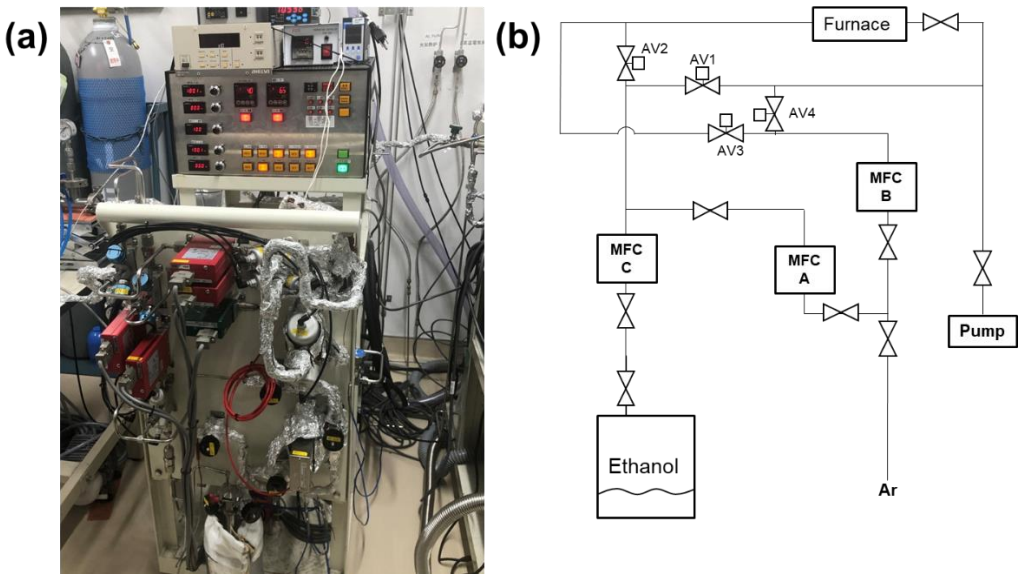

Figure 2.7 (a) Ventilation system connected to the infrared radiation furnace. (b) The simplified diagram of gas lines of the ventilation system.

Both of the tubular electric furnaces are resistance furnaces that utilize SiC as a heater, with a maximum operating temperature of 1650 °C. The material of tubes for the tubular furnaces is aluminum oxide. To prevent sample contamination caused by reactions between aluminum oxide and carbon sources at high temperatures, a carbon inner tube was used within the aluminum oxide tube in this study. Additionally, a pair of reflectors was placed inside the aluminum oxide tube at both ends of the inner tube to provide thermal insulation.

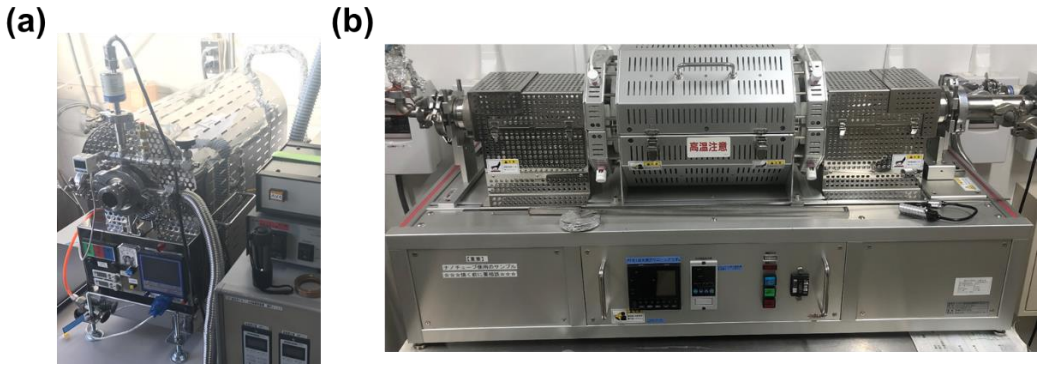

Figure 2.8 Tubular electric furnaces of (a) FT-01VAC-1650 and (b) HT1500-50-32P.

Another lab-made ventilation system was utilized and connected to the tubular electric furnaces, as shown in Fig. 2.9 (a) and (b). This ventilation system also can control the flow rate and achieve gas line switching. By utilizing this ventilation system, the feeding of carbon source can be accurately controlled within the reaction time, while avoiding significant changes in gas flow and pressure.

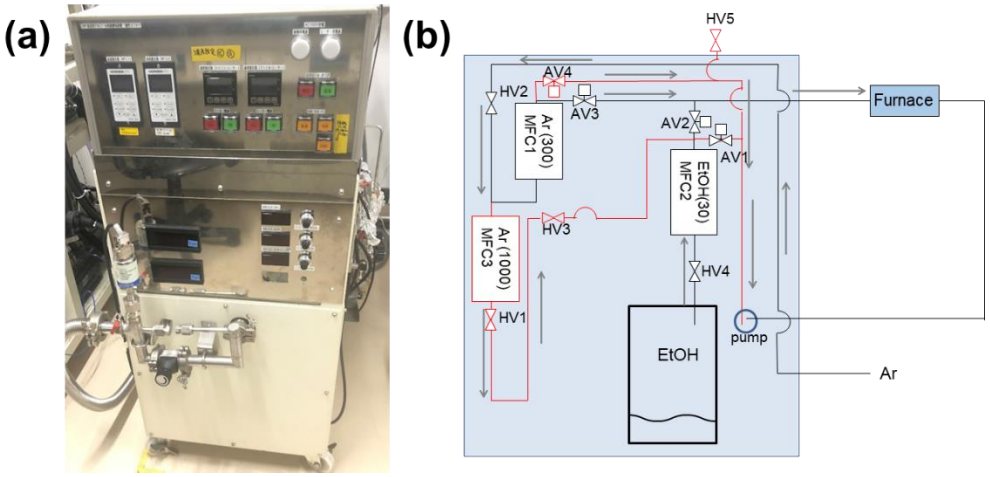

Figure 2.9 (a) Ventilation system connected to the tubular electric furnaces. (b) The simplified diagram of gas lines of the ventilation system.

2.3 Characterization

2.3.1 Raman measurement and analysis

The principle of Raman spectroscopy is based on the interaction between a laser and a sample [78-80]. When a laser beam irradiates the sample, photons interact with the molecules in the sample and scatter in different directions. Most of the scattering is elastic scattering, also known as Rayleigh scattering, where the photon has the same energy as the incident photon, as shown in Fig. 2.10 (a) [79]. However, a small fraction of scattered photons undergo non-elastic scattering, known as Raman scattering, which is due to the interaction between the laser and the molecules in the sample resulting in different energies. Stokes and anti-Stokes scattering are two types of Raman scattering, corresponding to when the energy of the scattered photon is less than or greater than the incident photon, respectively, as shown in Fig. 2.10 (a) [79]. The frequency difference between the incident and scattered photons corresponds to the vibrational energy of the molecules in the sample, which can be used to identify the chemical composition of the sample.

In experiments, Raman instruments allow for laser light to be scattered from the sample. A filter is used to separate the Raman scattering from the incident light and Rayleigh scattering. Finally, the signal is collected by a detector for analysis, as shown in Fig. 2.10 (d) [80]. Therefore, Raman spectroscopy can provide information on the molecular structure and composition of a sample by measuring the energy and wavelength of the Raman scattered light. In the case of graphene analysis, Raman spectroscopy is capable of detecting three characteristic peaks, namely D, G, and G′ bands, as shown in Fig. 2.10 (b).

The G-band and D-band can be commonly observed around 1580 cm^{-1} and 1350 cm^{-1}, respectively. The former derives from the in-plane stretching mode of the hexagonal lattice of graphene, and the latter originates from the hexagon-breathing mode activated through the presence of lattice defects. The intensity ratio of the D-band to the G-band, $I(D)/I(G)$, corresponds to the defect density of graphene. Note that the relationship between D-band intensity and defect density is classified into two different stages depending on defect density, namely interdefect distance. In the case of a small interdefect distance less than ~3 nm, D-band intensity decreases with increasing defect density, named as stage 1, whereas in the case of a large interdefect distance larger than

~3 nm, D-band intensity increases with increasing defect density, named as stage 2 [81]. Stage 1 and stage 2 can be distinguished by the broadening of D-band.

The G′-band of the graphene samples was observed around 2700 cm^{-1} with different sharpness and intensity. The intensity ratio of the G′-band to the G-band, $I(G')/I(G)$, provides information about the interlayer interactions of graphene because the G′-band is sensitive to the layer number and stacking order of graphene. Note that G′-band is also called 2D-band in the literature [82]. For distinction from two-dimensional (2D), the notation G′-band was used in this paper.

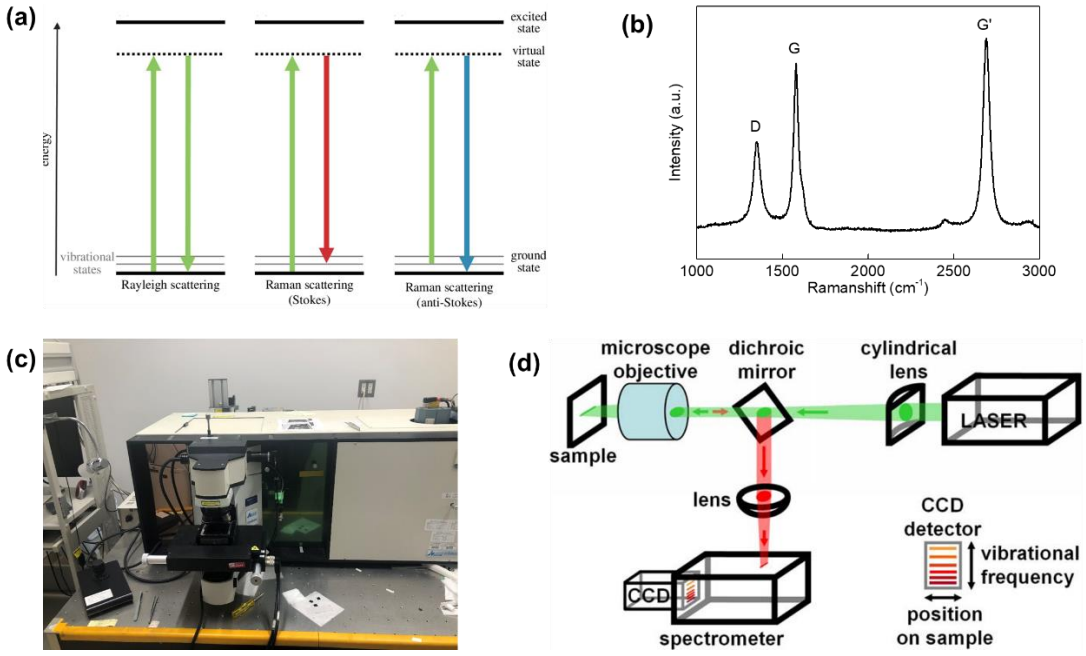

Figure 2.10 (a) Rayleigh scattering and Raman scattering [79]. (b) Typical Raman spectrum of our graphene sample with D, G, and G′ bands. (c) Image of Raman microscopy spectrum (e) Schematic presentation of typical Raman spectroscopy instrument [83].

The stacking order of the graphene sample can be obtained by further analysis of the G′-band peak shape. According to Cançado et al. [84], the G′-band in the Raman spectrum of multilayer graphene can be fitted by three Lorentzian peaks, as shown in Fig. 2.11. The first peak was located around 2700 cm^{-1}, which is close to the frequency of the original G′-band of monolayer graphene. It is denoted as a G'_{2D} component because it is associated with a two-dimensional graphite feature in which the stacking

order along the c-axis is low, namely a turbostratic structure or randomly stacked structure. The two other peaks around 2680 cm^{-1} and 2720 cm^{-1} are denoted as G'_{3DA} and G'_{3DB} components, respectively. These are related to the three-dimensional configuration of graphite, that is, the AB-stacked structure. It should be mentioned that the intensity of G'_{3DB} is proportional to the volume of 3D graphitic regions [8, 84]. We employed Cançado's method to calculate the random-stacking fraction in the bulk-scale graphene.

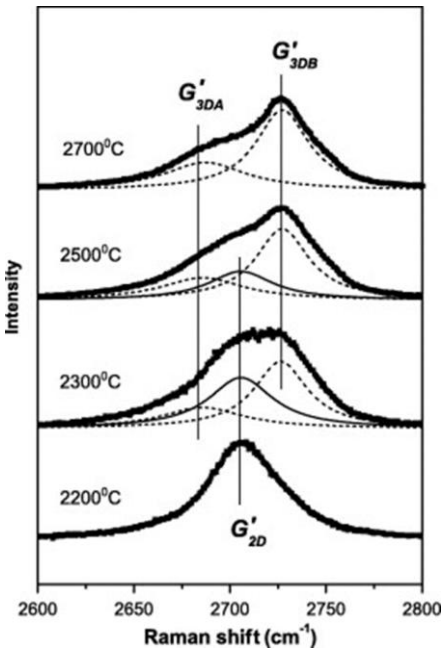

Figure 2.11 G′-band was fitted by three components [84].

From the intensities of the three components, the random stacking-fraction of graphene, *T*, can be written as

$$T\ [\%] = \frac{I(\mathrm{G'_{2D}})}{I(\mathrm{G'_{3DB}}) + I(\mathrm{G'_{2D}})} \times 100 \qquad (2.1)$$

where $I(G'_{2D})$ and $I(G'_{3DB})$ denote the intensities of G'_{2D} and G'_{3DB} peaks, respectively. For an ideal random-stacking structure of multilayer graphene, the Raman spectrum shows single-layer graphene-like features, *i.e.*, a strong G'_{2D} peak and negligible G'_{3DA} and G'_{3DB} peaks, which will result in a *T* value close to 100%.

LabRAM HR-800 UV (Horiba Jobin Yvon), as shown in Fig. 2.10 (c), was used in this research with an excitation laser wavelength of 532 nm, power of 1 mW, and spot size of 1 μm.

2.3.2 Scanning electron microscope

SEM is a characterization technique that utilizes the interaction between electrons and the sample (specimen). The working principle is started with emitting of the electron from an electron gun, which is then focused to a size ranging from nanometers to micrometers by a condenser lens, as shown in Fig 2.12 (a). When the electron beam hits the sample surface, it interacts with the atoms on the surface of the sample (specimen), resulting in various signals, including secondary electrons, backscattered electrons, Auger electrons, and characteristic X-rays. Among these signals, secondary electrons can reflect the surface topography of the sample (specimen), as shown in Fig 2.12 (b). These signals are detected by a detector and converted into image signals based on signal type and electron energy. SEM images were taken by VE-8800 (Keyence), as shown in Fig 2.12 (c), at an acceleration voltage of 15 kV and a working distance of about 33 mm.

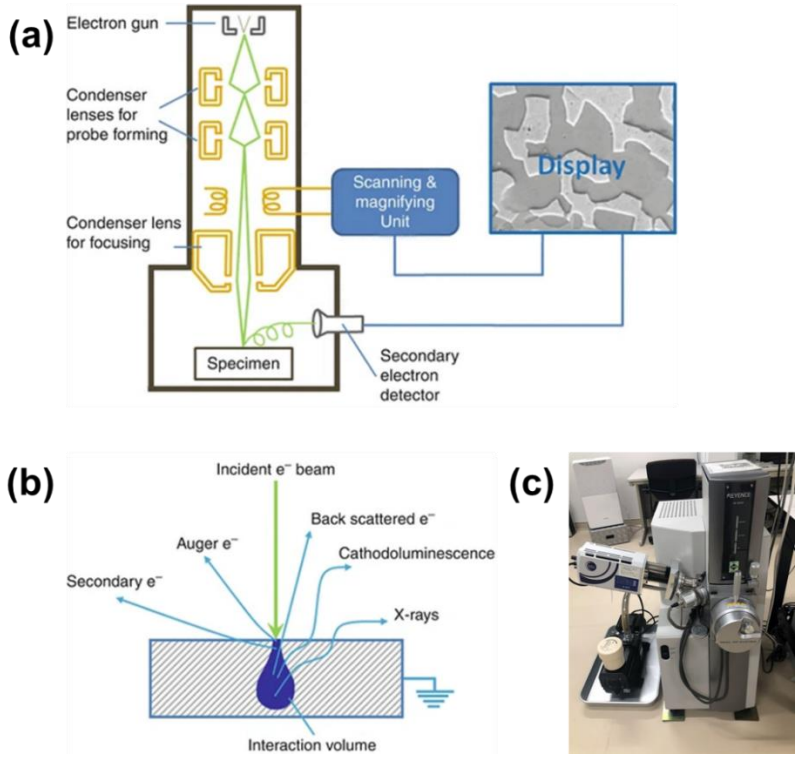

Figure 2.12 (a) Schematic diagram of SEM. (b) Interactions between the electron beam and specimen [85]. (c) The SEM, VE-8800, was used in this research.

2.3.3 X-ray diffraction

XRD is a powerful technique used for studying the structure of materials by analyzing the diffraction of X-rays from the atomic planes within the material. X-rays are generated by directing high-speed electrons at a metal target. The appearance of diffraction peaks in XRD is based on Bragg's equation, which relates the angle of incidence of X-rays on a crystal to the spacing between crystal planes. In other words, the layer distances (d_{002}) of graphene can be calculated by Bragg's equation:

$$d = \frac{n\lambda}{2\sin\theta} \tag{2.2}$$

where n, d, θ, and λ denote the diffraction order, the layer distance, the glancing angle, and the wavelength, respectively. When X-rays interact with the crystal, they scatter and interfere with one another, producing diffraction patterns. The strong peak can be observed when Bragg's equation is satisfied while the scattered waves from adjacent atomic planes constructively interfere.

The L_c can represent the crystalline size in any crystallographic direction, while in this study, the focus was specifically on the crystalline size of graphene in the stacking direction. Henceforth, L_c exclusively referred to the crystalline size in the stacking direction of graphene.

The L_c can be obtained by the following method. On the surface of crystallites, there is typically some degree of distortion that deviates from the ideal lattice structure. This distortion is more obvious in smaller crystalline sizes due to the larger surface area. When X-rays are directed at powder samples of small crystallites, these distortions result in a broadening of the diffraction pattern. In simple terms, the width of the diffraction pattern is influenced by the size of the crystalline, with smaller crystalline yielding broader diffraction patterns. Consequently, by analyzing the extent of broadening in the diffraction patterns, the average crystalline size was determined by Scherrer's equation as follows:

$$L_c = \frac{K\lambda}{\beta \cos\theta} \tag{2.3}$$

where K denotes the shape factor, which was 0.9 [86]; β, θ, and λ denotes the FWHM of the 002 peak, the glancing angle, and the wavelength, respectively. The applicability of Scherrer's equation is 3–100 nm [87].

The XRD measurements were conducted using Ultima IV (Rigaku Co.) and SmartLab (Rigaku Co.) via a standard Cu-Kα source having λ = 1.5406 nm, with 40 kV and 40 mA. The accuracy of XRD measurement was confirmed by measuring silicon powders and detecting Si 111 peak at 28.4°. The scanning speed from 10 to 20° was 0.5°/min.

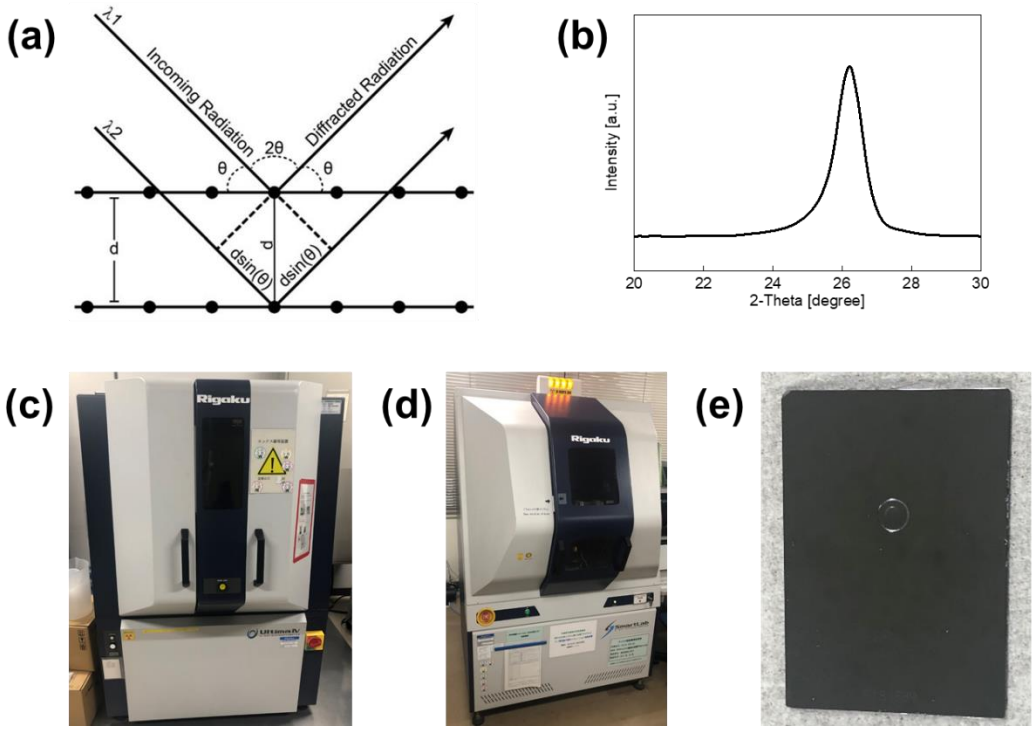

Figure 2.13 (a) Schematic representation of Bragg's law conditions [88]. (b) Typical XRD patterns of our sample. Instruments of XRD of (c) Ultima IV and (d) SmartLab. (e) Si sample holder for XRD measurements

2.3.4 Strain sensor performance testing with the four-wire method

The sensor performance was tested with a lab-made measuring device, as shown in Fig. 2.14 (a). The device consisted of two parts: the sensor operation part and the resistance measurement part. The sensor operation part consisted mainly of a stepping motor and its control unit, while the resistance measurement part was implemented by a DC voltage-current source/monitor (ADC 6241A). The contact resistance was evaluated by comparing the initial resistance of GDs obtained using both the two-wire and four-wire methods, as well as the comparison of sensor performance of G-0 evaluated separately using both methods, as shown in Fig. 2.14 (b) and (c). It should be noted that the two-wire method was exclusively used for this evaluation, whereas the four-wire method was employed for all other samples to ensure accurate measurements by minimizing the influence of contact resistance between the wires and the strain sensor. Measured parameters to evaluate the sensor performance are denoted as follows. L_0 and R_0 are the initial length and resistance of a sponge sample without

deformation, and ΔL and ΔR are the difference of the length and the resistance between initial and operating conditions, respectively. $\Delta L/L_0$ and $\Delta R/R_0$ are the relative variation of length and resistance and were utilized for the evaluation of the sensor performance. Before the stretching process, R_0 was measured. In the stretching process, the sample was stretched up to 40% of $\Delta L/L_0$. The stretching process had five steps. Each step consists of 8% stretching in length ($\Delta L/L_0$), pausing for 2 s to stabilize possible delay of the deformation, and measurement of the resistance for strain sensing. After five steps of the stretching processes were completed, the sensor was operated to reverse direction for releasing the strain with the same step interval as the stretching process. The resistance at each step in the releasing process was measured and compared with the resistance for the stretching process to evaluate the hysteresis in the sensor operation. Thus, ΔR of each step can be obtained, and the ΔR_{max} was measured at the maximum of the $\Delta L/L_0$ (40%). The stretching and releasing processes were repeated ten times to obtain the averaged $\Delta R/R_0$. In this study, the sensitivity of the strain sensor is evaluated by GF, which is defined as GF = $(\Delta R/R_0)/(\Delta L/L_0)$. The linearity is obtained by the adjusted coefficient of determination of the linear regression of GF. The adjusted coefficient of determination is a statistical metric used to evaluate the accuracy of a model. In the strain sensor operation, the proportional relationship between $\Delta R/R_0$ and $\Delta L/L_0$ indicates the sensor response with high linearity, which corresponds to improved accuracy of the measured value.

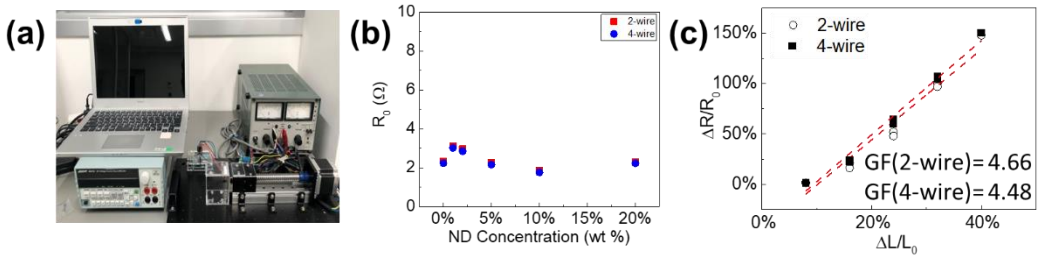

Figure 2.14 (a) Lab-made measurement set-up for strain sensor, (b) the initial resistance obtained by the two-wire and four-wire method, (c) Typical result of strain sensor performance testing, and the sensor performance obtained by the two-wire and four-wire method.

Chapter 3: Bulk-scale synthesis of randomly stacked graphene with high crystallinity

3.1 Background

Graphene possesses numerous excellent properties, such as high carrier mobility, electrochemical performance [1], optical transparency, thermal conductivity [3], and mechanical strength [4]. These properties are attributed to the unique electronic structure derived from a one-atom-thick honeycomb lattice of single-layer graphene. Due to these excellent properties, graphene and graphene-containing materials have been studied extensively toward applications in electronics [89-91], electrode materials [15-18, 92], etc. One problem is that the thinness and small volume of a single-layer graphene flake limits the electrical, mechanical, and other performances. Thus, bulk-scale graphene, which is an aggregate composed of plenty of graphene flakes, is required for various daily applications [93], such as pressure sensors [13, 14] and battery electrodes [15-18, 37]. The preparation of high-quality bulk-scale graphene is a critical issue for practical applications.

The production of bulk-scale graphene starting from GO is a promising approach due to mass-production compatibility and structure controllability. In this production process, GO flakes are dispersed in solution through the functionalization of bulk graphite with oxygen-containing groups. GO is then reduced into rGO. The most common approach for reduction is a hydro-thermal method or a chemical method [45, 46], but these do not address the defect issue, such as vacancy. Alternatively, a high-temperature treatment method can produce rGO with the highest crystallinity [49]. However, the stacking structure of multilayer graphene is problematic. The thermodynamically favorable AB-stacked structure of multilayer graphene is formed during the reduction of GO at high-temperature. A strong interlayer interaction in AB-stacked multilayer graphene causes its electronic structure to deviate from that of single-layer graphene, degrading the superior properties [50]. On the other hand, theoretical calculations have predicted that randomly stacked graphene, where adjacent graphene layers are randomly rotated or translated, can preserve the properties of single-layer graphene because it has an electronic structure similar to that of single-layer graphene [11]. Experimental studies have confirmed that randomly stacked graphene keeps a single-layer-like electronic structure [51] and has superior properties

compared to AB-stacked graphene. Richter et al. [52] realized a high mobility of 7×10^4 cm^2 $V^{-1} \cdot s^{-1}$ for individual flakes of multilayer graphene with a rotationally stacked structure, while Liu et al. [50] found that AB-stacked bilayer graphene films exhibited a mobility of 4.4×10^3 cm^2 $V^{-1} \cdot s^{-1}$. The development of fabrication methods for bulk-scale graphene with controlled interlayer stacking is crucial to realize graphene-based applications in numerous fields.

The previous research produced graphene with a high fraction of the randomly stacked structure from GO aggregates by ultrahigh temperature reduction under an ethanol vapor supply [54]. At ultrahigh temperature, ethanol is decomposed into different species, and further chemical reactions in the gas phase occur [53]. Reaction products containing carbon atoms and OH groups (hereafter called as "ethanol-derived species") mainly act as carbon sources and etchants, respectively. This reduction method has also been utilized for few-layer rGO on substrates and achieved a high carrier mobility [55]. However, the analysis of the bulk-scale graphene was limited to the outer surface of a GO aggregate [54], and the stacking structure of the internal area was not clarified. The repairing process and the formation of a randomly stacked structure should be limited to the surface area of the GO aggregates because the ethanol-derived species cannot enter the internal area of dense samples.

Accessibility of ethanol-derived species to GO flakes should be a critical factor for the successful formation of a randomly stacked structure induced by ethanol-mediated reduction of GO. The preparation of a GO sponge with a highly porous structure by freeze-drying is a potential solution for the inaccessibility problem of GO flakes [56]. Freeze-drying is a method by which liquid-containing materials are frozen below the freezing point, and the solvent is sublimated into a vapor and removed under a vacuum. The original structure and shape of the material are maintained because the solvent in the solid phase is sublimated directly into the gas phase. Instead of aggregation, the GO dispersion can be dried into a GO sponge where GO flakes maintain separation similar to the dispersion. It should be mentioned that GO flakes were randomly rotated in three dimensions, which was less impacted by nearby GO flakes compared to aggregate or film samples. The as-prepared GO sponge has a porous structure with a large surface area, which is suitable for further reduction reactions.

Besides inhibiting AB-stacked structure formation during the reduction process, the addition of other materials as spacers may effectively prevent graphene layers from stacking physically. Spacers must be chemically inert or transformed into

inert materials at high temperature to prevent reactions between GO and spacers. Additionally, the spacers must be water soluble to promote molecular-level mixing of GO and the spacers. CNF fulfills these requirements for spacers. CNF is a natural cylindrical polymer with plenty of resources, renewability [57], high strength, high stiffness [58-61], and low weight [13, 62], which makes it widely used in many areas [63, 65, 94]. CNF can be prepared by (2,2,6,6-tetramethylpiperidin-1-yl)oxidanyl, which is known as the TEMPO method. CNF possesses a high aspect ratio of 4–10 nm in diameter and 1 μm in length [57], which is suitable for intercalation into the GO interlayers in a dispersion before reduction. The water-solubility was improved by carboxylate groups on CNF [64, 95]. These effects make CNF a promising candidate as a spacer for graphene.

Herein a method was proposed, which combined freeze-drying and an ultrahigh temperature process to produce bulk-scale graphene to tackle property degradation due to the strong interlayer interaction in AB-stacked structure. This method can repair and reduce GO on the bulk scale and realize a high random-stacking fraction, which should preserve the properties of single-layer graphene. A GO sponge prepared by freeze-drying of a GO dispersion presents a larger surface area than a GO aggregate. An increase in the accessible area of the GO sponge by ethanol vapor contributes to a high crystallinity and high fractions of random stacking. Additionally, this study provides an approach to further decrease the AB-stacked structure fraction of a graphene sponge utilizing CNF. CNF serves as a spacer that intercalates between the graphene layers to prevent stacking where the graphene layer contact directly (direct stacking). This rGO/CNF sponge features a low defect density, large surface area, reduced interlayer stacking, and bulk-scale production compatibility, increasing its potential applicability.

3.2 Experimental section

3.2.1 Preparation of rGO sponge

Fig. 3.1 schematically illustrates the fabrication process of bulk-scale graphene samples. GO was prepared from graphite by a modified Hummers' method [77]. The obtained GO dispersion was 1 wt% in water solvent, and the flake size of GO was about 10 μm (observed by optical microscopy). The following freeze-drying process was

carried out by a lab-made vacuum drying system to prepare a GO sponge. A GO dispersion was added into an ice tray and shaped into a 1-cm^3 cube. It was then frozen in a freezer at −10 °C overnight, followed by pumping for 48 hours. Under the condition of chamber pressures of about 100 Pa, pumping sublimated the water in the frozen GO dispersion, leaving the GO network structure as a GO sponge. Then the GO sponge was thermally treated in ethanol/Ar gas under ultrahigh temperature conditions for repair and reduction. Instead of the solar furnace used in our previous study [54], the ultrahigh temperature process was performed at 1800 or 1650 °C using an infrared radiation furnace (SR1800G-S, THERMO RIKO Co.) or at 1500 °C using a tubular electric furnace (FT-01VAC-1650, FULL-TECH Co.). Both of the furnaces were connected to vacuum pumps to maintain low pressure. We introduced 20 sccm of Ar under the total pressure of 26.6 Pa during temperature rise. After reaching the set temperature, the thermal treatment was conducted at ultrahigh temperature with flowing 100 sccm of Ar and 0.3 sccm of ethanol under the pressure of 106.6 Pa. The obtained samples, which were named GS-Et1800, GS-Et1650, and GS-Et1500, respectively, were cut by a cutter to characterize the stacking structure of the internal area by Raman spectroscopy. The surface of GS-Et1800, named GS-Et1800-surf, was also characterized by Raman spectroscopy for comparison with the internal area. GS-Ar1800 was prepared by the same procedure at 1800 °C without ethanol vapor (100 sccm of Ar under the total pressure of 106.6 Pa), and GS-Ar1800-surf was readied for Raman spectroscopy. The measurement condition of Raman spectroscopy will be stated in the following section.

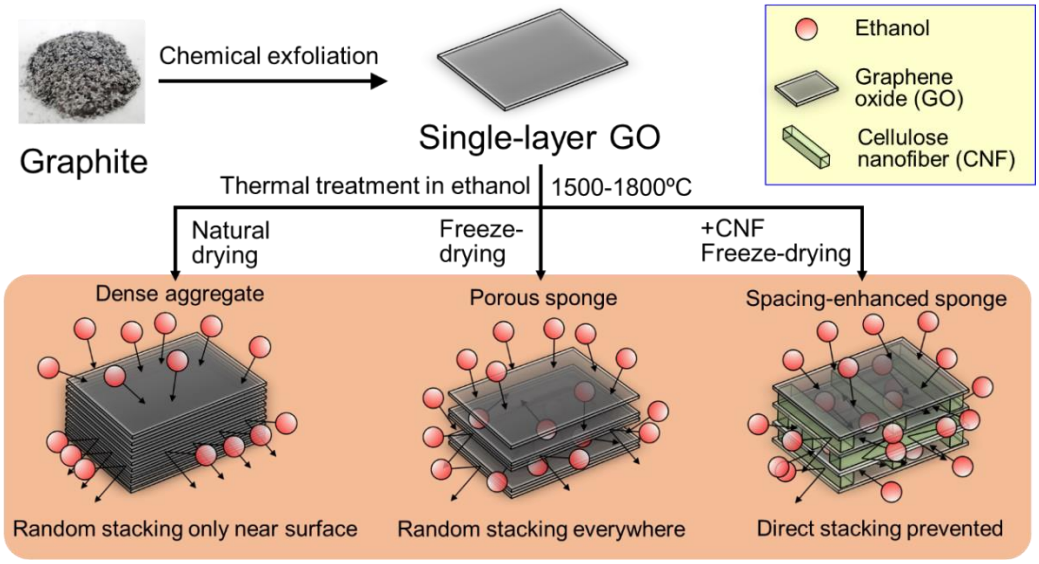

Figure 3.1 Schematic illustrations of the bulk-scale graphene fabrication process. GO aggregate,

GO sponge, and GO/CNF sponge are prepared from a GO dispersion by natural drying, freeze-drying, and freeze-drying with the addition of CNF, respectively. GO samples with different morphologies are then reduced into rGO by ethanol-associated reduction under ultrahigh temperature conditions [5].

3.2.2 Preparation of rGO aggregates

For comparison with the porous GO sponge samples, GO aggregates were prepared by naturally drying a GO dispersion and a subsequent thermal treatment for repair and reduction in an infrared radiation furnace in Ar gas or ethanol/Ar gas at 1800 °C [54], named GA-Ar1800 and GA-Et1800, respectively. The inside of GA-Et1800 was examined by Raman spectroscopy after cleaving with adhesive tape to remove the surface part. The surface parts of the aggregate samples were also characterized (GA-Ar1800-surf and GA-Et1800-surf).

3.2.3 Preparation of a composite sponge of reduced graphene oxide and cellulose nanofiber

CNF was prepared by the TEMPO method and used as received from DKS Co. [57]. It featured a high aspect ratio of 4−10 nm in diameter and 1 μm in length. The GO dispersion was blended with CNF in a mixer for 2 min at 10000 rpm and frozen in a freezer at −10 °C overnight, followed by pumping for 2 days under chamber pressures of about 100 Pa. The total mass fraction of the dispersion was 1 wt% with a mass ratio of GO: CNF = 4:6. The obtained GO/CNF sponges were thermally treated for repair and reduction at 1500 °C in ethanol/Ar gas. This composite sponge was named GCS-Et1500.

A CNF sponge without GO was also prepared for comparison. CNF was blended with water in a mixer for 2 min at 10000 rpm and frozen in a freezer at −10 °C overnight, followed by pumping for 2 days. The total mass fraction of dispersion was 1 wt%. The obtained CNF sponges were thermally treated for repair and reduction at 1500 °C in ethanol/Ar gas. This CNF sponge was named CS-Et1500.

3.2.4 Characterization

Raman spectra were obtained by LabRAM HR-800 UV (Horiba Jobin Yvon) with an excitation laser wavelength of 532 nm, power of 1 mW, and spot size of 1 μm. The Raman spectra of GA-Et1800, GA-Et1800-surf, GS-Ar1800-surf, GS-Ar1800, GS-Et1800-surf, GS-Et1800, and GS-Et1650 were obtained by averaging spectra measured at five random spots. Raman spectra of GS-Et1500 and GCS-Et1500 were averaged for 100 random spots. Note that the ratios of I(D)/I(G) and I(G′)/I(G) was obtained by averaged spectra, so there was no standard deviation as there was only one ratio value per sample. The fraction of the randomly stacked structure was calculated by G′-band fitting since the G′-band is sensitive to structural changes that are vertical to the graphene plane [84, 96]. The G′-band profile was composed of several peaks originating from both randomly stacked and AB-stacked structures [84]. Note that G′-band is also called 2D-band in the literature [82]. For distinction from two-dimensional (2D), the notation G′-band was used in this paper. Details of the fitting process are described in the next section. Images of scanning electron microscopy (SEM) were taken by VE-8800 (Keyence) at an acceleration voltage of 15 kV and a working distance of about 33 mm.

3.3 Results and discussion

3.3.1 Effect of accessibility of ethanol-derived species on the random-stacking fraction of graphene

The Raman spectra of the as-prepared rGO sponge and aggregate samples were measured with an exposure time and accumulation of 15 s and 10 times, respectively (Fig. 3.2(a)). The G-band and D-band of these samples were observed around 1580 cm^{-1} and 1350 cm^{-1}, respectively. The former derives from the in-plane stretching mode of the hexagonal lattice of graphene, and the latter originates from the hexagon-breathing mode activated through the presence of lattice defects [97]. The intensity ratio of the D-band to the G-band, I(D)/I(G), which corresponds to the defect density of graphene, ranged 0.09–0.37. Note that the relationship between D-band intensity and defect density is classified into two different stages depending on defect density, namely interdefect distance. In the case of a small interdefect distance less than ~3 nm,

D-band intensity decreases with increasing defect density, named as stage 1, whereas in the case of a large interdefect distance larger than ~3 nm, D-band intensity increases with increasing defect density, named as stage 2 [81]. Stage 1 and stage 2 can be distinguished by the broadening of D-band. The full width at half maximum of the D-band of our samples ranged 35–59 cm^{-1}, indicating that they were on stage 2 [47, 98]. The narrow D-band shapes and the low I(D)/I(G) ratios confirm that the present graphene samples have much lower defect density than rGO obtained by chemical reduction [81] or annealing in ethanol at ~1000 °C [99-101]. It should be noted that the rGO formed by chemical reduction dose not proceed to stage 2 but remains in stage 1. The result indicates the ultrahigh temperature process is effective in producing highly crystalline graphene. SEM images showed a dense and flat structure of the aggregate sample, while a porous structure and folds were observed on the thermo-treated rGO sponge (Figs. 3.2 (b) and (c)), confirming that freeze-drying successfully forms a high surface area structure. The porous structure and folds indicate that it may be difficult to grow an additional layer of graphene. SEM image of the GO sponge was not taken, because the functional groups of GO are easy to cross-link, resulting in deformation of the porous structure and aggregation of pore walls when the GO sponge was cut in a similar manner to that of the rGO sponge. Note that the D band originates from both edge area and point defect [102], which will be analyzed in details in a future work.

The I(D)/I(G) ratios for the surface area of ethanol-treated aggregate samples (GA-Et1800-surf) and sponge samples (GS-Et1800-surf) indicated similarly low defect densities (I(D)/I(G) of 0.09 and 0.14, respectively (Fig. 3.2 (a)). The internal area of the aggregate sample and sponge sample under the ethanol condition (GA-Et1800 and GS-Et1800, 0.32 and 0.36), and the surface area of aggregate samples and sponge samples under the Ar gas condition (GA-Ar1800-surf and GS-Ar1800-surf, 0.37 and 0.26) showed relatively high I(D)/I(G) ratios compared with the surface of the samples treated under ethanol condition (GA-Et1800-surf and GS-Et1800-surf). These results indicated that the behavior of defect healing depends mainly on the accessibility of ethanol-derived species to GO instead of its morphology.

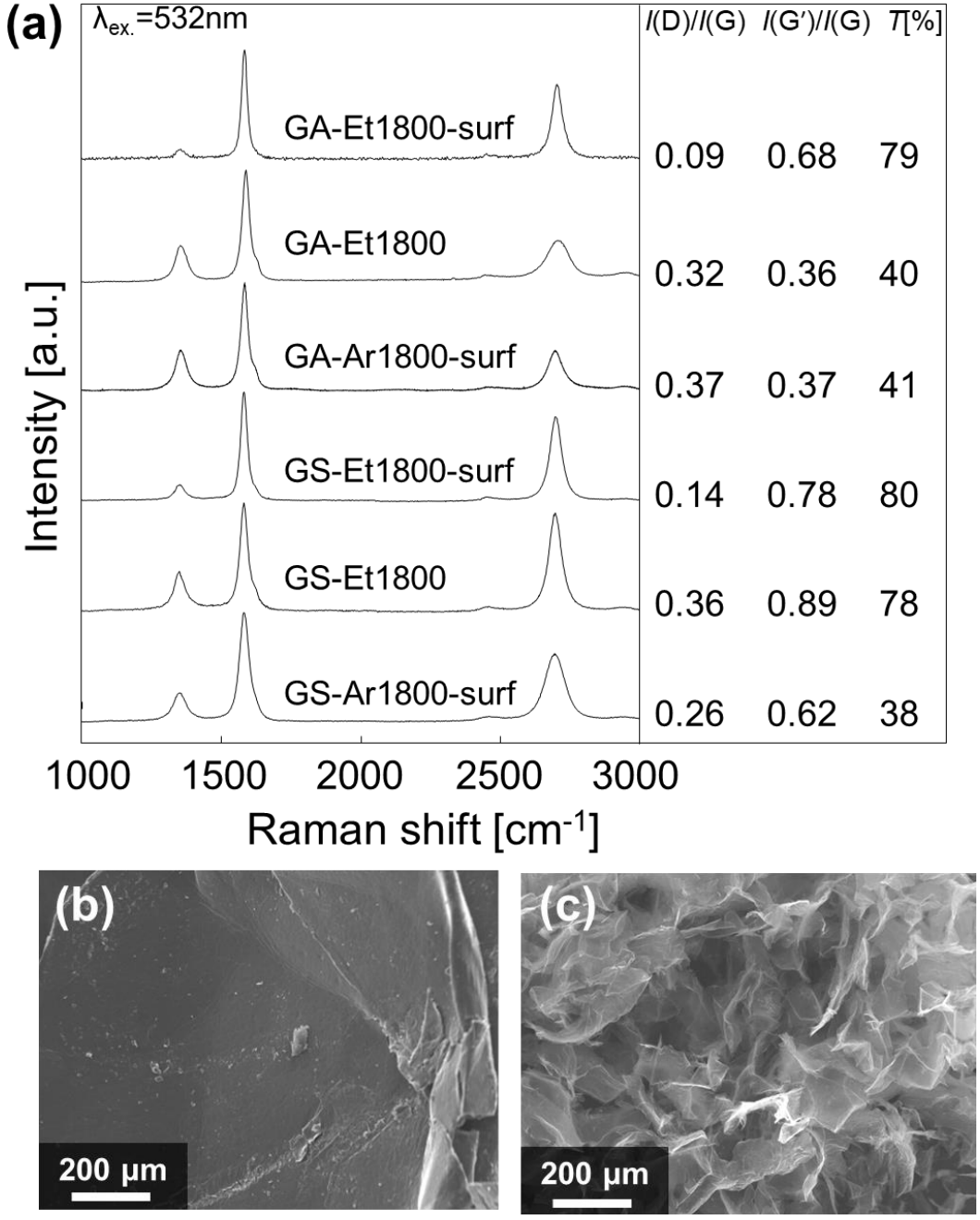

Figure 3.2 (a) Raman spectra of GA-Et1800-surf, GA-Et1800, GA-Ar1800-surf, GS-Et1800-surf, GS-Et1800, and GS-Ar1800-surf. D-band, G-band, and G′-band are observed at ~1350 cm^{-1}, 1580 cm^{-1}, and 2700 cm^{-1}, respectively. Intensity ratios of D-band to G-band, I(D)/I(G), G′-band to G-band, I(G′)/I(G), and random-stacking ratio, T, obtained from the G′-band analysis are displayed to the right of the corresponding spectra. (b, c) SEM images of (b) GA-Et1800-surf and (c) GS-Et1800 [5].

The G′-band of the graphene samples was observed around 2700 cm^{-1} with different sharpness and intensity (Fig. 3.2 (a)). The intensity ratio of the G′-band to the G-band, $I(G')/I(G)$, provides information about the interlayer interactions of graphene because the G′-band is sensitive to the layer number and stacking order of graphene [9, 103, 104]. Higher $I(G')/I(G)$ ratios were observed in GA-Et1800-surf, GS-Et1800-surf, and GS-Et1800, indicating a smaller interaction between graphene layers. GA-Et1800 and GA-Ar1800-surf displayed low $I(G')/I(G)$ ratios, suggesting a stronger coupling between adjacent graphene layers, while GS-Ar1800-surf showed a moderate $I(G')/I(G)$ ratio. This was attributed to the fact that rGO layers have a stronger tendency to form an AB-stacked structure in the aggregate shape, even crumples were located on rGO layers. On the other hand, a sponge shape provides a high fraction of the randomly stacked structure with a weak interaction between the graphene layers.

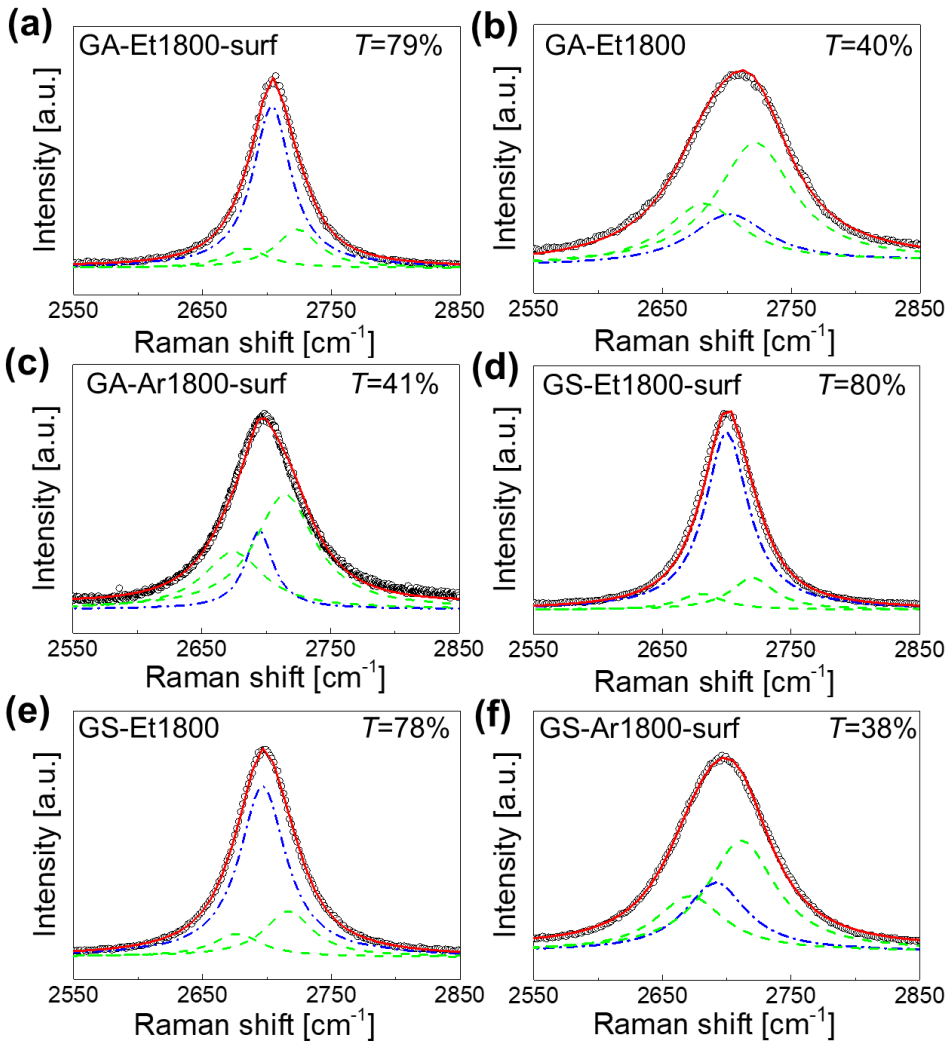

Figure 3.3 G′-band fitting of (a) GA-Et1800-surf, (b) GA-Et1800, (c) GA-Et1800-surf, (d) GS-

Et1800-surf, (e) GS-Et1800, and (f) GS-Ar1800-surf, which provides randomly stacked structure ratio, *T*. Black open circles denote the measured spectra. Blue dashed-dotted curves denote the G'_{2DA} components originating from the randomly stacked structure of graphene, while the two green dashed curves denote the G'_{3DA} and G'_{3DB} components derived from the AB-stacked structure. Red solid curves are the sum of the blue and green curves [5].

Via stacking order analysis based on the G′-band [84], as noticed in section 2.3.1, GA-Et1800-surf, GS-Et1800-surf, and GS-Et1800 displayed high *T* values of 79%, 80%, and 78%, respectively (Fig. 3.3). By contrast, GA-Et1800 showed a low *T* value of 40%, that is, it had a high AB-stacking fraction. Although AB-stacking is a thermodynamically stable structure, the superior properties originating from single-layer graphene are degraded. The high random-stacking fractions of GA-Et1800-surf, GS-Et1800-surf, and GS-Et1800 indicated that the formation of AB-stacked structure was effectively suppressed, which will be explained in detail in the subsequent paragraph. As shown in Fig. 3.2 (b), the rGO aggregate possessed a dense structure, making the internal area inaccessible for the ethanol-derived species. Relatively low *T* indicates preferential formation of AB stacking structure under Ar environment, even rGO layers were deformed by crumple naturally induced for stacked GO layers. The apparent difference between the surface and internal area of the aggregate samples (GA-Et1800-surf and GA-Et1800, Figs. 3.3 (a) and (b)) indicated that, as expected, the formation of a randomly stacked structure is restrained on the surface and does not occur in the internal area of the aggregate. It should be mentioned that the intensity of G'_{3DB} is directly proportional to the volume of 3D graphitic regions, and the overall intensity from 2D and 3D graphitic regions is proportional to (G'_{3DB} + G'_{2D}) since the intensity ratio of G'_{3DB} to G'_{3DA} is constant ($I(G'_{3DB})/I(G'_{3DA})$~2) [8, 84]. On the other hand, both the surface and internal areas of the sponge samples (GS-Et1800-surf and GS-Et1800, Figs. 3.3 (d) and (e)) showed similarly high fractions of the randomly stacked structure. These results confirmed that the sponge structure provides a higher exposed area of GO flakes for ethanol-derived species, allowing the randomly stacked structure to form even on the inside. For comparison between GA-Et1800 and GS-Et1800, the surface areas (Figs. 3. 3 (a) and (d)) showed a similar result, while the internal area of the sponge sample (GS-Et1800, Fig. 3.3 (e)) had a higher random-stacking fraction under the same reaction conditions. It should be noted that the porous morphology of the GO sponge was not a sufficient factor to obtain high random-stacking fractions. GA-Ar1800-surf and GS-Ar1800 (Figs. 3.3 (a) and (d)), which were

processed with only Ar instead of ethanol/Ar, showed low random-stacking fractions, 34% and 29%, respectively. Thus, the remarkable result of GS-Et1800 was attributed to the effect of ethanol-derived species in the high temperature treatment as well as the accessible surface obtained by the porous structure of the GO sponge. Cooperation between the porous structure, ethanol-derived species, and ultrahigh temperature contributed to the formation of bulk-scale graphene with high crystallinity and high random-stacking fraction.

The formation mechanism of randomly stacked graphene by the ethanol-associated ultrahigh temperature process is discussed by the energy diagram, as shown in Fig 3.4. The GO containing various functional groups constructs a random stacking structure in bulk scale instead of ordered AB stacking in graphite and usual multi-layer graphene because of relatively weak interaction between GO flakes. In this work, graphene in bulk scale was synthesized from GO by the thermal process at high temperature. During the high-temperature process, the functional groups of GO were dissociated and desorbed subsequently from the GO surface, leaving randomly oriented graphene with large numbers of vacancy defects and dangling bonds. Considering GO samples treated under only inert gas, the formed graphene with the vacancy and dangling bonds becomes in a metastable state but remains higher energy level. Consequently, the activation energy barrier to the thermodynamically stable AB stacking [105] is relatively low enough to overcome by thermal excitation around 1800 °C, resulting in the structural transformation from random stacking to AB stacking, and the low randomly stacking fraction of GA-Et1800, GA-Ar1800-surf, and GS-Ar1800-surf. On the other hand, in the case of the thermal process with ethanol addition (GS-Et1800 and GA-Et1800-surf), decomposed ethanol provides reactive species containing carbon and oxygen, which effectively repair the vacancies with dangling bonds and topological defects in reduced GO [54, 99]. The reduced defect density causes the formed graphene with random stacking to fall into the metastable state with a very stable energy level. Consequently, the activation energy barrier to the ordered AB stacking becomes too high to get over by the thermal process at 1800 °C or below, resulting in the formation of turbostratic graphene with low defect density. In this case, the formation of AB-stacked structures showed effective suppression, as indicated by the stacking order analysis results obtained in GA-Et1800-surf, GS-Et1800-surf, and GS-Et1800. It should be noted that the turbostratic graphene formation will be limited for the thermal process under 2000 °C since the turbostratic graphene with random stacking will also turn into the most stable AB stacking graphene [84] by thermal

excitation above 2000 °C as the result of overcoming the activation barrier. It should also be pointed out that the rGO treated in pure Ar (e.g., GS-Ar1800-surf) possesses higher defect density and a higher fraction of AB stacking compared with GO treated in the ethanol environment (e.g., GS-Et1800-surf) according to the results of Raman analysis in Fig. 2 (a). This result means defects remaining after the thermal process at 1800 °C should not hinder the transition to AB-stacking but may assist the process, possibly due to a lower energy barrier for the rearrangement of the chemical bonds.

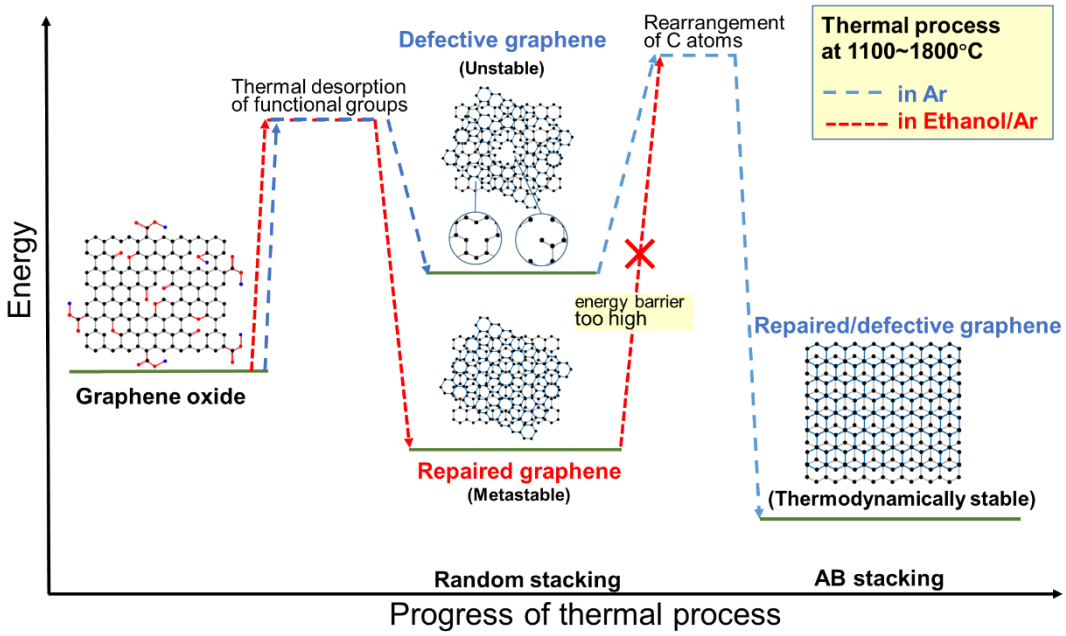

Figure 3.4 Energy diagram for the formation of graphene with random stacking from graphene oxide by the thermal process [5].

3.3.2 Effect of process temperature on the random-stacking fraction of graphene

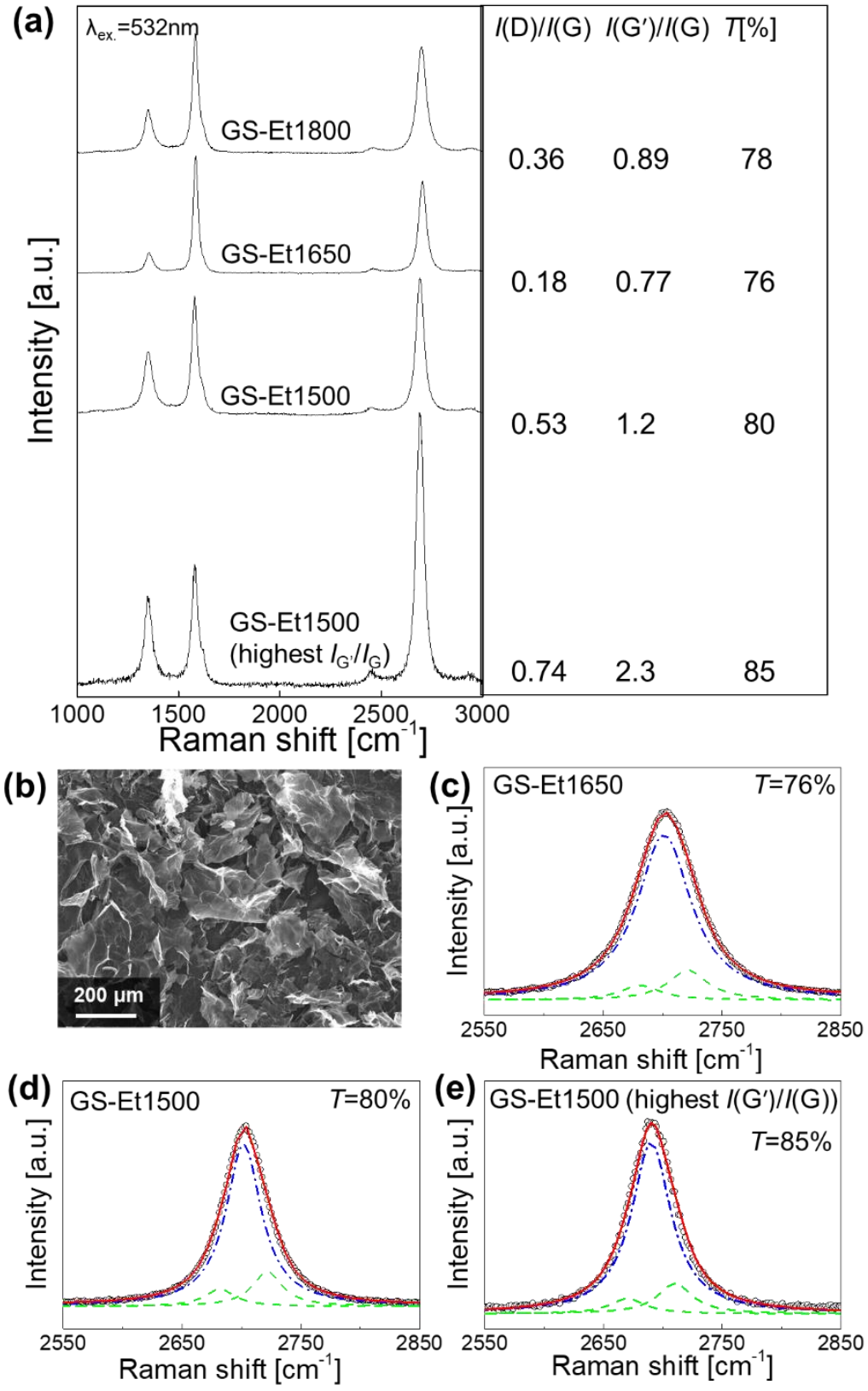

Figure 3.5 (a) Raman spectra of GS-Et1800, GS-Et1650, GS-Et1500, and GS-Et1500 with the highest $I(G')/I(G)$ ratio. Characteristic ratios are indicated to the right of the corresponding spectra. (b) SEM image of GS-Et1500. (c–e) G′-band fitting of (c) GS-Et1650, (d) GS-Et1500,

and (e) GS-Et1500 with the highest $I(G')/I(G)$ ratio. Random-stacking fraction, T, is denoted in the graphs [5].

Multilayer graphene tended to form an AB-stacked structure under a higher temperature process, leading to a higher interlayer interaction and lower G′-band [84, 105]. We tried to decrease the AB-stacking fraction by restraining the movement of the graphene flakes. Reducing the process temperature to 1650 °C or 1500 °C (GS-Et1650 and GS-Et1500) was attempted to increase the fraction of random stacking. Raman spectra of GS-Et1500 were measured with 5 s of exposure time and 5 times for accumulation at each of the 100 spots. The $I(D)/I(G)$ ratios of GS-Et1650 and GS-Et1500 were 0.18 and 0.53, while the $I(G')/I(G)$ ratios were 0.77 and 1.2, respectively (Fig. 3.5 (a)). The low $I(D)/I(G)$ ratio of GS-Et1650 displayed a similar low defect density as the 1800 °C sample (GS-Et1800-surf). By contrast, GS-Et1500 showed a high $I(D)/I(G)$ ratio, indicating relatively low crystallinity. The $I(G')/I(G)$ ratio of GS-Et1650 was close to that of the 1800 °C sample (GS-Et1800), suggesting that GS-Et1650 had a similar interlayer interaction with GS-Et1800. The $I(G')/I(G)$ ratio of GS-Et1500 was higher than those of GS-Et1650 and GS-Et1800, revealing less coupling between the graphene layers. The $I(G')/I(G)$ and $I(D)/I(G)$ exhibit a certain fluctuation for each measurement point, as shown in Fig. 3.6. It should be noted that the highest $I(G')/I(G)$ ratio of 2.3 was observed at a measurement spot of GS-Et1500 (Fig. 3.5 (a), bottom). The SEM image confirmed that the sponge maintained a porous structure after 1500 °C treatment (Fig. 3.5 (b)), which is similar to that of GS-Et1800 (Fig. 3.2 (c)). Analysis of the G′-band of GS-Et1650, GS-Et1500, and GS-Et1500 with the highest $I(G')/I(G)$ ratio showed that the random-stacking fractions were 76%, 80%, and 85%, respectively (Figs. 3.5 (c–e)). The random-stacking fraction increased as the reaction temperature decreased. The high random-stacking fraction and the highest G′ band of GS-Et1500 suggested that the sample under the reaction condition was far from crossing the energy barrier for AB-stacked structure and preserved a more randomly stacked structure at 1500 °C.

As shown in Fig 3.6, the majority of the data points are located within the ranges of 0.9–1.6 for $I(G')/I(G)$ and 0.45–0.65 for $I(D)/I(G)$. The standard deviations of $I(G')/I(G)$ and $I(D)/I(G)$ are 0.1 and 0.27, respectively. The origin of the variation is attributed to the spatially different morphology of the sponge structure formed during the freeze-drying process. While the porous morphology assists the ethanol-mediated

defect healing, locally aggregated graphene in some regions might be less healed. Therefore, a further enhancement of uniformity is possible by improving the forming process of the sponge structure.

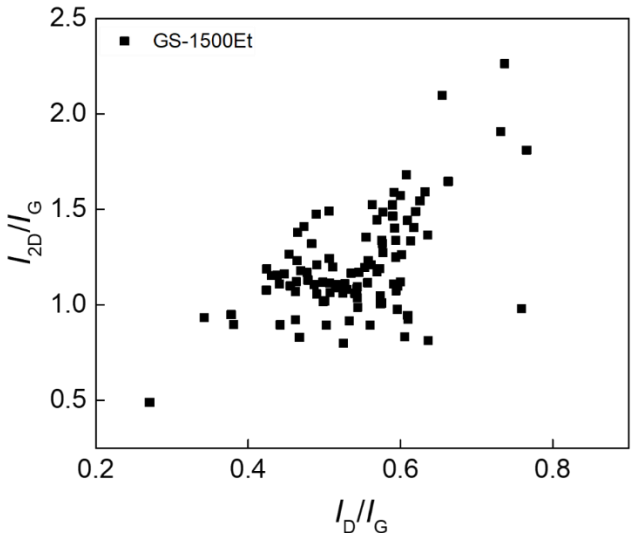

Figure 3.6 Distribution of *I*(D)/*I*(G) and *I*(G′)/*I*(G) for each measurement spot of the GS-Et1500. [5].

3.3.3 Increase of the random-stacking fraction of graphene by the addition of CNF as a spacer

We investigated the impact of a spacer to physically prevent graphene from stacking on the interlayer interaction in bulk-scale graphene. Because a high *I*(G′)/*I*(G) was achieved in GS-Et1500, the same treatment condition was employed in this experiment. Based on the advantages of CNF, it was added as a spacer into bulk-scale graphene (GCS-Et1500). The Raman spectra of GCS-Et1500 were measured with 5 s of exposure time and 5 times for accumulation at each of the 100 spots. A pure CNF sponge (CS-Et1500) was prepared as the control using the same mixing, freeze-drying, and thermal treatment conditions. The Raman spectra of CS-Et1500 were measured with 5 s of exposure time and 5 times for accumulation at each of the 30 spots. As shown in Fig. 3.7 (a), the *I*(D)/*I*(G) ratio of GCS-Et1500 was 0.60, while the *I*(G′)/*I*(G) ratio was 0.86. CS-Et1500 showed 1.32 of *I*(D)/*I*(G) and 0.26 of *I*(*G′*)/*I*(G). The SEM image of GCS-Et1500 suggested that the sponge also maintained a porous structure

(Fig. 3.7 (b)), which was very similar to the sponge samples treated in ethanol, such as that of GS-Et1800 (Fig. 3.2 (b)). The CNF structure was not observed by SEM because it was altered through graphitization during the ultrahigh temperature process. The SEM image of the GO/CNF sponge was not taken due to the cross-linking of functional groups, which is the same reason mentioned earlier. By adding CNF as a spacer, GCS-Et1500 showed a higher I(D)/I(G) and a lower I(G′)/I(G) than the sample without CNF (GS-Et1500). This high D-band intensity was attributed to the graphitization of CNF and the formation of amorphous carbon. The G′-band of GCS-Et1500 was analyzed to investigate the stacking order of the composite sponge of graphene and CNF by the analysis procedure described in section 3.3.1 [84]. As shown in Fig. 3.7 (c), the obtained T value was 93%. It should be noted that the T value here does not simply correspond to the fraction of the randomly stacked structure but indicates the fraction of two-dimensional graphene, which includes randomly stacked graphene and non-stacked graphene separated by the spacer. The high occupation of the two-dimensional graphite-originating peak for GCS-Et1500 indicated that the addition of CNF further suppressed the formation of the AB-stacked structure. It should be emphasized that the T value of GCS-Et1500, 93%, significantly surpassed that of GS-Et1500, 80%. This result implied that inserting CNF physically prevented the direct stacking of the graphene layers.

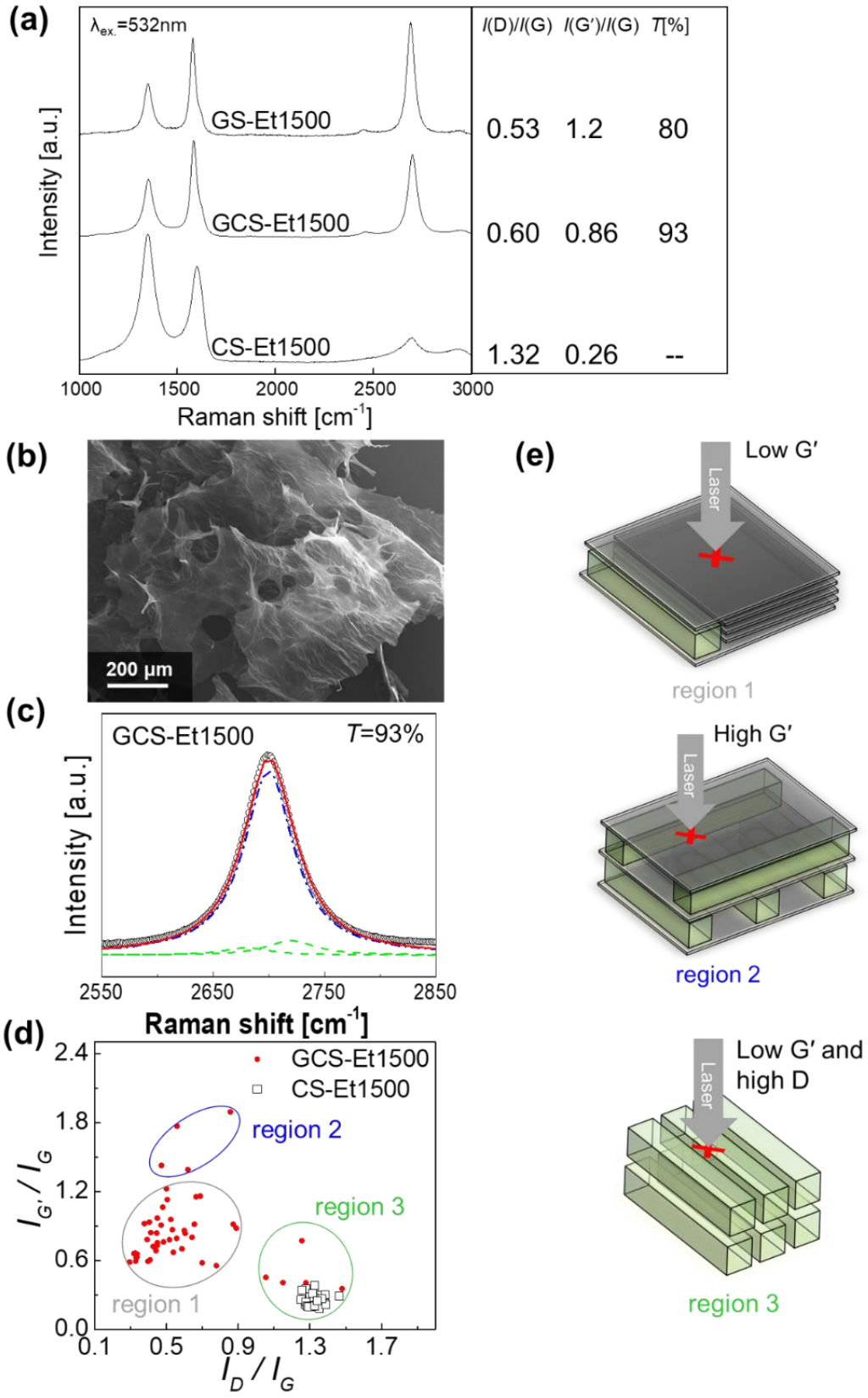

Figure 3.7 (a) Raman spectra of GS-Et1500 and GCS-Et1500. Characteristic ratios are indicated to the right of the corresponding spectra. (b) SEM image of GCS-Et1500. (c) G′-band fitting of GCS-Et1500. (d) Distribution of I(D)/I(G) and I(G′)/I(G) for each measurement spot of the

GCS-Et1500 (red dot) and CS-Et1500 (hollow square). (e) Schematic images of three different situations of GCS-Et1500, indicating stacked graphene (region 1), graphene intercalated with CNF (region 2), and aggregate of CNF (region 3) [5].

The spatial variation of the GCS-Et1500 sample was investigated. The $I(G')/I(G)$ and $I(D)/I(G)$ ratios of each measurement spot of GCS-Et1500 are plotted in Fig. 3.7 (d). Most of the Raman results were located at the grey oval circle (region 1), but some Raman results of GCS-Et1500 with a high $I(G')/I(G)$ (region 2) or a low $I(D)/I(G)$ (region 3) were observed outside region 1. As schematically illustrated in Fig. 3.7 (e), this result can be explained as follows. As for region 2 in Fig. 3.7 (d), CNF was perfectly dispersed and played the spacer role well. After the ultrahigh temperature process, CNF was changed into graphite material [106] and remained between graphene layers. Graphene layers were physically separated by the graphitic material, so that interlayer interactions were suppressed. Thus, $I(G')/I(G)$ was high. However, region 1 showed lower $I(G')/I(G)$ since CNF was insufficient in these spots of the sample, resulting in directly stacked graphene. Stacked graphene was also measured by X-ray diffraction (Fig. 3.8). Similar to that of GS-Et1500 (Fig. 3.6), these two results were mainly attributed to the graphene in the sponge. Additionally, due to the formation of CNF aggregates, region 3 exhibited a high $I(D)/I(G)$ ratio and low $I(G')/I(G)$ ratio, which was comparable to the pure CNF sample (CS-Et1500). The high defect density and strong interlayer interaction were features of graphitized CNF. Improving the dispersion of CNF should realize a more uniform formation of bulk-scale graphene with a low interlayer interaction.

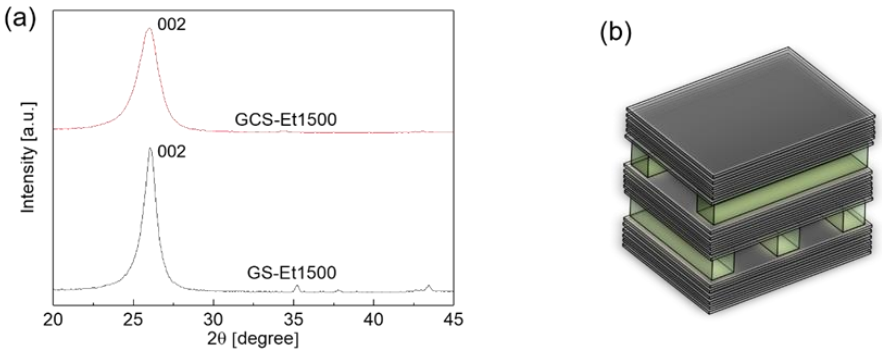

Figure 3.8 (a) XRD result of GS-Et1500 and GCS-Et1500. (b) Schematic structure of GCS-

Et1500 [5].

XRD measurement was conducted on GS-Et1500 and GCS-Et1500 (Fig. 3.8 (a)). 002 peak from GS-Et1500 and GCS-Et1500 were observed. *K* value of turbostratic graphene was 0.9 on the c-axis [86]. The average layer distances of GS-Et1500 and GCS-Et1500 were 0.342 nm and 0.343 nm, which were larger spacing than that of graphite (0.335 nm). GCS-Et1500 showed larger layer distances and smaller crystallite sizes on the c-axis, indicating that CNF was intercalated between graphene layers. The nanostructure of our sample can be schematically depicted in Fig. 3.8 (b), in which graphene layers are not individually separated by CNF, but small stacks of graphene are separated by CNF.

3.4 Conclusion

By freeze-drying a GO dispersion and an ethanol-mediated reduction at ultrahigh temperature, a graphene sponge with a high random-stacking fraction for both surface and internal areas was realized. This feature is in sharp contrast to GO aggregate samples, where the formation of AB stacking cannot be suppressed in the internal area. The high random-stacking fraction in internal regions is attributed to the increased accessible area of the porous graphene sponge for ethanol-derived species. We optimized the reduction conditions and confirmed that the strong and sharp G′-band from graphene sponge is reduced at 1500 °C, which is indicative of a weak interlayer interaction. Additionally, CNF was introduced as a spacer into a GO sponge to separate the graphene layers and to avoid direct stacking. The blending of CNF with the GO dispersion further reduces the AB-stacked fraction. Although there is still room to improve mixing to achieve a higher $I(G')/I(G)$ ratio and homogeneity, the proposed scheme prevents strong interlayer stacking in bulk-scale graphene. Consequently, it should realize the scalable production of high-performance bulk-scale graphene in which the superior properties of single-layer graphene are effectively preserved.

Chapter 4: Stacking order reduction in multilayer graphene by inserting nanospacers

4.1 Background

Graphene has attracted wide attention as a two-dimensional (2D) material for its various excellent properties, such as high carrier mobility, electrochemical performance [1], optical transparency [2], thermal conductivity [107], and mechanical strength [6]. Many of these properties are attributed to the unique electronic structure derived from a one-atom-thick honeycomb lattice of single-layer graphene. However, the electrical, mechanical, and other performances were limited by the thinness and small volume of a single-layer graphene flake. Thus, scaling up high-quality graphene toward bulk-scale, which is composed of plenty of graphene flakes [108], is necessary for practical applications [13-18, 93].

Considering mass-production compatibility and structure controllability, a promising approach for producing bulk-scale graphene is beginning with GO and then reducing it into rGO. Hydro-thermal or chemical methods are the most common approaches for reduction [45, 46]. However, they produce rGO that suffers from a high density of defects that remain in reduction, such as vacancy. Alternatively, the defect problem can be solved by high temperature treatment of GO [49], while it brings about a problem regarding the stacking structure of multilayer graphene. The thermodynamically stable AB-stacked structure [50] is spontaneously formed at high temperature, which causes a strong interlayer interaction between graphene layers and results in degradation of the superior properties of single-layer graphene. Conversely, theoretical calculations have predicted that randomly stacked graphene, where each layer is vertically stacked and randomly rotated, can preserve the electronic band structure similar to that of single-layer ones [11]. This is due to the smaller interactions between adjacent graphene layers. Compared to AB-stacked graphene, randomly stacked graphene possesses superior properties for maintaining a single-layer-like electronic structure; this has been confirmed in experimental studies [51, 109, 110]. AB-stacked bilayer graphene and individual flakes of rotationally stacked multilayer graphene indicate carrier mobility of 4.4×10^3 cm^2 $V^{-1} \cdot s^{-1}$ and 7×10^4 cm^2 $V^{-1} \cdot s^{-1}$ [52], respectively. The development of randomly stacked graphene manufacturing methods is essential for the realization of daily applications of graphene.

Due to the unique reaction pathway, the random-stacking structure of graphene is effectively maintained by adding ethanol vapor during the high-temperature treatment of GO [54]. Ethanol vapor at high temperatures generates carbon atoms and OH radicals (hereafter called “ethanol-derived species”), which respectively function as a carbon source and an etchant during the reduction process. They can provide efficient defect healing for GO without causing intense stacking order rearrangement. High carrier mobility was achieved by utilizing this reduction method for few-layer rGO on substrates [100]. However, this method faced the following problem: the repairing and formation of randomly stacked structures were limited to the surface region when preparing bulk-scale graphene. Preparing GO with a porous structure before the ethanol-associated ultrahigh temperature process resolved this issue [5]. Such graphene sponge was prepared via freeze-drying of GO dispersion and the ethanol-associated thermal treatment. According to the Raman spectra analysis, both the internal and surface regions of graphene reached ~80% of the random-stacking fraction. To further improve the random-stacking fraction of rGO, we conducted a preliminary experiment on adding CNF as a spacer [5]. This spacer aims to physically prevent the direct layer stacking of graphene. In addition to the previously mentioned randomly stacked graphene structure, inserting the spacer between graphene layers is expected to reduce the strong interlayer interaction caused by ordered stacking. Also, the accessibility of ethanol-derived species in the samples can be improved during the thermal treatment, which suppresses the formation of AB stacking. Choosing the spacer was based on the fact that CNF has high water solubility and could transform into inert materials at high temperatures without reacting with GO [64, 66]. Considering the 2D structure of graphene and the one-dimensional (1D) structure of CNF, this composite sponge can be regarded as a 2D/1D mixed-dimensional heterostructure, where the material property is designed with the combination of different building blocks [67]. The rGO/CNF sample indicated a higher random stacking fraction than the pure rGO sample. However, the mechanism of stacking order reduction in the multilayer graphene remained unclear. Thus, a systematic study on spacer concentration and the change in stacking structure along the process sequence is necessary for understanding the stacking mechanism and further controlling the stacking order of graphene.

Another spacer candidate is ND, a zero-dimension (0D) material attracting wide attention for its potential applications in catalysis [68], bio-sensor [69], and so on [70]. The detonation method is wildly used in the industrial preparation of ND. It is followed by an oxidation process that removes impurities on the surface [71-73]. ND

particles prepared by the detonation method possess a three-layered structure. In the inner region of ND, a core and an intermediate shell are made up of a cubic diamond crystal (sp^3-hybridization) and the partial layer of a fullerene-like shell (sp^2-hybridization) [74], respectively. The surface layer of ND has oxygen-containing groups, and the mentioned oxidation process can enhance hydrophilicity [73]. Because both ND and GO show a negative Zeta charge, a stable mixed dispersion with electrostatic repulsion is expected. In contrast to the 1D structure of CNF, ND is a 0D material with a low aspect ratio, making the formation of the micrometer-scale agglomerates more difficult. Additionally, ND transforms into a carbon nano onion, that is the nested sp^2 carbon shells, at high temperature [76], which is inert and does not react with graphene during the thermal treatment. These advantages make ND a promising candidate as a spacer for graphene to produce 2D/0D mixed-dimensional heterostructures with a low stacking order.

In this chapter, we propose a method of reducing the stacking order in multilayer graphene using nanomaterials with different dimensions as spacers. CNFs or NDs with varied concentrations were added to the GO dispersion, which is the precursor of the GO sponge. After the freeze-drying and ethanol-associated thermal treatment, the bulk-scale multilayer graphene sponge was obtained. The stacking structures of the graphene samples were examined with Raman spectroscopy and XRD. The random-stacking fraction of the samples was evaluated by G′-band analysis of Raman spectra. The result indicated a remarkable decrease in the stacking order of graphene with a low concentration of spacer. Then, to investigate the periodic structure of the graphene samples, the XRD analysis was utilized to evaluate the crystalline size to the stacking direction as well as the layer distance. We found that the crystalline size decreased drastically with the small amount of spacers and then decreased gradually with the increase in the spacer concentration. The gradual change in the stacking order was analyzed in detail with a two-component model. Furthermore, the XRD analysis on the pre-thermal treatment samples confirmed that the layer number of stacked graphene was effectively suppressed by the spacers during the treatment. ND provided lower graphene stacking order than CNF, which was explained by the fact that the former was less aggregated in the samples. To sum up, inserting nanospacers, especially NDs with high concentrations, can effectively reduce the stacking order in multilayer graphene.

4.2 Experiment section

4.2.1 Preparation of GO, GO/CNF, and GO/ND dispersion

The 1 wt% GO/water dispersion was prepared from bulk graphite by a modified Hummers' method [77]. The GO flake size was evaluated to be around 10 μm by optical microscopy. The diluted GO dispersion weight percentage was 0.8 wt%, which was equal to that of the GO/spacer composite samples.

The CNFs were prepared by the TEMPO method and used as received from DKS Co. They featured a high aspect ratio of 4−10 nm in diameter and 1 μm in length. The GO dispersion was blended with CNFs in water [5]. The GO mass fraction of the dispersion was fixed at 0.8 wt%, while the CNF mass fraction varied between 0.01, 0.02, 0.05, 0.1, and 0.2 wt%.

The NDs were prepared by the detonation method and used as received from Nippon Kayaku Co. They featured an average of 5 nm in diameter. The GO dispersion was blended with NDs in water. The GO mass fraction of the dispersion was fixed at 0.8 wt%, while the ND mass fraction varied between 0.01, 0.02, 0.05, 0.1, and 0.2 wt%.

4.2.2 Preparation of GO, GO/CNF, and GO/ND Sponges by freeze-drying

A lab-made vacuum drying system was used for the freeze-drying process [5]. To prepare 1 cm^3 cube sponges of GO with or without spacers, the dispersion was poured into an ice tray and then frozen using liquid nitrogen. The tray was installed in the vacuum drying system, and its chamber was pumped for 72 hours. Pumping causes the water in the frozen dispersion to sublimate, leaving the network structure as a GO or composite sponge for the following thermal treatment. The sponges of 0.8 wt% GO, 0.8 wt% GO mixed with 0.01 wt% CNF, and 0.8 wt% GO mixed with 0.01 wt% ND were used for the XRD analysis without the thermal treatment, respectively labeled as GO, GO/CNF, and GO/ND.

4.2.3 Thermal treatment

The GO and composite sponges were thermally treated in ethanol/Ar under ultra-high temperature conditions for repairing and reduction. The ultrahigh temperature process was performed at 1500 °C using a tubular electric furnace (HT1500-50-32P, HEAT TECH Co.). Its chamber was maintained at low pressure via a vacuum pump. During the temperature rise, 20 sccm of Ar was introduced under a total pressure of 34.7 Pa. After reaching the set temperature, the thermal treatment was conducted by flowing 98 sccm of Ar and 2 sccm of ethanol under a total pressure of 133 Pa. The obtained rGO sample from pure GO was called as G-0, while those from GO mixed with 0.01 wt%, 0.02 wt%, 0.05 wt%, 0.1, and 0.2 wt% of CNFs (NDs) were named GC-1, GC-2, GC-3, GC-4, and GC-5 (GD-1, GD-2, GD-3, GD-4, and GD-5), respectively. Additionally, a pure GO sponge was prepared by using an infrared radiation furnace (SR1800G-S, THERMO RIKO Co.) at 1800 °C under an Ar environment as reported in our previous study [5], and the sample was named as G-1800-Ar and used as a reference.

4.2.4 Characterization

The obtained samples were ground in a mortar and characterized by Raman spectroscopy and XRD. Raman spectra were obtained by LabRAM HR-800 UV (Horiba Jobin Yvon) with an excitation laser wavelength of 532 nm, power of 1 mW, and a spot size of ~0.7 μm. They were obtained at 20 random spots for each sample, and the ratios of I(D)/I(G) and I(G′)/I(G) were calculated by each individual spectrum. Then, the spectra were averaged for further stacking analysis. The G′-band is sensitive to the vertically changed structure of the graphene plane. Thus, the volume fraction of a randomly stacked structure can be analyzed by G′-band fitting [84, 96]. The G′-band profile is the sum of several peaks originating from both random-stacked and AB-stacked structures. Note that in the literature, the G′-band is also represented as the 2D-band [82]. To distinguish this Raman band from two-dimensional (2D), the G′-band notation was used in this paper. Details of the fitting process are described in the next section and in our previous paper [5]. The XRD measurements for the G-0, GC, and GD series samples were conducted using Ultima IV (Rigaku Co.) via a standard Cu-Kα source having λ = 1.5406 nm, with 40 kV and 40 mA. The accuracy of XRD

measurement was confirmed by measuring silicon powders and detecting Si 111 peak at 28.4°. The measurements for the samples without thermal treatments (GO, GO/CNF, and GO/ND) were conducted by SmartLab (Rigaku Co.) using a standard Cu-Kα source of λ = 1.5406 nm, with 40 kV and 40 mA. The scanning speed from 10 to 20° was 0.5°/min. To evaluate the ordered structures of stacked GO and rGO with and without spacers, the XRD patterns were analyzed by Bragg's and Scherrer's equations. SEM images were taken by VE-8800 (Keyence) at an acceleration voltage of 15 kV. Samples before grinding were used for the SEM observation.

4.3 Raman analysis of stacked graphene with spacer

4.3.1 Raman analysis of stacked graphene with CNFs

The structure of the rGO sponge with CNFs as spacers was evaluated by Raman spectroscopy. The Raman spectra of the GC-1, GC-2, GC-3, GC-4, GC-5, and the control group samples, G-0 and G-1800-Ar, were measured as shown in Fig. 4.1(a). The G-band was observed at around 1580 cm^{-1}, while the D-band was around 1350 cm^{-1}. The G-band derives from the in-plane stretching mode of the hexagonal lattice of graphene, and the D-band originates from the hexagon-breathing mode activated by the presence of lattice defects [97]. The intensity ratio of the D-band to the G-band, I(D)/I(G), corresponds to the defect density of graphene [97]. Additionally, the G′-band of the samples was observed at around 2700 cm^{-1} with varying peak shape and intensity. Because the G′-band is sensitive to the layer number and stacking order of graphene [9, 103, 104], the intensity ratio of the G′-band to the G-band, I(G′)/I(G), provides information related to the interlayer interactions of graphene.

The I(D)/I(G) and I(G′)/I(G) ratios of the samples are plotted against the CNF concentration in Fig. 4.1 (b). The I(D)/I(G) ratios of the GC series samples ranged between 0.81−0.88, while that of G-0 was 0.57. The relationship between the D-band intensity and the defect density was classified into two different stages depending on the latter, namely the inter-defect distance [81]. In the case of a distance larger than ~3 nm, the D-band intensity increases with the increase in defect density; this is called stage 1. Whereas in the case of an inter-defect distance less than ~3 nm, the intensity decreases with the increase in defect density; this is named stage 2 [81]. Stages 1 and 2 can be distinguished by the broadening of the D-band. Our samples were in stage 1

because the full width at half maximum (FWHM) of the D-band ranged between 60−70 cm^{-1} [47, 98]. Compared to G-0, GC series samples demonstrated a higher *I*(D)/*I*(G) ratio, indicating that they featured a higher defect density. This increase in D-band intensity was attributed to the change in the structural restoration of GO induced by adding CNFs. The *I*(D)/*I*(G) ratios of the GC series samples were almost constant while the CNF concentration varied, indicating that amorphous carbon formed by incomplete graphitization of CNF did not strongly influence the increase in D-band intensity.

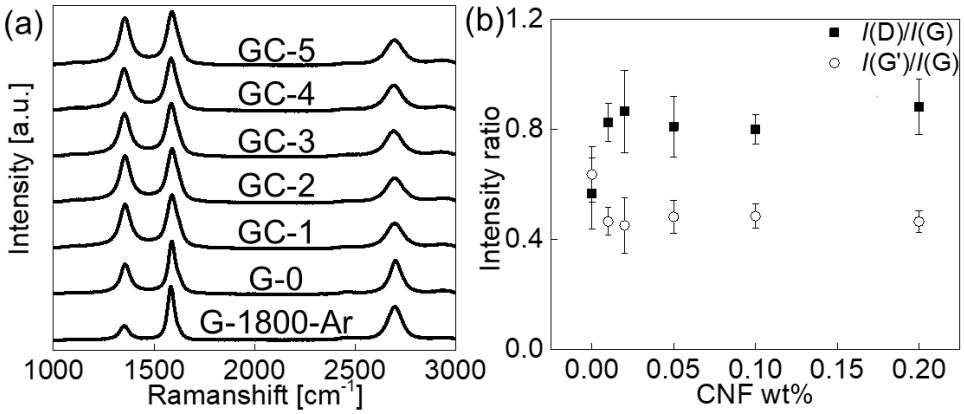

Figure 4.1(a) Raman spectra of the GC series samples, G-0, and G-1800-Ar. (b) Intensity ratios of D-band to G-band, *I*(D)/*I*(G), and G′-band to G-band, *I*(G′)/*I*(G), plotted against the CNF weight percentage (G-0 and GC series samples). Filled squares denote the *I*(D)/*I*(G) ratio, and open circles denote the *I*(G′)/*I*(G) ratio [75].

The *I*(G′)/*I*(G) ratios of the GC series samples (0.45−0.49) were lower than that of G-0 (0.64), and their dependence on the mass fraction of CNF exhibited an opposite trend of *I*(D)/*I*(G). This implies that the increase of defects led to a decrease in the G′-band intensity when the stacking order remained unchanged [111]; thus, the simple comparison of the *I*(G′)/*I*(G) ratio was not suitable for evaluating the stacking order of graphene. Actually, the G′-band was observed to shift slightly to a lower frequency by ~7 cm^{-1} after adding the spacer, corresponding to the increase of the randomly stacking fraction as shown by further analysis of the G′-band described below. To investigate the stacking order of multilayer graphene with CNFs, further analysis on the G′-band was conducted as follows.

As conducted in our previous research, the stacking order of graphene in the bulk-scale samples was evaluated by analyzing the peak shape of the G′-band [5]. According to the research of Cançado et al. [84] and formula (2.1), the fraction of random-stacking structure in the bulk-scale graphene can be calculated. Note that A. Mohapatra et al. [112] provided a new method based on the strong and constant intensity of *I*(G′) for graphene with 100% randomly stacking fraction. This method should be very reliable for defect-free graphene. However, it is not suitable for our research using defective graphene as samples because the *I*(G′) decreases for the increasing defects [113], leading to overestimating the volume of the AB-stacking structure.

Via the stacking order analysis based on the G′-band shape, the control group sample, G-1800-Ar, showed a low T value of 40% [5], as shown in Fig. 4.2 (g). This result indicates the preferential formation of a thermodynamically stable AB-stacking structure at high temperatures without the introduction of ethanol. Another control group, G-0, showed a moderate T value of 75% (Fig. 4.2 (a)), which confirms the ethanol effect on suppressing the formation of the AB-stacking structure [5, 54, 55]. By adding CNFs, GC-1 showed a T value of 87% (Fig. 4.2 (b)), which is higher than that of the spacer-less graphene sample, G-0, obtained with identical high-temperature treatment. Other GC samples (GC-2, GC-3, GC-4, and GC-5) also displayed similar T values, as shown in Fig. 4.2 (c-f), ranging between 85%–90% (Fig. 4.2 (h)). This concluded that the majority of the graphene structures of the GC samples were constructed from randomly stacking layers. The T values of GC series samples did not greatly differ when the CNF concentration increased, which requires further analysis to understand the mechanism of determining random-stacking fractions. Note that although the stacking order can be featured by the G′-band analysis, the thickness of multilayer graphene, which composes the sponges remains unknown using the Raman spectra. Note that the G′ band underwent broadening because of the randomly stacked structure, resulting in varying intensities around 2250 cm^{-1}. Thus, the evaluation of graphene stacking order using XRD analysis will be given in Section 4.4.1.

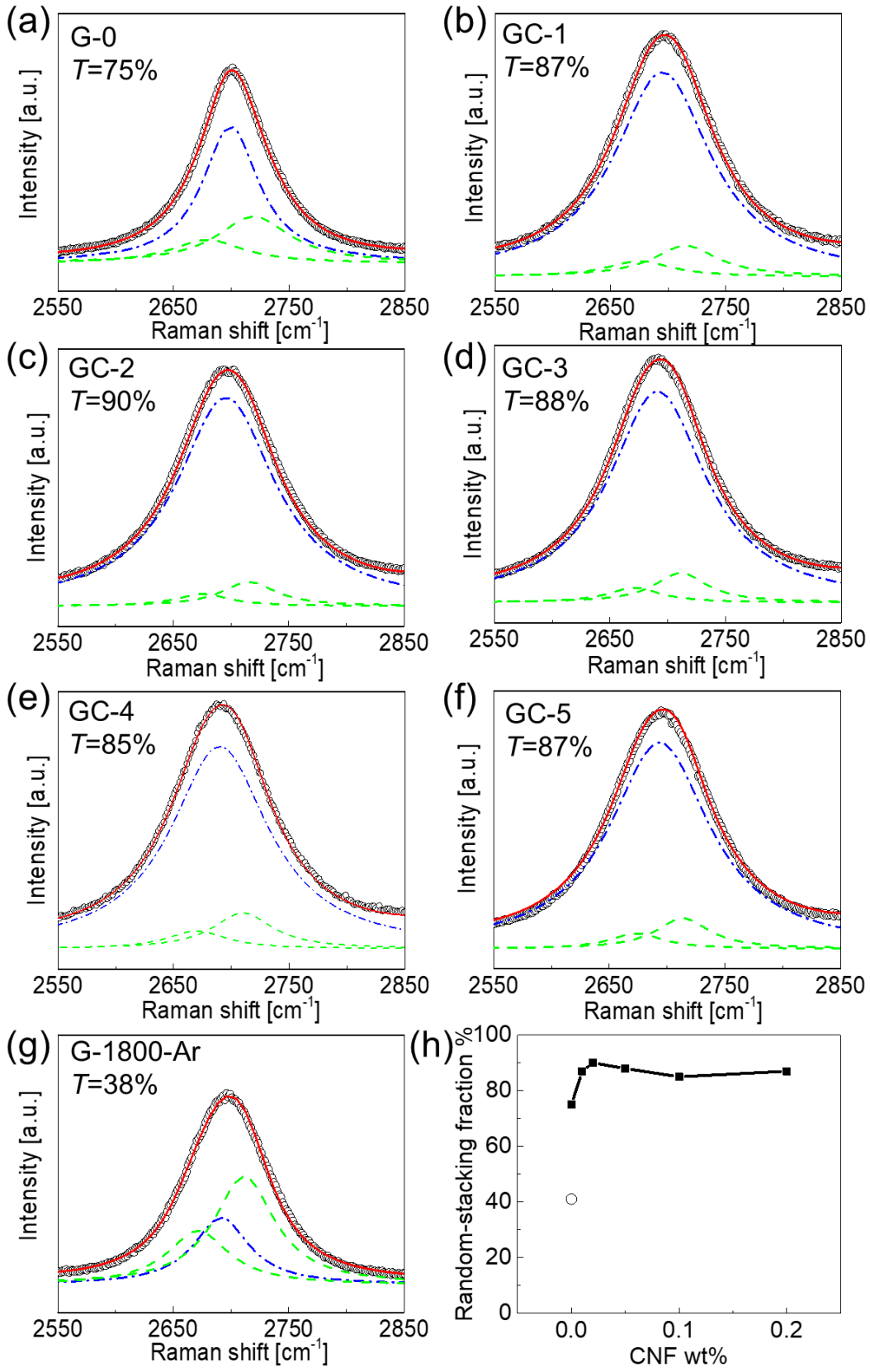

Figure 4.2 (a-g) G′-band fitting of (a) G-0, (b) GC-1, (c) GC-2, (d) GC-3, (e) GC-4, (f) GC-5, and (g) G-1800-Ar, which provides the randomly stacked structure ratio, *T*. Black open circles denote the measured spectra. Blue dashed-dotted curves denote the G'_{2D} components

originating from the randomly stacked structure of graphene, while the two green dashed curves denote the G'_{3DA} and G'_{3DB} components derived from the AB-stacked structure. Red solid curves are the sum of the blue and green curves. (h) Random stacking fraction of samples with different weight percentages of CNF. Filled squares denote the random-stacking fraction of the GC series samples and G-0. The open circle denotes that of G-1800-Ar [75].

4.3.2 Raman analysis of stacked graphene with NDs

Since the ND particles possess a smaller diameter and lower dimensionality than those of CNF, a more effective insertion of ND is expected. Therefore, this study attempted to improve the *T* value of graphene by changing the spacer material to ND. The Raman spectra of GD-1, GD-2, GD-3, GD-4, and GD-5 were measured and plotted with the control groups, G-0, and G-1800-Ar, in Fig. 4.3(a). The G-band was observed to be around 1580 cm^{-1}, while the D-band was around 1350 cm^{-1}. The *I*(D)/*I*(G) ratios of the GD series samples ranged between 0.42–0.65 (Fig. 4.3 (b)). Our samples were on stage 1 because the FWHMs of the D-bands ranged between 50–90 cm^{-1} [47, 98]. The G′-band of the samples was observed to be around 2700 cm^{-1} with varying peak shape and intensity. The *I*(G′)/*I*(G) ratios of GD series samples ranged between 0.45–0.72.

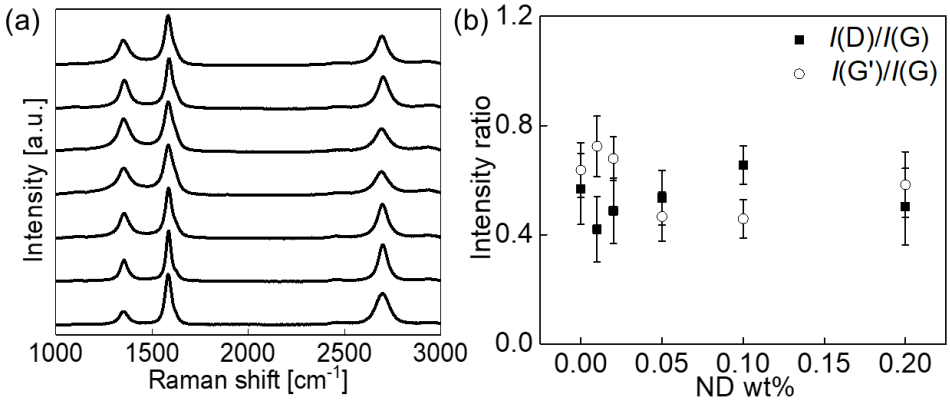

Figure 4.3 (a) Raman spectra of the GD series samples, G-0, and G-1800-Ar. (b) The intensity ratios of D-band to G-band, *I*(D)/*I*(G), and G′-band to G-band, *I*(G′)/*I*(G), plotted against the ND weight percentage (G-0 and GD series samples). Filled squares denote the *I*(D)/*I*(G) ratio, and open circles denote the *I*(G′)/*I*(G) ratio [75].

The G-0 and GD series samples demonstrated similar I(D)/I(G) and I(G′)/I(G) ratios with small fluctuations, indicating that the GD series samples featured a comparably low defect density with G-0. This similar D-band intensity indicated that NDs did not significantly hinder the reduction process nor transform into substances that show a strong D-band. Similarly to the GCs, a slight decrease in the G′-band frequency for the GD samples was observed after adding the spacer. To understand the stacking order, further analysis on the G′-band was conducted as follows.

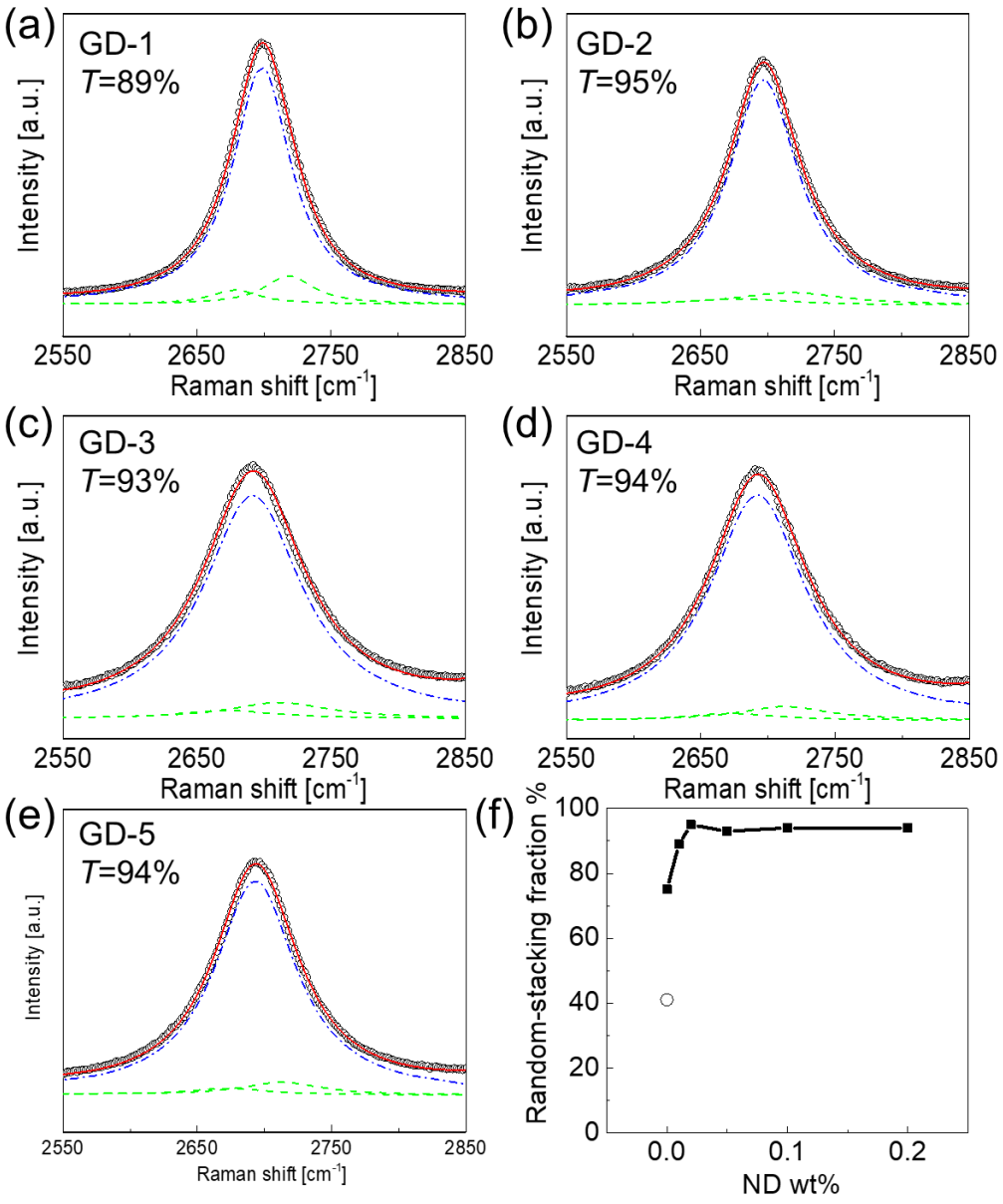

Figure 4.4 (a-e) G′-band fitting of (a) GD-1, (b) GD-2, (c) GD-3, (d) GD-4, and (e) GD-5, which

provides the randomly stacked structure ratio, *T*. Black open circles denote the measured spectra. Blue dashed-dotted curves denote the G'_{2D} components originating from the randomly stacked structure of graphene, while the two green dashed curves denote the G'_{3DA} and G'_{3DB} components derived from the AB-stacked structure. Red solid curves are the sum of the blue and green curves. (f) Random stacking fraction of samples with different weight percentages of ND. Filled squares denote the random-stacking fraction of the GD series samples and G-0. The open circle denotes that of G-1800-Ar [75].

Via the stacking order analysis based on the G′-band shape [84], GD-1 showed a *T* value of 89% (Fig. 4.4 (a)), which is higher than that of the spacer-less graphene sample, G-0. Other GD samples (GD-2, GD-3, GD-4, and GD-5) also displayed high *T* values ranging between 89%–95% (Fig. 4.4 (b-f)). Varying intensities around 2250 cm^{-1} were observed as a result of the broadening of the G′ band caused by the randomly stacked structure. Similar to the GC samples, this result concluded that most of the GD samples were constructed from the graphene layers with randomly stacking structures. Compared to that of the GC series samples, the GD ones showed an even higher *T* value. This indicates that NDs should be highly effective compared with CNFs when it comes to decreasing the stacking order of multilayer graphene. The *T* values of the GD samples did not differ largely when the ND concentration increased. The details of the stacking structure variations will be further discussed by combining the result of the XRD analysis in Section 4.4.2.

4.4 X-ray diffraction analysis of stacked graphene with spacers

4.4.1 X-ray diffraction analysis of stacked graphene with CNFs

Fig. 4.5 (a) shows the XRD patterns measured from the CNF-incorporated rGO sponges (GC series) and pure rGO sponge (G-0). The 002 peak derives from the periodicity of the graphene layer in the stacking direction. The 002 peak position indicates the layer distance of the samples, while the FWHM of the 002 peak corresponds to the crystalline size in the stacking direction. The 002 peak position of G-0 was at 26.2°, and its FWHM was 0.85°. These values were obtained by fitting the peak with a pseudo-Voigt function, which is commonly used for XRD analysis of

graphite [114]. This is because the broadening peak is composed of two major profiles: size broadening and strain broadening, which can be fitted using the Lorentzian and Gaussian functions, respectively [115, 116]. The pseudo-Voigt function is an appropriate candidate as it is a linear combination of Gaussian and Lorentzian functions [117]. The peak positions and the FWHM of the 002 peaks from the GC series samples ranged between 25.9°–26.0° and 1.52°–1.74°, respectively.

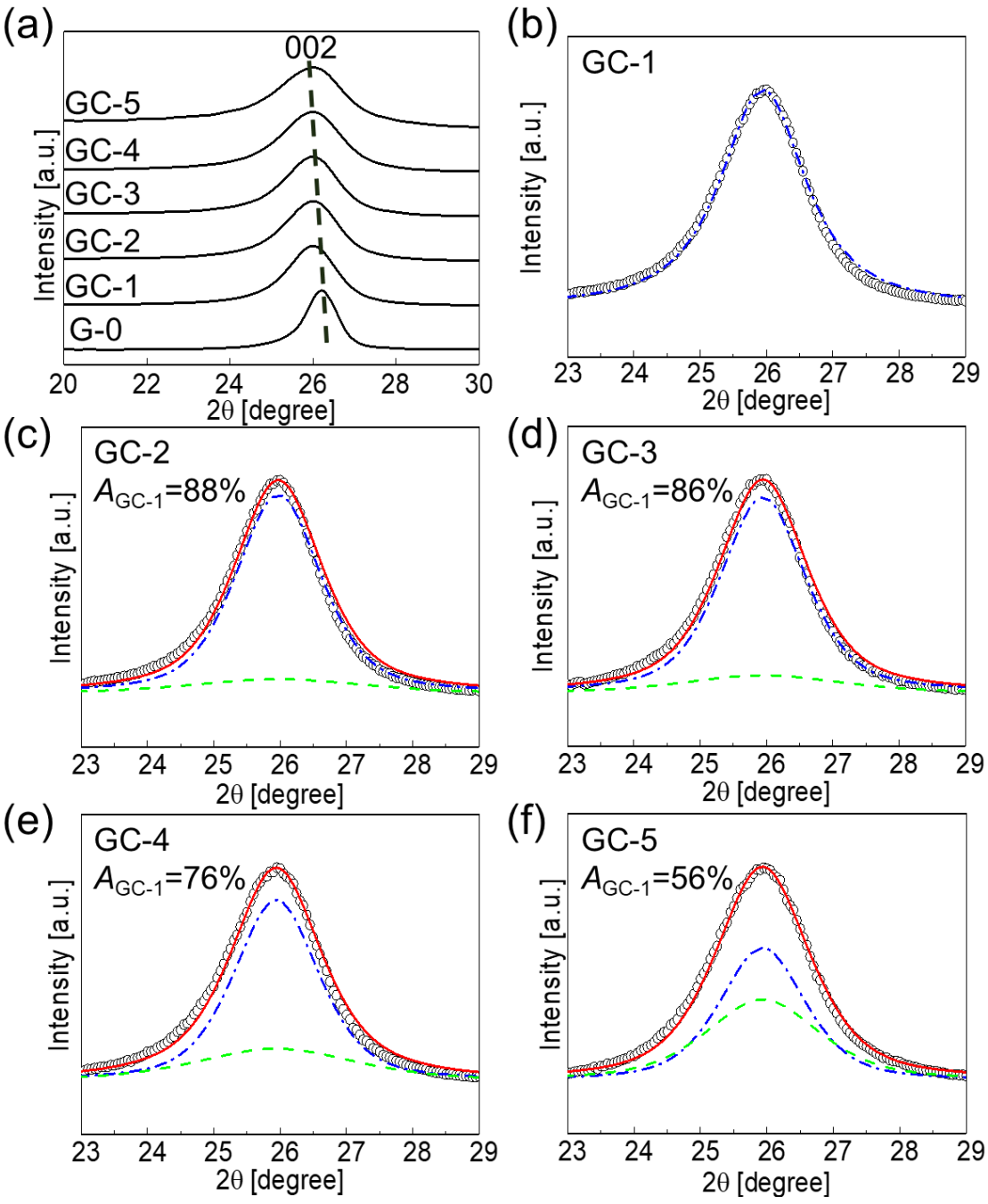

Figure 4.5 (a) XRD patterns of the GC series samples and G-0. The 002 peaks of graphene are

observed at ~ 26°. (b) Fitting of the GC-1 002 peaks. Black open circles denote the measured XRD patterns. Blue dashed-dotted curves denote the fitting curve with a single pseudo-Voigt function [114]. Deconvolution of the 002 peaks of (c) GC-2, (d) GC-3, (e) GC-4, and (f) GC-5 into two components. Black open circles denote the measured XRD patterns. Blue dashed-dotted curves denote the first components originating from the stacked structure of graphene possessing the same d_{002} and L_c as GC-1, while the green dashed curves denote the second components derived from the one possessing the same d_{002} as GC-1 but smaller L_c. Red solid curves are the sum of the blue and green ones. Ratios of the first component areas over the total peak area, $A_{GC\text{-}1}$, are displayed [75].

According to the formula (2.2), the d_{002} of G-0 was 0.340 nm, while that of GC-1, GC-2, GC-3, GC-4, and GC-5 ranged between 0.342–0.343 nm. Compared to G-0, GC samples showed larger layer distances in the stacking direction, indicating that the addition of CNFs enlarged the layer distance of stacked graphene. This slight increase indicates a decrease in the layer number of graphene; this is because the layer number and distance are directly correlated [118]. Note that d_{002} of bulk graphite is 0.335 nm, according to references [119, 120], while that of a typically stacked rGO is about 0.341 nm [121]. The details of the layer number will be discussed later.

The L_c, the crystalline size in the stacking direction, was analyzed from the 002 peak of XRD patterns of the GC series samples and G-0, as shown in Fig. 4.6 (a). The L_c values analyzed from XRD for G-0 and GC samples were 9.50 nm, and 4.63–5.29 nm, indicating the suitability of Scherrer's equation to these samples [87]. By adding CNFs as a spacer material, L_c decreased with the increase in CNF concentration. This was particularly clear in the comparison between G-0 and GC-1. Even when a little amount of CNF (actually, the smallest in this experiment) was added, the fraction of the random stacking structure significantly increased from 75% to about 85% (Fig. 4.1 (g)), whereas L_c rapidly decreased from 9.50 to 5.29 nm. This indicates that CNFs contribute to the crystalline size reduction due to their role as a spacer between layers. By dividing L_c by d_{002}, a characteristic layer number of stacked graphene, which is active for XRD measurement, can be obtained. The characteristic layer number of G-0 and GC-1 was calculated to be about 28 and 15 layers, respectively, indicating that the stacking of graphene layers is suppressed by the addition of CNFs.

It should be mentioned that the 002 peak fitting with only a single pseudo-Voigt function resulted in a relatively high residential error of 18–25% for GC-2 to GC-

5, while G-0 and GC-1 displayed a low error of 13% and 16%, respectively, as shown in Fig. 4.6 (c). The large errors indicate that the high CNF concentration samples have large structural variation and cannot be represented by a single component of periodically stacked graphene. Considering the drastic decrease of L_c with the small number of CNFs and its following gradual decrease with the increase in CNFs, it is expected that the spacer will first separate stacked graphene into thin components and then make them even thinner with the increase in CNF concentration. Thus, for simplicity of the analysis, this study assumes that stacked graphene can be mainly classified into two components based on thickness, namely the first and the second ones. The first component is regarded as the main component formed by adding a small number of CNFs, and the second component is formed by increasing the CNF fraction. We conducted the peak fitting of the 002 peak with two pseudo-Voigt functions, as described in detail later, and found that the residential error of GC-2 to GC-5 was significantly reduced to 9–13%, as shown in Fig. 4.6 (c). This confirms the effectiveness of the two peak deconvolution and the validity of the assumption.

Since all GC series samples showed 002 peak at similar 2θ angles, this study considered that the first and second components of each sample maintained the same layer distance. Thus, both the 2θ angle of the first and second component were fixed to their original values obtained by the single component fitting. The FWHM of the first component was fixed to that of GC-1 such that its L_c was identical to that of GC-1. To evaluate the relative abundance of the first component, $A_{GC\text{-}1}$ was obtained by taking the ratio of its area over the total peak area.

This analysis was applied to the XRD patterns of the GC series samples, except for GC-1. The fitting results are shown in Fig. 3(c-f). $A_{GC\text{-}1}$ decreased from 88% to 56%, for GC-2 and GC-5, respectively. The change in L_c of the second component and $A_{GC\text{-}1}$ are shown in Fig. 4.6 (a) and (b), respectively. This tendency indicates that by increasing the CNF concentration, the formation of the first component was restrained, while that of the second was enhanced. It should be noticed that Raman signals reflect whole portions of samples, and the analysis of G′-band indicates that the fraction of randomly stacking graphene is almost constant for the samples with the addition of the spacer, as shown in Fig. 4.2 (f) and Fig. 4.4 (f). This result should allow us to assume that both of the first and the second components possess the same fraction of the randomly stacking graphene.

Based on the XRD fitting results, it can be inferred that the stacking process of graphene with the addition of CNFs can be regarded as a two-step process. In the first one, the GO aggregates to the first component size, and the low concentration of CNF restrained the further aggregation between the first components, leading to a decreased L_c of GC-1, which is about half of that of G-0. As a result, the accessible region for the ethanol-derived species, where the formation of AB-stacking is suppressed, is increased, explaining why the T value of GC-1 increases compared to that of G-0. If the spacer concentration is high, the second step will occur simultaneously. In this process, the spacer physically restrains the formation of the first component, especially in high CNF concentrations. The GO flakes are formed into the second component with fewer layers. Therefore, the CNF concentration strongly affects the second component fraction.

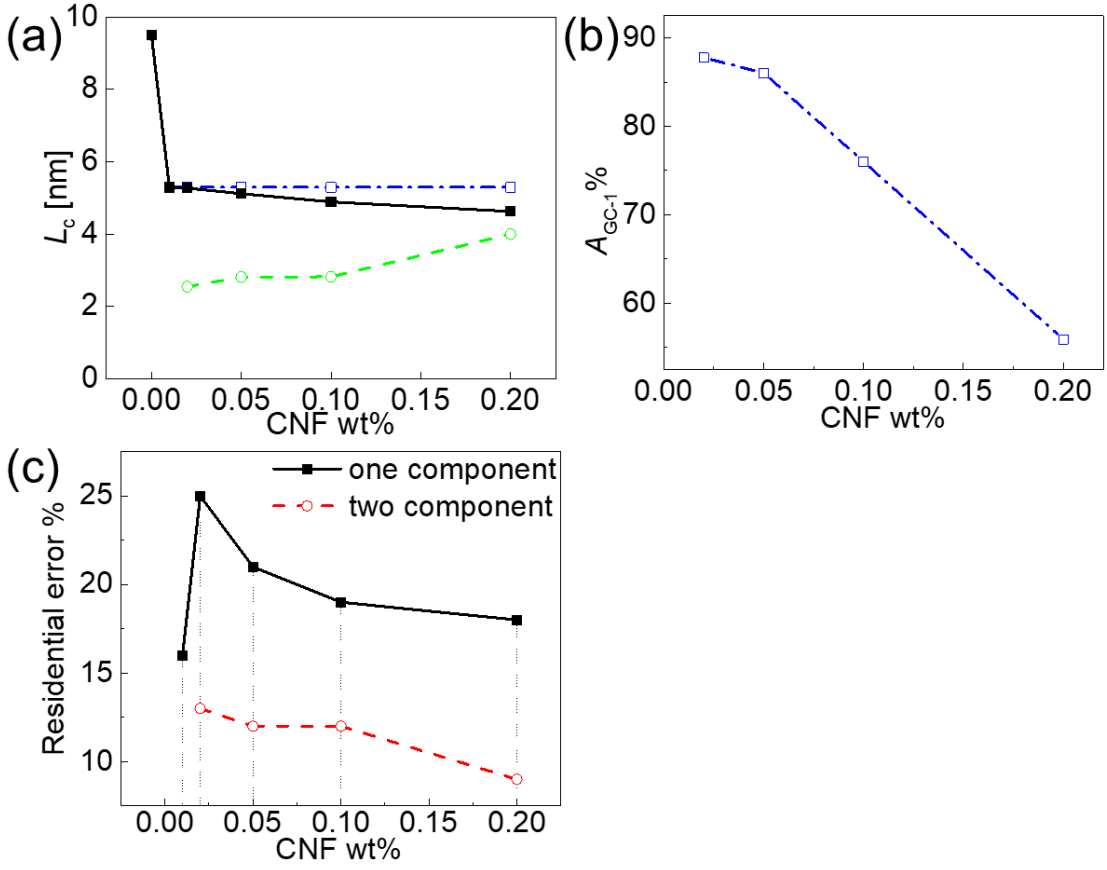

Figure 4.6 (a) L_c of different CNF concentration samples (Filled black square, G-0, and GC series samples). Blue open squares with dashed-dotted lines denote the L_c of the first components, while green open circles with dashed lines denote the second components. (b) A_{GC-1} plotted against the CNF weight percentage. (c) Residential error in XRD peak analysis of

samples with different spacer weight percentages of CNF. Black-filled squares with solid lines denote the residential error of one component fitting, while the red open circles with dash lines denote the residential error of two components fitting [75].

4.4.2 X-ray diffraction analysis of stacked graphene with NDs

The XRD patterns of the GD sponges and G-0 as the control group are shown in Fig. 4.7 (a). The 002 peak positions of the GD sponges ranged between 25.9°–26.0°. The FWHM of the peaks ranged from 1.27° to 1.82°. During fitting, this study also found that the residential error of GD-2 to GD-5 could be reduced from 10–15% to 7–10% by using the two-peak fitting in a similar manner to the one used with the GC samples(Fig. 4.8 (c)).

Using Bragg's equation (2.2), the calculated d_{002} values of GD-1, GD-2, GD-3, GD-4, and GD-5 ranged between 0.342–0.344 nm. Compared to G-0, GD samples showed a larger layer distance in the stacking direction. The observed expansion of d_{002} implies that ND decreased the layer number since graphene with smaller layer numbers had a larger layer distance [118].

By adding NDs as a spacer material, L_c decreased with the increase in ND concentration (Fig. 4.8(a)). The L_c [87] of the GD samples ranged 4.43–6.31 nm. This was particularly manifest in the comparison between G-0 and GD-1. When the smallest amount of NDs was added, the fraction of the random stacking structure increased significantly from 75% to around 95% (Fig. 4.4 (f)), whereas L_c rapidly fell from 9.50 to 6.31 nm. This indicates that NDs contribute to the size reduction of ordered structures of stacked graphene, presumably due to their function as spacers between layers. By dividing L_c by d_{002}, the characteristic layer number of the GD samples was calculated to be around 18 layers.

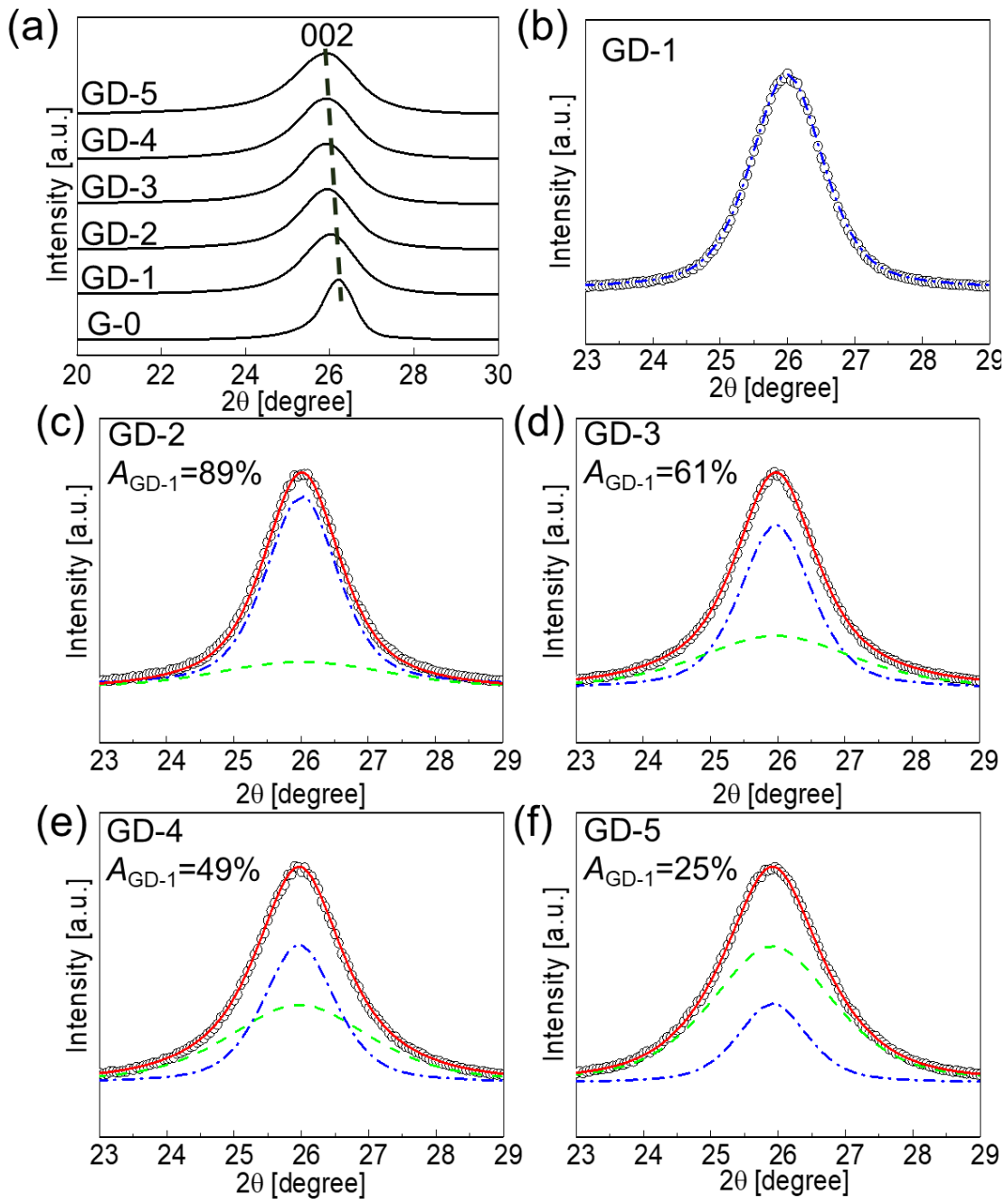

Figure 4.7. (a) XRD patterns of the GD series samples and G-0. The 002 peaks of graphene are observed at ~ 26°. (b) Fitting of the GD-1 002 peaks. Black open circles denote the measured XRD patterns. Blue dashed-dotted curves denote the fitting curve with a single pseudo-Voigt function [114]. Deconvolution of the 002 peaks of (c) GD-2, (d) GD-3, (e) GD-4, and (f) GD-5 into two components. Black open circles denote the measured XRD patterns. Blue dashed-dotted curves denote the first components originating from the stacked structure of graphene possessing the same d_{002} and L_c as GD-1, while the green dashed curves denote the second components derived from the stacked structure of graphene possessing the same d_{002} as GD-1

but smaller L_c. Red solid curves are the sum of the blue and green ones. The ratios of the first component areas over the total peak area, $A_{GD\text{-}1,}$ are displayed [75].

The analysis method based on two components, distinguished by their thicknesses, was applied for the XRD patterns of the GD series samples, except for GD-1. After fitting, the area fraction of the first component, $A_{GD\text{-}1}$, was obtained using the ratio of the first component area to the total peak area. The fitting results are shown in Fig. 4.7 (c-f). The first component fraction, $A_{GD\text{-}1}$, decreased from 81% to 25%, for GD-2 and GD-5, respectively. The change in L_c of the second component and $A_{GC\text{-}1}$ are shown in Fig. 4.8 (a) and (b), respectively. This tendency indicates that by increasing the ND concentration, the formation of the first component was restrained, while the second component was enhanced.

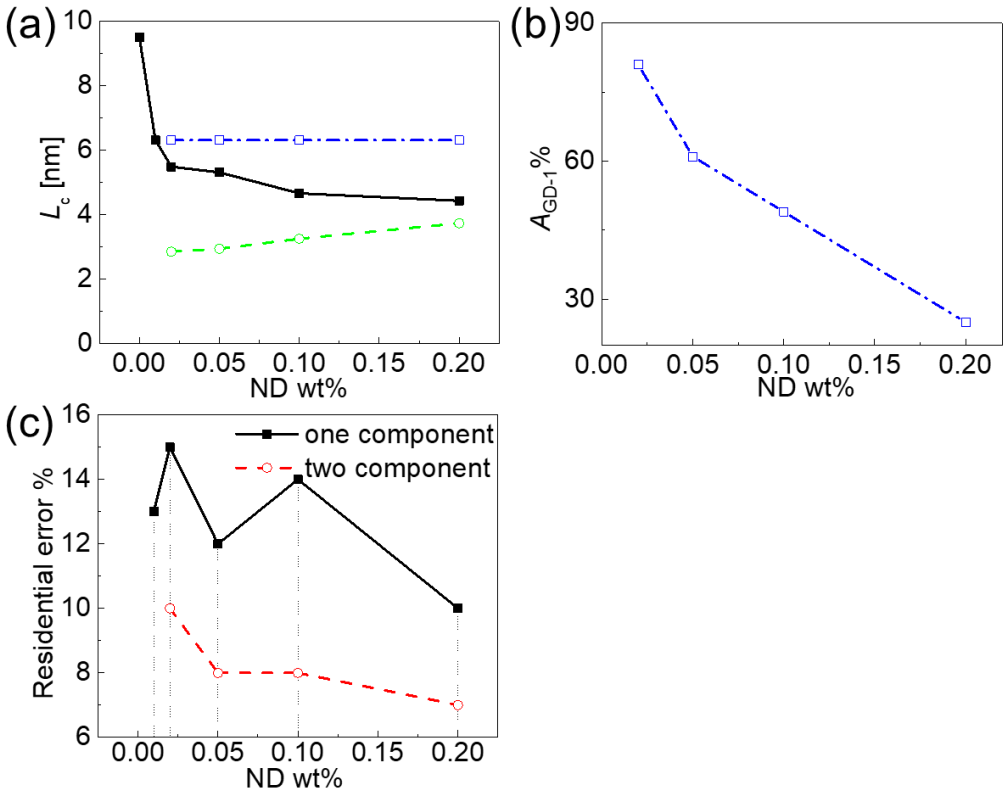

Figure 4.8 (a) L_c of different ND concentration samples (Filled black squares, G-0, and GD series samples). Blue open squares with dashed-dotted lines denote the L_c of the first components, while the green open circles with dashed lines denote the second components. (b) $A_{GD\text{-}1}$ plotted against the ND weight percentage. (c) Residential error in XRD peak analysis of

samples with different spacer weight percentages of ND. Black-filled squares with solid lines denote the residential error of one component fitting, while the red open circles with dash lines denote the residential error of two components fitting [75].

The fitting results of XRD indicate that the process of the stacking order change in the ND-incorporated samples can be understood similarly to the case of CNFs, which was described in Section 4.3. In addition, compared with GC samples, GD ones demonstrated a low $A_{GD\text{-}1}$, indicating that GD possessed a higher efficiency in restraining the formation of the first component. The reason for the decreased restraining efficiency of CNF will be discussed in the following section.

It should be mentioned that XRD and Raman spectroscopy provides information on different portion of samples. Since diffraction occurs only from periodic structures of samples, XRD can evaluate crystalline structures but cannot detect un-periodic structures, including amorphous structures and graphene separated by spacers. On the other hand, Raman signals reflect whole portions of samples in each measurement spot. Note that the smaller measurement area of Raman spectroscopy was compensated by the measurement at multiple spots. We characterized the random stacking ratio of whole samples by Raman spectroscopy and utilized XRD for the deep analysis of relatively thick periodic portions of samples, including AB-stacked graphene whose formation should be suppressed. This evaluation scheme is effective for investigating the stacking order of bulk-scale graphene. Selected area electron diffraction (SAED) provides direct information on the structure of turbostratic graphene, such as twist angle [122]. However, SAED is not capable of measuring our sample, a three-dimensional graphene sponge, since SAED can only be utilized for a thin sample. We would prepare a graphene thin film with twisted stacking and adequate thickness for SAED observation in future research.

4.5 Mechanism of stacking order change with nanospacers

By comparing G-0 with GC-1 and GD-1, this study found that L_c decreased to almost half after adding spacers. To find out in which process the change in stacking happened, XRD measurements of the sponge samples were conducted before thermal treatment (GO, GO/CNF, and GO/ND). Fig. 4.9 shows the XRD pattern observed from

the sponge prepared by freeze-drying the dispersions of the GO, GO/CNF, and GO/ND, in which the 002 peaks were located at 12.3°, 12.0°, and 11.1°, and their FWHM were evaluated to be 0.75°, 0.75°, and 0.63°. The 002 peaks from GO/CNF and GO/ND shifted to lower angles, compared to that of GO. These shifts should be caused by the difference in the pH values for the dispersions [123]. The pH values for the dispersions of GO, GO/CNF, and GO/ND measured before freeze-drying were 2.6, 2.9, and 3.5. The oxygen functional groups on the GO flakes showed increased repulsion due to a negative charge with pH increasing [123], leading to the larger layer distance for a higher pH value. The d_{002} and L_c can be evaluated by applying Bragg's and Scherrer's equations, (2.2) and (2.3), with the observed FWHM and 002 peak angles. Obtained values of the d_{002} for GO, GO/CNF, and GO/ND were 0.72, 0.74, and 0.80 nm, and those of L_c [87] were 10.55, 10.62, and 12.45 nm. The d_{002} of the pre-thermal treatment samples were larger than that of the corresponding ones with thermal treatment due to the oxygen-containing groups in GO [124].

From d_{002} and L_c, the characteristic layer numbers of these samples were calculated as ~14, 15, and 16 layers, respectively. This indicates that the stacking number of GO layers before the thermal treatment does not significantly differ even after adding spacers. The layer number is comparable to that of the GC (~15) and GD (~18) series samples but is about half of that of G-0 (~28). Thus, it can be inferred that in the case without spacers, the layer number of stacked graphene increased during the thermal treatment, probably due to the merge of the stacked GO units originally separated by void gaps. In contrast, the layer number was preserved during the thermal process in the case of the spacer addition. This represents the role of the spacers in suppressing the graphene stacking during the thermal treatment by physically separating the stacked GO units.

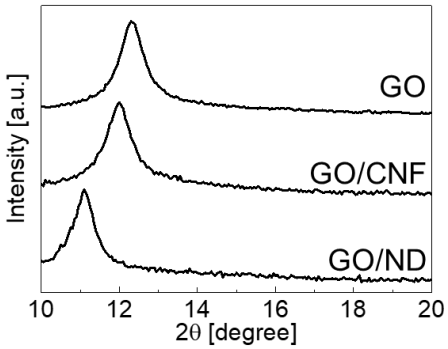

Figure 4.9 XRD patterns of GO, GO/CNF, and GO/ND [75].

SEM images of the GC-5, GC-3, GC-1, G-0, GD-5, GD-3, and GD-1showed porous structures of graphene sponges (Fig. 4.10 and Fig. 4.11), confirming that freeze-drying successfully formed a high surface-area structure preserved even after the thermal treatments at high temperature. Particles of around 10 μm in size were observed on GC-5 and GC-3 (Fig. 4.10 (a-f)), while none were to be seen on GC-1, GD-5, GD-3, GD-1, and G-0 (Fig. 4.10 (g-l) and Fig. 4.11 (a-i)). This indicates that part of the CNF was aggregated into the particles in high concentration, obstructing it from playing a spacer role in the GO composite. Thus, the CNF results in less contribution to the stacking order reduction in the following process at high concentration. On the other hand, no ND aggregate was observed, indicating that ND continued to work as a spacer even in high concentrations.

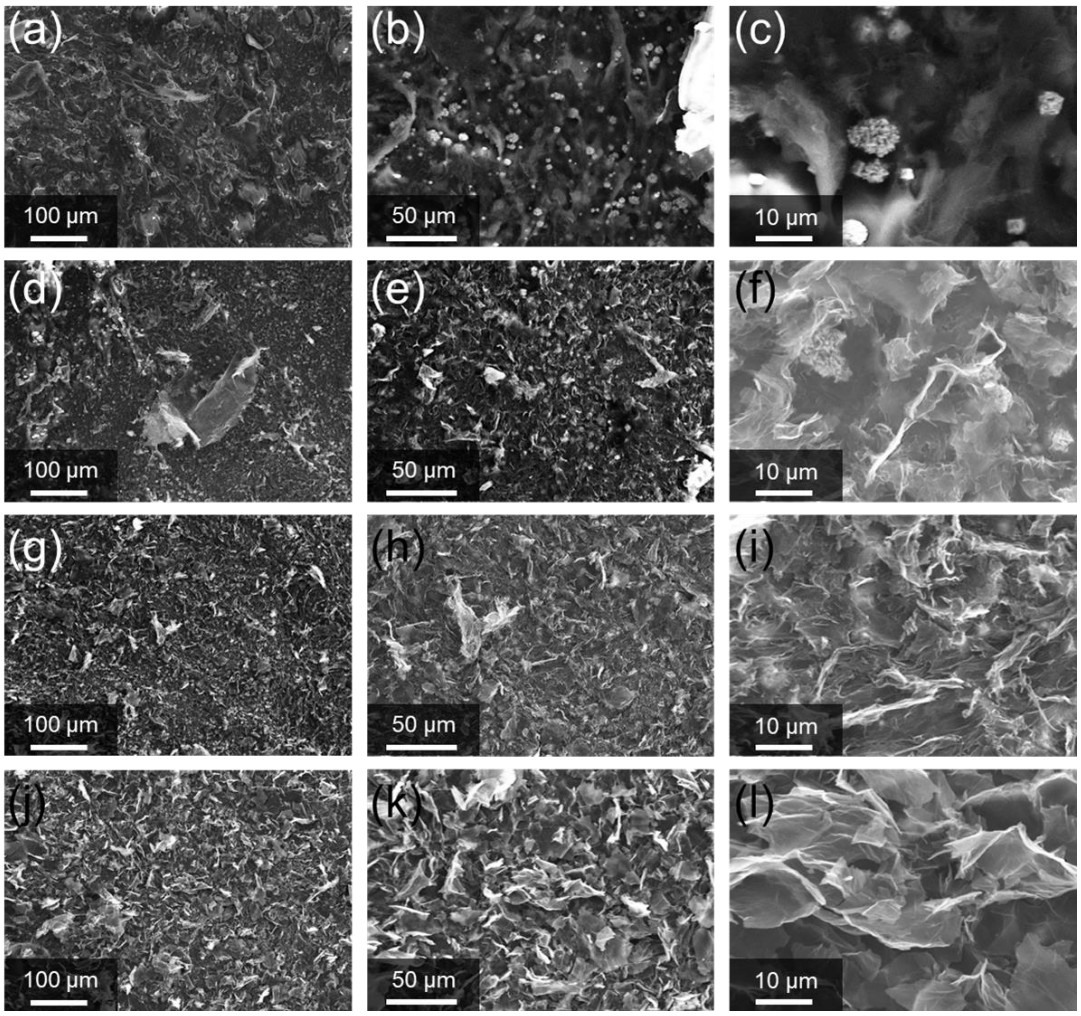

Figure 4.10 SEM images of (a-c) GC-5, (d-f) GC-3, (g-i) GC-1, and (j-l) G-0 with different magnifications [75].

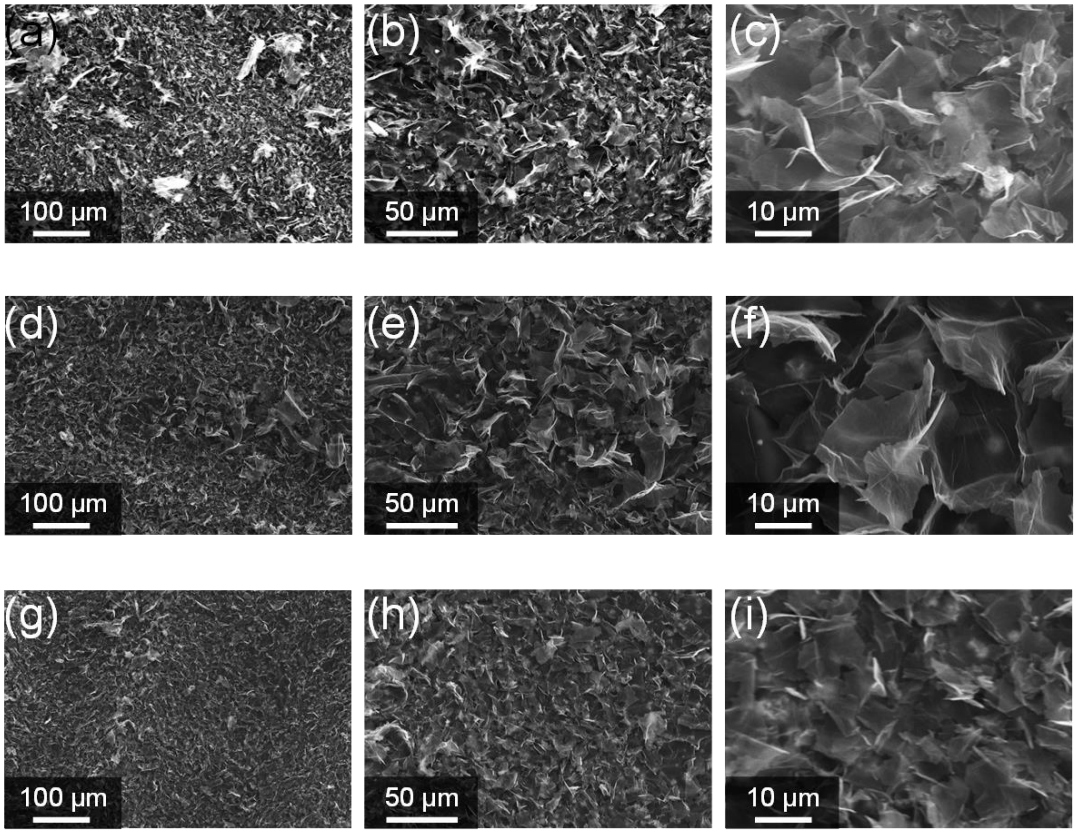

Figure 4.11 SEM images of (a-c) GD-5, (d-f) GD-3, and (g-i) GD-1 with different magnifications [75].

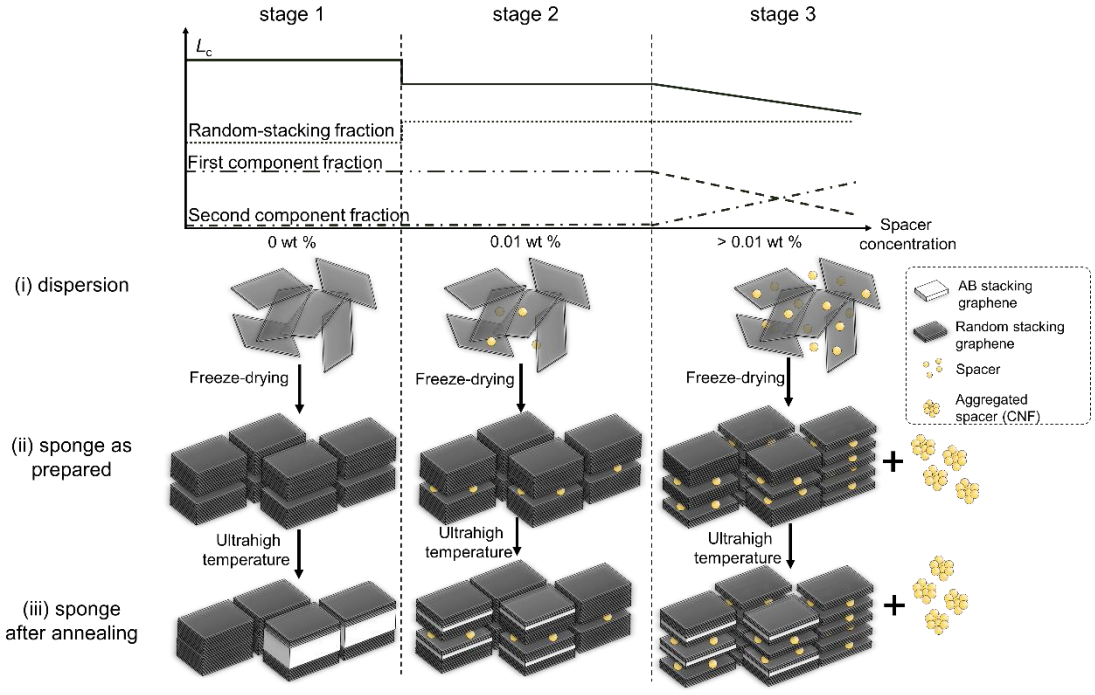

Figure 4.12 Schematic image showing the nanospacer effect. The trends in L_c, random-stacking

fraction *T*, and the first and the second component fractions versus the spacer concentration are indicated at the top of the panel. The solid curve donates the L_c. The dotted curve donates the random-stacking fraction. The dash-dot-dotted curve and dash-dotted curve donate the first- and second component fractions, respectively. The mechanism diagram is located below the curve graph. It is divided into three stages from left to right: a graphene sponge without spacers, one with a 0.01 wt% spacer concentration, and one with a higher spacer concentration, respectively. Each stage is further divided into three steps of the sample preparation process from top to bottom: (i) dispersion after mixing, (ii) the GO sponge after freeze-drying, and (iii) the rGO sponge after the thermal treatment, respectively. For high spacer concentrations, the CNF was aggregated, whereas the ND was not largely aggregated [75].

Based on the results and the above discussion, this study summarized the stacking order reduction mechanism in multilayer graphene by inserting nanospacers in Fig. 4.12. The change in stacking order is divided into three stages and three steps depending on the concentration of spacers and the process. In the first stage (Fig. 4.12, left), without adding any spaces at step (i), the pure graphene sponge showed a large L_c of 9.50 nm and a relatively low *T* value of 75%. This was due to the further stacking of the GO flakes, having about 15 layers at step (ii) that compose the GO sponge, into the rGO, having about 28 layers, during the ultrahigh temperature process at step (iii). Thus, the formation of AB stacking cannot be prevented in the internal region of thick graphene, where ethanol-derived species [5, 54] cannot access, resulting in a relatively low *T* value. In the second stage (Fig. 4.12, middle), a small amount of ND and CNF was added as a spacer at step (i). L_c was reduced to 5.29 and 6.31 nm for CNF and ND, respectively. This was because the added spacers prevented the stacking increase during the thermal process of step (iii) and produced the first component, which is thinner than the ones without spacers. This is also supported by the preservation of the characteristic layer numbers before and after the thermal treatment for the spacer-inserted samples. Due to the very thin layer (~15) of the first components, the ethanol-derived species can access the surfaces of each graphene flake, resulting in the formation of random-stacking graphene. Actually, according to the G′-band analysis on the Raman spectra, the *T* value increased to 85% and 89% for CNF and ND, respectively. In the third stage (Fig. 4.12, right), with the increase in spacer concentration at step (i), the *T* value did not vary from that of the second stage and remained almost constant. However, L_c gradually decreased at step (iii). The two-component analysis of XRD indicated that the formation of the first component was restrained, while the second one began to form.

The second component fraction was increased, resulting in the decrease of L_c. X. He, et al. repaired the graphene layer structure with 6-nm-thickness by CH_4 in graphene foam, and K. Kanishka, et al. proved that after ethanol-assisted thermo-treatment, the turbostratic stacking fraction of rGO on substrates reduced to about 80% when the thickness increased to 3.5 nm [125, 126]. Therefore, the accessible length for the substrate-free sponges is approximately 6 nm. Accordingly, the T value for the GC and GD samples did not change significantly, because the whole part of these samples, in which the thickness of the first and second components is not more than 6 nm, is within the accessible region for the ethanol-derived species.

4.6 Conclusion

The bulk-scale multilayer graphene sponge with ND or CNF spacers was obtained by freeze-drying and an ethanol-associated thermal treatment. Raman spectroscopy indicated a sudden increase in the random-stacking fraction by the addition of the spacers. According to the XRD analysis, the composite GO/spacer sponges before the thermal treatment possessed characteristic layer numbers comparable to those of the composite rGO/spacer sponges after the treatment, while the layer number of the pure rGO sponge was twice as large as that of the pure GO sponge. As a result, the accessible region for the ethanol-derived species of multilayer graphene increased after adding the spacers. Consequently, the random stacking fraction increased compared to the pure rGO sponge. The two-component analysis of XRD revealed that the graphene component with a smaller crystalline size was increased with increasing the spacer concentration, indicating that spacers can restrain the formation of the relatively thick component. Compared to the CNF-incorporated samples, the ND-incorporated ones showed a lower fraction of the thick component, indicating the effectiveness of ND as a spacer. Some particles were observed in the SEM image of the sample with a high CNF concentration, indicating that CNFs agglomerated in a high concentration and were unable to act as a spacer. The results proved that inserting nanospacers, especially NDs with high concentrations, can effectively reduce the stacking order in multilayer graphene. The controlled formation of 2D/1D and 2D/0D mixed-dimensional heterostructures is expected to preserve the superior properties of monolayer graphene in bulk scale, such as electric conductivity and flexibility, in bulk scale. These practically-available properties will pave the way for macroscopic

applications, for example, electrode materials in battery [15, 16] and supercapacitor [17, 18], and piezoresistive sensor [13, 14] for wearable devices.

Chapter 5: Performance enhancement of strain sensor using graphene with nanospacer insertion

5.1 Background

Strain sensors are devices aiming to convert changes in length into resistance signals [127], which are being explored in various potential applications, such as automated logistics transportation [128], autonomous driving [129], and human motion monitoring [130, 131]. The conventional strain sensors obtain resistance signals through a mechanism that involves resistance increase achieved by reducing the cross-sectional area of the internal metal wire when stretching. However, this mechanism results in low sensitivity and insufficient operating range [132-134], making them incapable of meeting the demands of the applications in the future. Researchers have studied nanomaterials as strain sensor material [135], including graphene [136-138], carbon black particles [139, 140], metal nanostructures [141, 142], and polymer nanofibers [143]. Unlike the metal wire with low stretchability in conventional stain sensors, nanomaterials offer high stretchability [144, 145] since they exist as individual components which can be easily separated, addressing the issue of a narrow operating range. Notably, graphene-based material [136-138] was supposed to be an ideal candidate for strain sensors due to the excellent properties of monolayer graphene, such as mechanical strength, surface area, and electric conductivity [6].

However, the recently reported graphene-based strain sensors suffer from some issues, including low linearity [146, 147], large hysteresis [148], and high initial resistance [149, 150], which restrict their practical application [151]. These issues arise due to the requirement of bulk-scale graphene in the fabrication of strain sensors. Typically bulk-scale graphene is produced through the reduction of graphene oxide (GO), where reducing chemical agents or hydrothermal treatment in an autoclave was employed. The graphene fabrication by chemical reduction of GO introduces the inevitable problems of the high defect density and functional group remaining on the prepared reduced GO (rGO)[45], which can result in the mentioned issues. The low linearity, the most serious issue, should be attributed to the remaining functional groups [147, 151], because they provide undesirable cross-linking between rGO flakes [152]. The sensor response is evaluated by variation of electrical resistance for rGO samples and is dominated by the contact area between the rGO flakes in the sensor device. The

cross-linking should cause non-linear deformation of rGO flakes on the strain sensor operation, leading to poor linearity in the sensor response of the relation between the resistance and device length. The large hysteresis, the second serious issue, should be due to the low mechanical strength, originating from the high defect density in the rGO [4, 6]. The low mechanical strength of rGO flakes leads to inefficient stress transmission on rGO flakes [132, 153]. This deviation from elastic deformation causes fluctuations in the contact area between rGO flakes during strain sensor operation. Accordingly, the resistance incompletely responds to deformation, and larger hysteresis should be observed from strain sensors with rGO with low crystallinity. The high initial resistance, the third serious issue, is also caused by the high defect density of rGO [154, 155], which is the resistance of strain sensor without deformation. Therefore, a higher applied voltage is required for strain sensing, as strain sensors are typically read by measuring the current at a constant voltage. Accordingly, the issues of low linearity, large hysteresis, and high initial resistance can be solved by utilizing highly crystalline rGO with low defect density and a reduced number of functional groups. Bulk-scale rGO with high crystallinity can be obtained through our previous study [5, 75], including freeze-drying and ethanol-associated ultra-high temperature process. Additionally, the random-stacking structure of rGO can also be achieved and is expected to exhibit high conductivity due to reduced interaction between rGO layers compared with AB-stacked graphene [55, 109]. It has been proved that the randomly stacked structure of rGO can achieve excellent properties similar to those of monolayer graphene, surpassing those of the AB-stacked structure [55, 109].

Moreover, we propose a novel strategy to further enhance the sensitivity. Compared to conventional metal-based strain sensors, rGO exists as individual flakes in graphene-based strain sensors, which can effectively separate by stretching operation. To further reduce the interaction between rGO flakes and enhance the sensor sensitivity, nano-diamonds (NDs) were added as a nanospacer between rGO flakes to physically prevent stacking and effectively separate the rGO flakes during the sensor operation. The ND is made up of an inner layer of a cubic diamond crystal (sp^3-hybridization) and a surface layer of oxygen-containing groups [73, 74]. Notably, while graphene is a two-dimensional (2D) material, ND is a zero-dimension (0D) material. The ND is transformed into carbon nano-onion (CNO) [76] by thermal treatment at more than 1000 °C, which can facilitate the separation of rGO flakes [156, 157]. It should be noted that the CNO can form a conductive path for current in sensor devices since it is composed of sp^2-hybridization and is highly conductive [158]. This combination of

graphene and the ND forms resilient 2D/0D mixed-dimensional heterostructures, effectively reducing the contact area between rGO flakes and yielding a higher resistance difference during sensor operation. Accordingly, the composite of rGO with ND as nanospacer was examined in this study for promising material to enhance the sensitivity of strain sensors.

In this study, to achieve low linearity, large hysteresis, and high initial resistance in graphene-based strain sensor, we used the freeze-drying and the ethanol-associated ultra-high temperature process to improve the crystallinity of rGO. Moreover, to ameliorate the sensitivity of the strain sensor, we investigated the effect of ND addition on reducing the interaction between rGO flakes. Also, we constructed a model to understand the unexpected trends of the resistance of strain sensors with increasing ND concentration. The strain sensor possessing high linearity, high sensitivity, and low initial resistance will pave the way for utilization, such as human motion detection and automated logistics transportation.

5.2 Experiment design

Fig. 5.1 shows the fabrication process of strain sensors from rGO. GO dispersion (1 wt%) was prepared using a modified Hummers' method [77]. The size of the GO flakes was measured to be approximately 10 μm by optical microscopy. The NDs were prepared using the detonation method, which had an average diameter of 5 nm by atomic force microscopy. The water dispersion of NDs with 1 wt% was applied as received from Nippon Kayaku Co. The sponges of GO and GO/ND were prepared by blending and freeze-drying as stated in our former research [75].

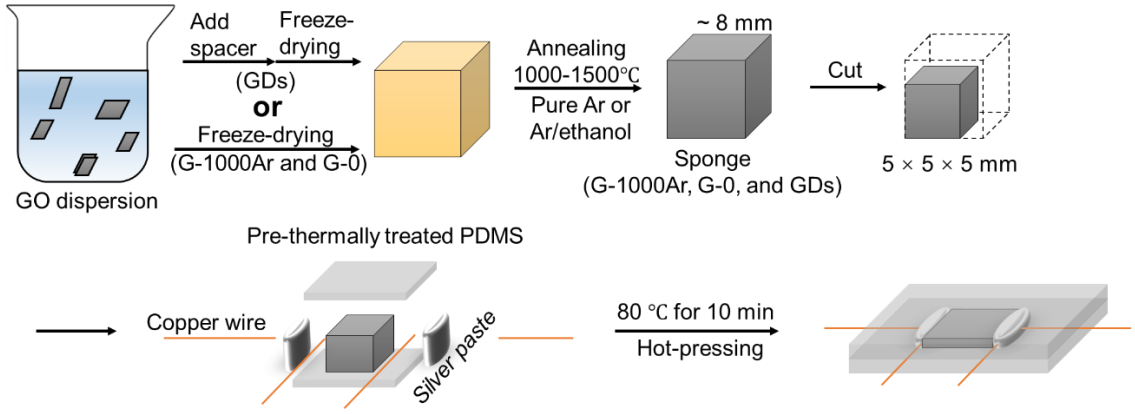

Figure 5.1 Process of rGO strain sensor preparation.

The GO and composite sponges were reduced and repaired under ultra-high temperature conditions with pure Ar or ethanol/Ar [5, 75]. We used a tubular electric furnace (HT1500-50-32P, HEAT TECH Co.) to conduct the ultra-high temperature process at 1000 °C or 1500 °C, with a vacuum pump keeping the chamber at low pressure. The rGO sample was prepared from GO sponge without ND under the condition of pure Ar at 1000 °C and with ethanol/Ar at 1500 °C, named as G-1000Ar and G-0, respectively. The GO/ND sponge samples were treated at 1500 °C with ethanol/Ar, and are named as GD-1, GD-2, GD-3, GD-4, and GD-5 according to the concentration of mixed ND for 0.01 wt%, 0.02 wt%, 0.05 wt%, 0.1 wt%, and 0.2 wt%, respectively. The series of the samples is also called GDs.

To prepare a strain sensor, the obtained G-1000Ar, G-0, and GDs sponges were cut into 5 mm ×5 mm ×5 mm cubes. The dimethylsiloxane was mixed with the initiator. This mixture was poured into the mold and heated at 80 °C for 7 min, and the partially polymerized polydimethylsiloxane (PDMS) film was obtained with about 35 mm ×25 mm ×2 mm. The cut sponge(G-1000Ar, G-0, or GDs), silver paste, and copper wire were placed on the PDMS film, and covered with another PDMS film, as shown in Fig. 5.1. By applying pressure and further heat treatment (66 kPa and 80 °C for 10 min), strain sensors were obtained to be ready for the operation.

Raman spectra were obtained by LabRAM HR-800 UV (Horiba Jobin Yvon) with a 532 nm wavelength for the excitation laser, 1 mW power, and ~0.7 μm of spot size. All the Raman results are obtained by averaging the data measured from 20 random spots. The sensor performance was tested with a lab-made measuring device, as shown in Fig. 2.14 (a). The device consisted of two parts: the sensor operation part

and the resistance measurement part. The sensor operation part consisted mainly of a stepping motor and its control unit, while the resistance measurement part was implemented by a DC voltage-current source/monitor (ADC 6241A). The contact resistance was evaluated by comparing the initial resistance of GDs obtained using both the two-wire and four-wire methods, as well as the comparison of sensor performance of G-0 evaluated separately using both methods, as shown in Fig. 2.14 (b) and (c). It should be noted that the two-wire method was exclusively used for this evaluation, whereas the four-wire method was employed for all other samples to ensure accurate measurements by minimizing the influence of contact resistance between the wires and the strain sensor. Measured parameters to evaluate the sensor performance are denoted as follows. L_0 and R_0 are the initial length and resistance of a sponge sample without deformation, and ΔL and ΔR are the difference of the length and the resistance between initial and operating conditions, respectively. $\Delta L/L_0$ and $\Delta R/R_0$ are the relative variation of length and resistance and were utilized for the evaluation of the sensor performance. Before the stretching process, R_0 was measured. In the stretching process, the sample was stretched up to 40% of $\Delta L/L_0$. The stretching process had five steps. Each step consists of 8% stretching in length ($\Delta L/L_0$), pausing for 2 s to stabilize possible delay of the deformation, and measurement of the resistance for strain sensing. After five steps of the stretching processes were completed, the sensor was operated to reverse direction for releasing the strain with the same step interval as the stretching process. The resistance at each step in the releasing process was measured and compared with the resistance for the stretching process to evaluate the hysteresis in the sensor operation. Thus, ΔR of each step can be obtained, and the ΔR_{max} was measured at the maximum of the $\Delta L/L_0$ (40%). The stretching and releasing processes were repeated ten times to obtain the averaged $\Delta R/R_0$. In this study, the sensitivity of the strain sensor is evaluated by GF, which is defined as GF = $(\Delta R/R_0)/(\Delta L/L_0)$. The linearity is obtained by the adjusted coefficient of determination of the linear regression of GF. The adjusted coefficient of determination is a statistical metric used to evaluate the accuracy of a model. In the strain sensor operation, the proportional relationship between $\Delta R/R_0$ and $\Delta L/L_0$ indicates the sensor response with high linearity, which corresponds to improved accuracy of the measured value.

5.3 Result and discussion

5.3.1 Sensor performance impacted by the crystallinity of reduced graphene oxide

To confirm the impact of rGO crystallinity on sensor performance, rGO samples of G-1000Ar and G-0 prepared by the thermal process at 1000 °C and 1500 °C were examined. No spacer material was incorporated in these samples for simplicity. The Raman spectra of G-0[75] and G-1000Ar had been measured for the evaluation of crystallinity, as indicated in Fig. 5.2 (a). The intensity ratio of the D-band to the G-band I(D)/I(G) corresponded to the defect density in graphene [97]. Fig. 5.2 (b) and (c) showed the observed sensor response from these samples, and the R_0 and the analyzed GF were plotted in Fig. 5.2 (d).

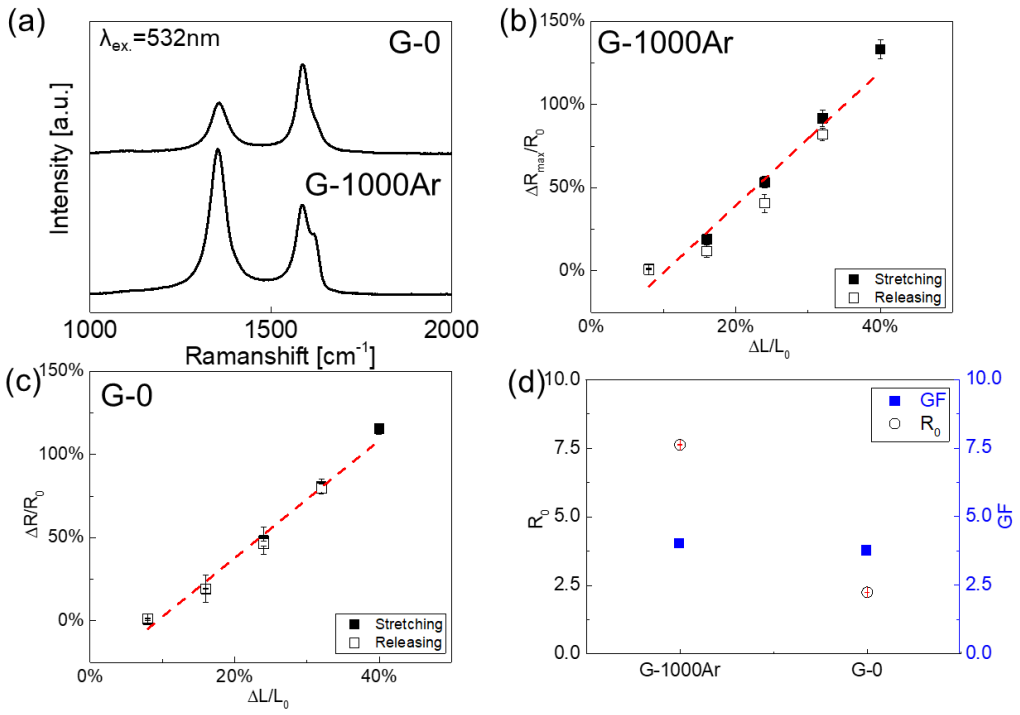

Figure 5.2 (a) Raman spectra of G-1000Ar and G-0. Sensor operation of (b) G-1000Ar and (c) G-0 during the sensor operation process. (d) R0 and GF of G-1000Ar and G-0.

Much lower I(D)/I(G) was observed from G-0 compared with G-1000Ar, indicating a lower defect density of G-0, where stronger mechanical strength should be expected due to high crystallinity. The D′-band observed at 1620 cm^{-1} for G-1000Ar

also indicates a high defect density [159]. As for the linearity of the sensor response, both G-0 and G-1000Ar were observed to exhibit higher linearity compared with the previous reports [148]. This response preferable for sensor operation might be originated from the thermal process at high temperature, which causes the improved crystallinity and the removal of the functional groups, resulting in the reduction of cross-linking between rGO layers. Relatively small hysteresis was observed from both G-1000Ar and G-0, as seen in Fig. 5.2 (b) and (c). A closer inspection of the differences revealed that G-1000Ar showed slightly larger hysteresis than that of G-0. This might be due to the decreased mechanical strength [4, 6] caused by the lower crystallinity for G-1000Ar, which shows higher I(D)/I(G) in the Raman spectrum. The rGO flakes with higher defect density could not perfectly follow the strain during the sensor operation because of the unstable connection of rGO layers. Hence, slight hysteresis of the resistance was observed from G-1000Ar. On the other hand, G-0 exhibited higher crystallinity due to the ethanol-associated ultra-high temperature process and is expected to provide higher mechanical strength. Accordingly, the rGO flakes with lower defect density could be deformed elastically, and the connection of the rGO flake should be stable and similar for the stretching and releasing operation of the sensor. Hence, smaller hysteresis of the resistance was observed from G-0. Higher crystallinity also affected the initial resistance R_0 significantly. As shown in Fig. 5.2 (d), R_0 decreased from 7.70 Ω for G-1000Ar to 2.25 Ω for G-0, indicating improved conductance of rGO with lower defect density. The sensitivity of the strain sensor was evaluated by GF, which was obtained by the analysis of $\Delta R/R_0$ and $\Delta L/L_0$. Contrary to expectation, as shown in Fig. 5.2 (d), the GF of G-0 was a similar value (~3.7) to that of G-1000Ar in spite of the large difference of their crystallinity and significant decrease of R_0 for G-0. This unexpected result might be caused by coordinated variation of ΔR and R_0, suggesting that the ΔR should be enlarged for achieving higher sensitivity.

As achieved for G-0, better linearity, smaller hysteresis, and lower R_0 will be expected for samples with higher crystallinity. Therefore, the condition of 1500 °C and Ar/ethanol gas was employed in the following study. In order to enhance ΔR during sensor operation and the sensitivity (GF), we attempted to improve the separation of rGO flakes by reducing their interaction with the addition of ND.

5.3.2 Sensor performances change with different ND concentrations

Composite of rGO and various concentrations of ND was fabricated in the sponge form and was used for sensor operation after structural analysis by Raman spectroscopy. The Raman spectra and their I(D)/I(G) analysis for G-0 and GDs samples were already reported in our former work [75] and were shown again as Fig 5.3 (a) and (b). The Raman result showed that the I(D)/I(G) ratios of the GDs samples ranged between 0.42–0.65, which were close to that of G-0 and lower than that of G-1000Ar. This means that the defect density of GDs and G-0 are quite comparable. The relationship between $\Delta R/R_0$ and $\Delta L/L_0$ evaluated during the sensor operation was indicated in Fig. 3 (c-g) for from GD-1 to GD-5, respectively. As indicated in Fig. 5.3 (h), the R_0 values from G-0 and GDs were almost constant and did not virtually depend on the ND concentration, ranging between 2.23–3.02 Ω. On the other hand, the ΔR_{max} increased from 2.75 to 7.37 Ω by adding a relatively lower concentration of ND (0.01–0.02 wt%), and then decreased to about 3.47 Ω by adding a relatively higher concentration of ND more than 0.02 wt%. The dependence of the linearity and GF on ND concentration were plotted in Fig. 5.3 (i), where high linearity ranging mostly between 0.92 to 0.98 was observed for G-0 and GDs. The hysteresis for $\Delta R/R_0$–$\Delta L/L_0$ relationship in stretching and releasing operation was negligibly small for GDs, indicating that structural deformation by the stretching and releasing process should be very stable. Unusual behavior of GF was observed for the increase of ND concentration. The GF suddenly increased from 3.8 (G-0) to 6.6 (GD-1) by adding a small amount of ND. The increase of GF, however, became maximum at 0.01 wt% of ND (GD-1), and the GF gradually decreased to 4.4 by adding a higher concentration of ND. As summarized in Fig. 5.3 (j), the sensor performance obtained from GD-1 surpassed that of the reported value in previous studies.

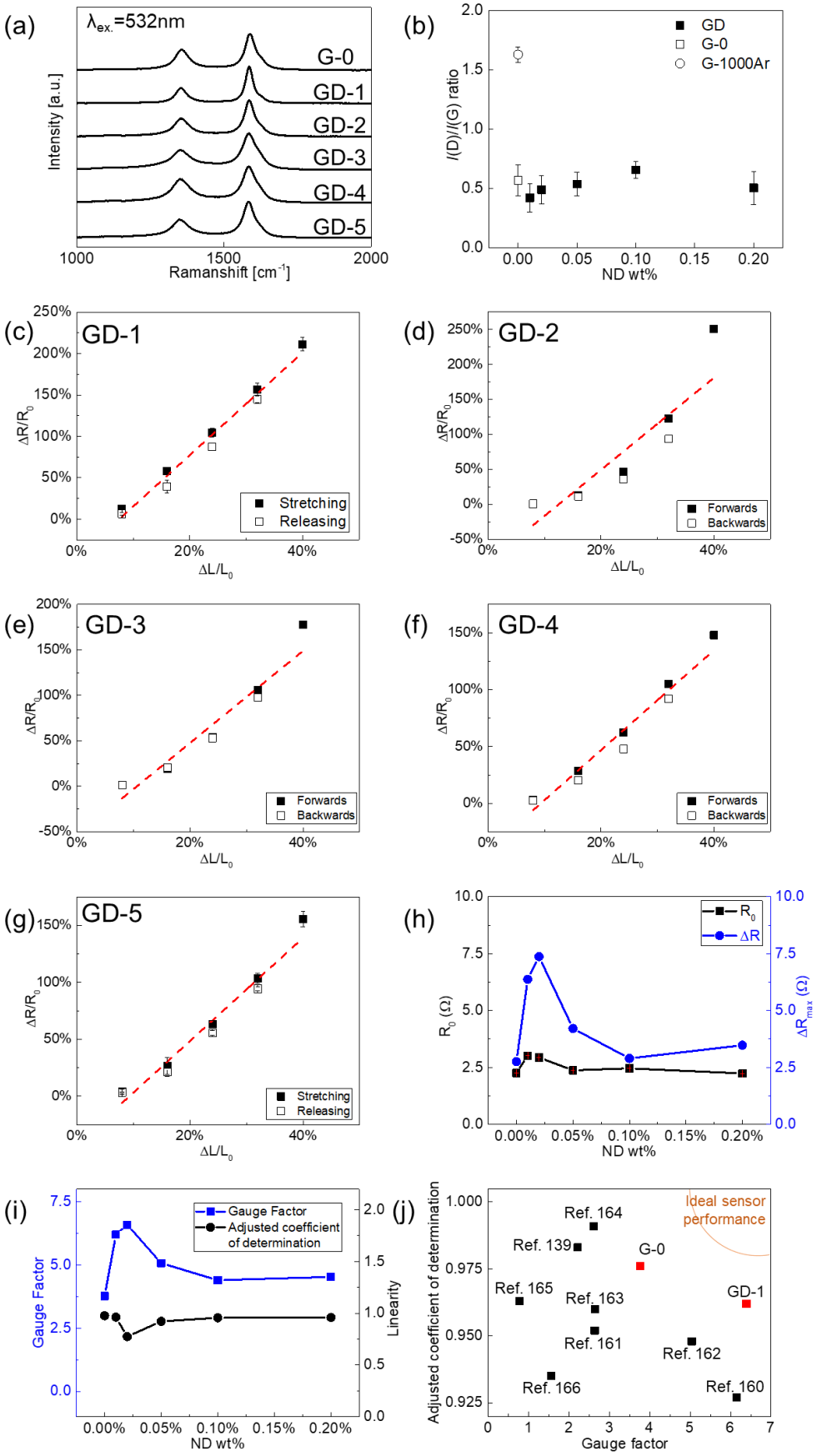

Figure 5.3 (a) Raman spectra of GDs and G-0. (b) *I*(D)/*I*(G) ratio of G-1000Ar, G-0, and GDs.

Sensor operation of (c) GD-1, (d) GD-2, (e) GD-3, (f) GD-4, and (g) GD-5 during the stretching and releasing process. (h) R_0 and ΔR against spacer concentration. (i) GF and linearity against spacer concentration. (j) Other previous studies of linearity and sensitivity on graphene-based strain sensors [139, 160-166].

5.3.3 Mechanism of sensor performances change

For the sensor performances with different ND concentrations, the R_0 showed similar values regardless of ND addition, while the ΔR_{max} first reached the peak after adding ND and subsequently decreased with increasing ND concentration (Fig. 5.3 (h)). To understand the trends of the R_0 and the ΔR_{max} observed in our experiment, we constructed a model that simplifies the structure of the rGO sponge. In this model, the resistance of the rGO sponge was considered as the combined resistance of identical unit components that were connected in series and parallel, as shown in Fig. 5.4 (a). We define a pair of multilayer rGO flakes as the unit component of G-0, as shown in Fig. 5.4 (b), and that of GDs will be explained later. This model was based on the assumptions that the sponge was homogenously composed of numerous rGO flakes and that the change in the resistance of the sponge at stretching was determined only by the change in contact resistance between rGO flakes, while the resistance of a single rGO flake remained constant. We employ the intrinsic resistance of a single rGO flake (R_i), the contact resistance between two rGO flakes at releasing (R_c), and the difference in the contact resistance at stretching (ΔR_c). The resistances of G-0 and GDs were denoted with suffixes, such as R_i(G-0) and R_i(GD). The R_i is determined by resistivity, cross-sectional area, and length of rGO flakes. As we assumed that the rGO flakes possessed the same resistivity and flake size, the R_i depends only on the rGO flake thickness. In our previous work,[75] the rGO flake thickness of G-0 is evaluated to be twice that of GDs (~10 nm and ~5 nm, respectively), suggesting that $2R_i(\text{G-0}) = R_i(\text{GD})$. Meanwhile, the R_c is determined by the contact area between two rGO flakes. The resistance of the unit component of G-0 at the initial state is $2R_i(\text{G-0})+R_c(\text{G-0})$ (Fig. 5.4 (b)). Because the total amount of rGO was the same for G-0 and GDs and the thickness was half for GDs, the number of rGO flakes in GDs was twice that of G-0. Thus, we defined two pairs of rGO flakes connected in parallel as the unit component of GDs, as shown in Fig. 5.4 (c), so that the numbers of unit components were the same for G-0 and GDs.

Accordingly, the resistance of the unit component of GDs at the initial state is expressed as $(2R_i(GD)+R_c(GD))/2$.

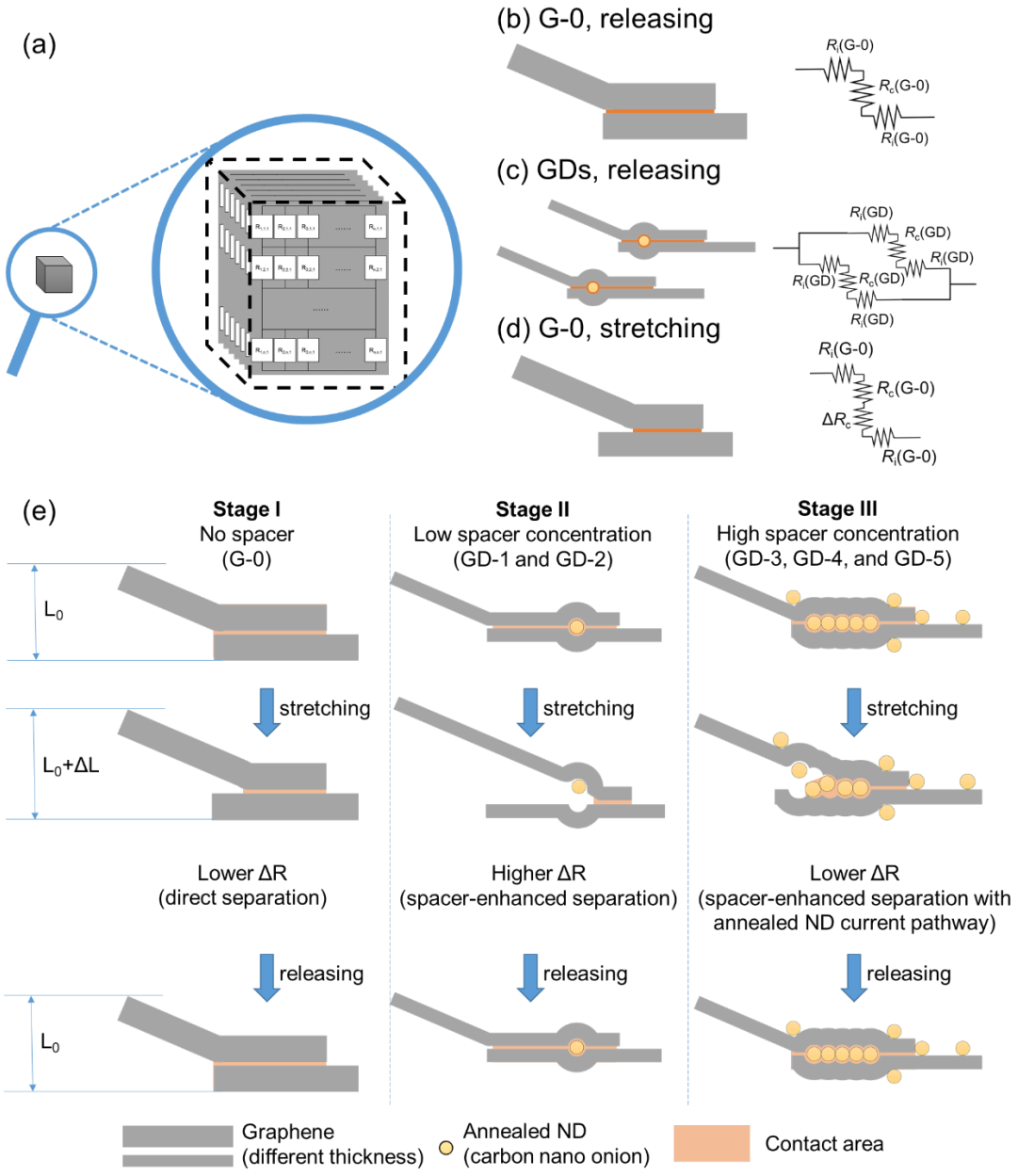

Figure 5.4 (a) Schematic image of the model in which the rGO sponge is composed of unit components. (b–d) Schematic images of unit components of (b) G-0 when releasing $(2R_i(G-0)+R_c)$, (c) GDs when releasing $(2R_i(GD)+R_c)$, and (d) G-0 when stretching $(2R_i(G-0)+R_c+\Delta R_c)$. (e) Schematic image showing the nanospacer effect in the strain sensor with increasing spacer concentration. There are three stages from left to right: a graphene sponge with no spacers, one with a lower spacer concentration, and one with a higher spacer concentration. The length of

the strain sensors during stretching and releasing, L_0 and $L_0+\Delta L$, respectively, were shown on the left side.

Based on the model, we explained the experimental result that the R_0 exhibited a similar value in G-0 and GDs. Because the rGO sponges, G-0 and GDs, were isotopically composed of the same number of each unit component, their resistances R_0 were proportional to the resistances of the corresponding unit components. From the definitions of the unit components and the relation of R_i(G-0) and R_i(GD) as discussed above, the resistances of the unit components of G-0 and GDs can be expressed as $2R_i$(G-0)+R_c(G-0) and $2R_i$(G-0)+R_c(GD)/2, respectively. Moreover, regarding R_c, our previous study [167] has revealed that the non-contact area and contact area of rGO flakes possess similar sheet resistance, which is consistent with other studies [168, 169]. This indicates that the R_c was much smaller than the R_i for the rGO flakes with high crystallinity and that the contribution of the R_c to the R_0 was negligibly small compared with that of the R_i. Consequently, the R_0 of both G-0 and GDs was approximated as $2R_i$(G-0), which can explain the comparable values of the R_0 for G-0 and GDs.

We then discussed the variation of ΔR_{max} with the ND concentration based on the model. The resistance of the unit component of G-0 at stretching is expressed as $2R_i$(G-0)+R_c(G-0)+ΔR_c(G-0), as shown in Fig. 5.4 (d). Considering the change from the released state to the stretched state, ΔR_{max}(G-0) was proportional to $\Delta R_{c(G-0)}$ at the highest strain (length was $L_0+\Delta L$). Similarly, ΔR_{max}(GD) was proportional to ΔR_c(GD)/2. Thus, the ΔR_c with different ND concentration should be considered for explaining the trend of ΔR_{max}. In our experiment, the ΔR_{max} firstly reached a peak at a low spacer concentration, and then it decreased with further increasing spacer concentration (Fig. 5.3 (h)). Thus, the variation of ΔR_{max} was divided into three stages depending on the ND concentration, as shown in Fig. 5.4 (e). In stage I, the ΔR_c of the pure rGO sample (G-0) indicated a certain positive value because of the decreased contact area for the separation of the rGO flakes during stretching. In stage II, by adding a small amount of ND (GD-1 and GD-2), much higher ΔR_c was obtained after stretching than that of stage I. The steeper decrease in the contact area of the rGO flakes in GDs, than that of G-0, was attributed to the annealed ND, which can facilitate the separation of rGO flakes [156, 157]. Thus, the sample of stage II achieved the highest ΔR_c and, accordingly, the highest ΔR_{max} because of the low contact area and the least conductive path of annealed ND compared to those of other samples. In stage III, the ΔR_c decreased

with further increasing the ND concentration. From the diameter of the annealed ND and the thickness of the rGO flakes, we calculated the occupation of the projected area of annealed ND on the rGO flake to be about 23% in GD-5, as shown in Appendix A. The high occupation of the projected area by annealed ND (CNO), which was electrically conductive, can provide additional conductive paths, even between separated rGO flakes during stretching. This brought about decreases in ΔR_c and then in ΔR_{max} in stage III. Consequently, the ΔR_{max} reached a peak at a low spacer concentration and decreased when the spacer concentration was further increased.

5.4 Conclusion

In this study, high linearity, small hysteresis, and low R_0 were achieved in the rGO strain sensor, by realizing the high crystallinity in the rGO sponge via ethanol-associated ultra-high temperature process. The R_0 decreased from 7.7 Ω to 2.25 Ω for the increase in the crystallinity. Then, the sensitivity of the strain sensor was further improved by the addition of ND, because the annealed ND can facilitate the separation of rGO flakes during stretching. After adding ND, the GF first increased from 3.7 (G-0) to 6.6 (GD-1), but it decreased to 4.4 (GD-5) for a further increase in ND concentration. The behavior of ΔR_{max} and R_0 of G-0 and GDs were understood by analyzing the R_i and the R_c under stretching or releasing based on the structural model. Accordingly, by increasing the crystallinity and adding a low concentration of ND, the strain sensor can achieve high linearity, small hysteresis, and low R_0, as well as improved GF, making it a promising candidate for future applications, such as human motion detection and automated logistics transportation.

Appendix A: The occupation of the projected area of annealed ND on the rGO flake

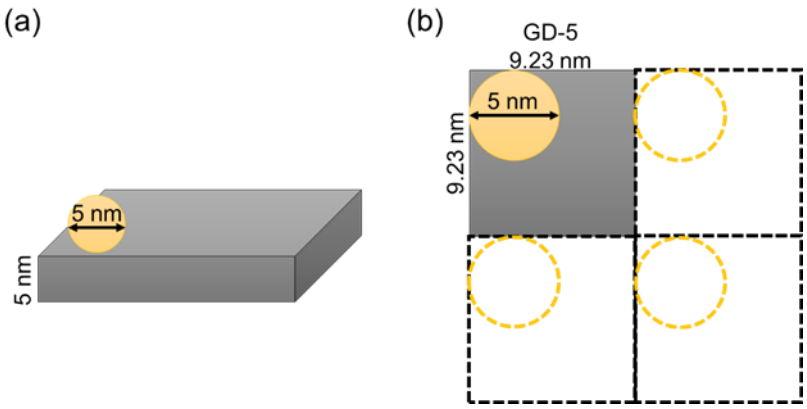

Figure 5.6 (a) The occupation of the projected area of annealed ND on the 5-nm-thickness rGO flake of GD-5. (b) The assumption of ND possessed a square lattice arrangement.

The GD-5 sample was prepared by incorporating 0.8 wt% of GO, 0.2 wt% ND, and 99% water. For a 1-cm^3 sponge, the mass of ND was 0.002 g, and the mass of GO was 0.008 g. Considering the respective densities of GO and ND, which are 0.00216 g/mm^3 and 0.00352 g/mm^3, the volumes of GO and ND (V(GO) and V(ND)) can be calculated as follows:

$$V(\text{GO}) = 0.008/0.00216 = 3.70\ \text{mm}^3 = 3.7 \times 10^{36}\ \text{nm}^3 \quad (5.1)$$

$$V(\text{ND}) = 0.002/0.00352 = 0.568\ \text{mm}^3 = 0.568 \times 10^{36}\ \text{nm}^3 \quad (5.2)$$

For a single ND particle with a diameter of 5 nm, which was observed by atomic force microscope, its volume (V(1-ND)) can be determined using the formula for the volume of a sphere:

$$V(\text{1-ND}) = 4/3 \times 3.14 \times 2.5^3 = 65.4\ \text{nm}^3 \quad (5.3)$$

By dividing the V(ND) by the V(1-ND), the number of ND particles (n(ND)) in the sample can be calculated:

$$n(\text{ND}) = 0.568 \times 10^{36}\ \text{nm}^3 / 65.4\ \text{nm}^3 = 8.69 \times 10^{33} \quad (5.4)$$

Next, the size of graphene, s(GO), with a thickness of 5 nm can be determined by dividing V(GO) by the thickness, as shown in Fig. 5.6 (a):

$$s(\mathrm{GO}) = 3.70 \times 10^{36}\ \mathrm{nm}^3 / 5\ \mathrm{nm} = 7.41 \times 10^{35}\ \mathrm{nm}^2 \quad (5.5)$$

To calculate the area of graphene that accommodates a single ND particle, A(ND), the s(GO) is divided by the n(ND):

$$A(\mathrm{ND}) = 7.41 \times 10^{35}\ \mathrm{nm}^2 / 8.69 \times 10^{33} = 85.3\ \mathrm{nm}^2 \quad (5.6)$$

Furthermore, assuming that the ND possessed a square lattice arrangement, the distance between two ND particles, d(ND), can be obtained by taking the square root of the A(ND), as shown in Fig. 5.6 (b):

$$d(\mathrm{ND}) = \sqrt{(85.3\ \mathrm{nm}^2)} = 9.23\ \mathrm{nm} \quad (5.7)$$

Similarly, the d(ND) and the occupation of the projected area of annealed ND on the rGO flake for GD-1, GD-2, GD-3, GD-4, and GD-5 can be obtained. The d(ND) was 41.3, 29.2, 18.5, 13.1, and 9.23 nm, while the occupation of the projected area of annealed ND was 1.2, 2.3, 5.7, 11.4, and 23.0% for GD-1, GD-2, GD-3, GD-4, and GD-5, respectively. Accordingly, the occupation of the projected area of annealed ND on the rGO flake was obtained.

Chapter 6 Conclusion

To fully utilize the high performance of graphene in macroscopic devices, it is necessary to form randomly stacked graphene instead of AB-stacked graphene in bulk scale. This is because the strong interlayer interaction of AB-stacked graphene can degrade the superior properties of monolayer graphene. However, conventional methods to obtain bulk-scale graphene suffer from a low crystallinity and/or the formation of a thermodynamically stable AB-stacked structure. To address this problem, the freeze-drying and ethanol-associated ultrahigh temperature processes were employed in this dissertation. Moreover, to further improve the randomly stacking fraction, CNF and ND played the nanospacer role in restraining the stacking during the ultrahigh temperature process. Lastly, the rGO and the rGO/ND sponge were employed as strain sensors to overcome the limitations of sensitivity (about 2) and strain test range (about 5%) of conventional sensors.

In chapter 3 of this dissertation, by freeze-drying of GO dispersion and an ethanol-associated reduction at ultrahigh temperature, a graphene sponge with a high random-stacking fraction for both surface and internal areas was realized. This feature is in sharp contrast to GO aggregate samples, where the formation of AB stacking cannot be suppressed in the internal area. The high random-stacking fraction in internal regions is attributed to the increased accessible area of the porous graphene sponge for ethanol-derived species. We optimized the reduction conditions and confirmed that the strong and sharp G′-band from graphene sponge is reduced at 1500 °C, which is indicative of a weak interlayer interaction. Additionally, CNF was introduced as a spacer into a GO sponge to separate the graphene layers and to avoid direct stacking. The blending of CNF with the GO dispersion further reduces the AB-stacked fraction. Although there is still room to improve mixing to achieve a higher $I(G')/I(G)$ ratio and homogeneity, the proposed scheme prevents strong interlayer stacking in bulk-scale graphene. Consequently, it should realize the scalable production of high-performance bulk-scale graphene in which the superior properties of single-layer graphene are effectively preserved.

Chapter 4 began with the bulk-scale multilayer graphene sponge with ND or CNF spacers prepared by freeze-drying and an ethanol-associated thermal treatment. Raman spectroscopy indicated a sudden increase in the random-stacking fraction by the addition of the spacers. According to the XRD analysis, the composite GO/spacer

sponges before the thermal treatment possessed characteristic layer numbers comparable to those of the composite rGO/spacer sponges after the treatment, while the layer number of the pure rGO sponge was twice as large as that of the pure GO sponge. As a result, the accessible region for the ethanol-derived species of multilayer graphene increased after adding the spacers. Consequently, the random stacking fraction increased compared to the pure rGO sponge. The two-component analysis of XRD revealed that the graphene component with a smaller crystalline size was increased with increasing the spacer concentration, indicating that spacers can restrain the formation of the relatively thick component. Compared to the CNF-incorporated samples, the ND-incorporated ones showed a lower fraction of the thick component, indicating the effectiveness of ND as a spacer. Some particles were observed in the SEM image of the sample with a high CNF concentration, indicating that CNFs agglomerated in a high concentration and were unable to act as a spacer. The results proved that inserting nanospacers, especially NDs with high concentrations, can effectively reduce the stacking order in multilayer graphene. The controlled formation of 2D/1D and 2D/0D mixed-dimensional heterostructures is expected to preserve the superior properties of monolayer graphene in bulk scale, such as electric conductivity and flexibility, in bulk scale.

In chapter 5, high linearity, small hysteresis, and low R_0 were achieved in the rGO strain sensor, by realizing the high crystallinity in the rGO sponge via the ethanol-associated ultra-high temperature process. The R_0 decreased from 7.7 Ω to 2.25 Ω for the increase in the crystallinity. Then, the sensitivity of the strain sensor was further improved by the addition of ND, because the annealed ND can facilitate the separation of rGO flakes during stretching. After adding ND, the GF first increased from 3.7 (G-0) to 6.6 (GD-1), but it decreased to 4.4 (GD-5) for a further increase in ND concentration. The behavior of ΔR_{max} and R_0 of G-0 and GDs were understood by analyzing the R_i and the R_c under stretching or releasing based on the structural model. Accordingly, by increasing the crystallinity and adding a low concentration of ND, the strain sensor can achieve high linearity, small hysteresis, and low R_0, as well as improved GF, making it a promising candidate for future applications, such as human motion detection and automated logistics transportation.

By using the mentioned procedure, this study achieved the production of bulk-scale graphene with high crystallinity and a high randomly stacking ratio. Therefore, the obtained graphene is expected to possess excellent electrical and mechanical properties. In addition to the bulk-scale production of this rGO, the potential will be

increasingly explored, particularly in batteries, supercapacitors, conductive ink, shielding effect, organic contaminant removal, and so on.

Reference

[1] A. Ambrosi, C.K. Chua, N.M. Latiff, A.H. Loo, et al., Graphene and its electrochemistry - an update, Chemical Society Reviews 45 (2016) 2458-2493.

[2] R.R. Nair, P. Blake, A.N. Grigorenko, K.S. Novoselov, et al., Fine structure constant defines visual transparency of graphene, Science 320 (2008) 1308.

[3] J. Yang, E. Zhang, X. Li, Y. Zhang, et al., Cellulose/graphene aerogel supported phase change composites with high thermal conductivity and good shape stability for thermal energy storage, Carbon 98 (2016) 50-57.

[4] K.S. Novoselov, V.I. Fal'ko, L. Colombo, P.R. Gellert, et al., A roadmap for graphene, Nature 490 (2012) 192-200.

[5] Z. Xu, S. Nakamura, T. Inoue, Y. Nishina, et al., Bulk-scale synthesis of randomly stacked graphene with high crystallinity, Carbon 185 (2021) 368-375.

[6] C. Lee, X. Wei, J.W. Kysar, J. Hone, Measurement of the elastic properties and intrinsic strength of monolayer graphene, Science 321 (2008) 385-388.

[7] V. Berry, Impermeability of graphene and its applications, Carbon 62 (2013) 1-10.

[8] E.B. Barros, N.S. Demir, A.G. Souza Filho, J. Mendes Filho, et al., Raman spectroscopy of graphitic foams, Physical Review B 71 (2005).

[9] A.C. Ferrari, J.C. Meyer, V. Scardaci, C. Casiraghi, et al., Raman spectrum of graphene and graphene layers, Physical Review Letters 97 (2006) 187401.

[10] K.F. Mak, J. Shan, T.F. Heinz, Electronic Structure of Few-Layer Graphene: Experimental Demonstration of Strong Dependence on Stacking Sequence, Physical Review Letters 104 (2010) 176404.

[11] S. Latil, V. Meunier, L. Henrard, Massless fermions in multilayer graphitic systems with misoriented layers: Ab initio calculations and experimental fingerprints, Physical Review B 76 (2007) 201402.

[12] T. Ohta, A. Bostwick, J.L. McChesney, T. Seyller, et al., Interlayer Interaction and Electronic Screening in Multilayer Graphene Investigated with Angle-Resolved Photoemission Spectroscopy, Physical Review Letters 98 (2007) 206802.

[13] H.-Y. Mi, X. Jing, A.L. Politowicz, E. Chen, et al., Highly compressible ultra-light anisotropic cellulose/graphene aerogel fabricated by bidirectional freeze drying for selective oil absorption, Carbon 132 (2018) 199-209.

[14] H. Liu, M. Dong, W. Huang, J. Gao, et al., Lightweight conductive graphene/thermoplastic polyurethane foams with ultrahigh compressibility for piezoresistive sensing, Journal of Materials Chemistry C 5 (2017) 73-83.

[15] W. Chen, X. Zhang, L. Mi, C. Liu, et al., High-Performance Flexible Freestanding Anode with Hierarchical 3D Carbon-Networks/Fe7 S8 /Graphene for Applicable Sodium-Ion Batteries, Advanced Materials 31 (2019) e1806664.

[16] X. Yu, B. Lu, Z. Xu, Super Long-Life Supercapacitors Based on the Construction of Nanohoneycomb-Like Strongly Coupled CoMoO4 -3D Graphene Hybrid Electrodes, Advanced Materials 26 (2014) 1044-1051.

[17] X.-N. Tang, C.-Z. Liu, X.-R. Chen, Y.-Q. Deng, et al., Graphene aerogel derived by purification-free graphite oxide for high performance supercapacitor electrodes, Carbon 146 (2019) 147-154.

[18] P. Xu, Q. Gao, L. Ma, Z. Li, et al., A high surface area N-doped holey graphene aerogel with low charge transfer resistance as high performance electrode of non-flammable thermostable supercapacitors, Carbon 149 (2019) 452-461.

[19] L.Q. Tao, D.Y. Wang, H. Tian, Z.Y. Ju, et al., Self-adapted and tunable graphene strain sensors for detecting both subtle and large human motions, Nanoscale 9 (2017) 8266-8273.

[20] B. Wen, M. Cao, M. Lu, W. Cao, et al., Reduced Graphene Oxides: Light-Weight and High-Efficiency Electromagnetic Interference Shielding at Elevated Temperatures, Advanced Materials 26 (2014) 3484-3489.

[21] P.D. Xue, C. Chen, D.F. Diao, Ultra-sensitive flexible strain sensor based on graphene nanocrystallite carbon film with wrinkle structures, Carbon 147 (2019) 227-235.

[22] W. Xu, T. Yang, F. Qin, D. Gong, et al., A Sprayed Graphene Pattern-Based Flexible Strain Sensor with High Sensitivity and Fast Response, Sensors (Basel) 19 (2019).

[23] J. Ren, W. Zhang, Y. Wang, Y. Wang, et al., A graphene rheostat for highly durable and stretchable strain sensor, InfoMat 1 (2019) 396-406.

[24] J. Li, S. Zhao, X. Zeng, W. Huang, et al., Highly Stretchable and Sensitive Strain Sensor Based on Facilely Prepared Three-Dimensional Graphene Foam Composite, ACS Applied Materials & Interfaces 8 (2016) 18954-18961.

[25] T. Liu, Y. Yang, S. Cao, R. Xiang, et al., Pore Perforation of Graphene Coupled with In Situ Growth of Co(3) Se(4) for High-Performance Na-Ion Battery, Advanced Materials 35 (2023) e2207752.

[26] L. Wang, H. Yao, F. Chi, J. Yan, et al., Spatial-Interleaving Graphene Supercapacitor with High Area Energy Density and Mechanical Flexibility, ACS Nano 16 (2022) 12813-12821.

[27] W. Li, J. Yan, C. Wang, N. Zhang, et al., Molecule bridged graphene/Ag for highly conductive ink, Science China Materials 65 (2022) 2771-2778.

[28] Y.H. Yeh, K.T. Hsu, C.H. Huang, W.R. Liu, Facile and Green Process to Synthesize a Three-Dimensional Network Few-Layer Graphene/Carbon Nanotube Composite for Electromagnetic Interference Shielding, Polymers (Basel) 14 (2022).

[29] Y. Wang, X. Zhang, X. Ding, Y. Li, et al., Stitching Graphene Sheets with Graphitic Carbon Nitride: Constructing a Highly Thermally Conductive rGO/g-C(3)N(4) Film with Excellent Heating Capability, ACS Applied Materials & Interfaces 13 (2021) 6699-6709.

[30] R. Allgayer, N. Yousefi, N. Tufenkji, Graphene oxide sponge as adsorbent for organic contaminants: comparison with granular activated carbon and influence of water chemistry, Environmental Science: Nano 7 (2020) 2669-2680.

[31] M. Inagaki, Y. Kim, M. Endo, Graphene: preparation and structural perfection, Journal of Materials Chemistry 21 (2011) 3280-3294.

[32] X. Li, J. Shen, C. Wu, K. Wu, Ball-Mill-Exfoliated Graphene: Tunable Electrochemistry and Phenol Sensing, Small 15 (2019) 1805567.

[33] M. Yi, Z. Shen, A review on mechanical exfoliation for the scalable production of graphene, Journal of Materials Chemistry A 3 (2015) 11700-11715.

[34] H.W. Shim, K.-J. Ahn, K. Im, S. Noh, et al., Effect of Hydrophobic Moieties in Water-Soluble Polymers on Physical Exfoliation of Graphene, Macromolecules 48 (2015) 6628-6637.

[35] K. Yoo, Y. Takei, S. Kim, S. Chiashi, et al., Direct physical exfoliation of few-layer graphene from graphite grown on a nickel foil using polydimethylsiloxane with tunable elasticity and adhesion, Nanotechnology 24 (2013) 205302.

[36] C.-M. Seah, S.-P. Chai, A.R. Mohamed, Mechanisms of graphene growth by chemical vapour deposition on transition metals, Carbon 70 (2014) 1-21.

[37] Y. Zhang, L. Zhang, C. Zhou, Review of chemical vapor deposition of graphene and related applications, Physics Reports 46 (2013) 2329-2339.

[38] C. Mattevi, H. Kim, M. Chhowalla, A review of chemical vapour deposition of graphene on copper, Journal of Materials Chemistry 21 (2011) 3324-3334.

[39] W. Liu, H. Li, C. Xu, Y. Khatami, et al., Synthesis of high-quality monolayer and bilayer graphene on copper using chemical vapor deposition, Carbon 49 (2011) 4122-4130.

[40] R.S. Weatherup, B.C. Bayer, R. Blume, C. Baehtz, et al., On the mechanisms of Ni-catalysed graphene chemical vapour deposition, ChemPhysChem 13 (2012) 2544-2549.

[41] K. Al-Shurman, H. Naseem, CVD Graphene growth mechanism on nickel thin films, Proceedings of the 2014 COMSOL Conference in Boston, 2014.

[42] S.J. Rowley-Neale, E.P. Randviir, A.S.A. Dena, C.E. Banks, An overview of recent applications of reduced graphene oxide as a basis of electroanalytical sensing platforms, Applied Materials Today 10 (2018) 218-226.

[43] P. Cui, J. Lee, E. Hwang, H. Lee, One-pot reduction of graphene oxide at subzero temperatures, Chemical Communications 47 (2011) 12370-12372.

[44] S. Mao, H. Pu, J. Chen, Graphene oxide and its reduction: modeling and experimental progress, RSC Advances 2 (2012) 2643-2662.

[45] F. Li, X. Jiang, J. Zhao, S. Zhang, Graphene oxide: A promising nanomaterial for energy and environmental applications, Nano Energy 16 (2015) 488-515.

[46] V. Chabot, D. Higgins, A.P. Yu, X.C. Xiao, et al., A review of graphene and graphene oxide sponge: material synthesis and applications to energy and the environment, Energy & Environmental Science 7 (2014) 1564-1596.

[47] S. Eigler, C. Dotzer, A. Hirsch, Visualization of defect densities in reduced graphene oxide, Carbon 50 (2012) 3666-3673.

[48] R. Rozada, J.I. Paredes, S. Villar-Rodil, A. Martínez-Alonso, et al., Towards full repair of defects in reduced graphene oxide films by two-step graphitization, Nano Research 6 (2013) 216-233.

[49] X. Chen, X. Deng, N.Y. Kim, Y. Wang, et al., Graphitization of graphene oxide films under pressure, Carbon 132 (2018) 294-303.

[50] L. Liu, H. Zhou, R. Cheng, W.J. Yu, et al., High-yield chemical vapor deposition growth of high-quality large-area AB-stacked bilayer graphene, ACS Nano 6 (2012) 8241-8249.

[51] H. Peng, N.B.M. Schroter, J. Yin, H. Wang, et al., Substrate Doping Effect and Unusually Large Angle van Hove Singularity Evolution in Twisted Bi- and Multilayer Graphene, Advanced Materials 29 (2017) 1606741.

[52] N. Richter, Y.R. Hernandez, S. Schweitzer, J.-S. Kim, et al., Robust Two-Dimensional Electronic Properties in Three-Dimensional Microstructures of Rotationally Stacked Turbostratic Graphene, Physical Review Applied 7 (2017) 024022.

[53] B. Hou, R. Xiang, T. Inoue, E. Einarsson, et al., Decomposition of Ethanol and Dimethyl Ether during Chemical Vapor Deposition Synthesis of Single-Walled Carbon Nanotubes, Japanese Journal of Applied Physics 50 (2011) 065101.

[54] T. Ishida, Y. Miyata, Y. Shinoda, Y. Kobayashi, Anomalous restoration of graphitic layers from graphene oxide in ethanol environment at ultrahigh temperature using solar furnace, Applied Physics Express (2016) 025103.

[55] R. Negishi, C. Wei, Y. Yao, Y. Ogawa, et al., Turbostratic Stacking Effect in Multilayer Graphene on the Electrical Transport Properties, Physica status solidi (b) 257 (2019) 1900437.

[56] Y. Li, X. Liu, Z. Zhang, S. Zhao, et al., Adaptive Structured Pickering Emulsions and Porous Materials Based on Cellulose Nanocrystal Surfactants, Angewandte Chemie International Edition 57 (2018) 13560-13564.

[57] T. Saito, S. Kimura, Y. Nishiyama, A. Isogai, Cellulose Nanofibers Prepared by TEMPO-Mediated Oxidation of Native Cellulose, Biomacromolecules 8 (2007) 2485-2491.

[58] R. Xiong, K. Hu, A.M. Grant, R. Ma, et al., Ultrarobust Transparent Cellulose Nanocrystal-Graphene Membranes with High Electrical Conductivity, Advanced Materials 28 (2016) 1501-1509.

[59] Y. Gao, H. Xu, Q. Cheng, Multiple Synergistic Toughening Graphene Nanocomposites through Cadmium Ions and Cellulose Nanocrystals, Advanced Materials Interfaces 5 (2018) 1800145.

[60] Q. Zheng, Z. Cai, Z. Ma, S. Gong, Cellulose Nanofibril/Reduced Graphene Oxide/Carbon Nanotube Hybrid Aerogels for Highly Flexible and All-Solid-State Supercapacitors, ACS Applied Materials & Interfaces 7 (2015) 3263-3271.

[61] K. Abe, H. Yano, Cellulose nanofiber-based hydrogels with high mechanical strength, Cellulose 19 (2012) 1907-1912.

[62] Z.-Y. Wu, C. Li, H.-W. Liang, J.-F. Chen, et al., Ultralight, Flexible, and Fire-Resistant Carbon Nanofiber Aerogels from Bacterial Cellulose, Angewandte Chemie International Edition 52 (2013) 2925-2929.

[63] S. Wang, A. Lu, L. Zhang, Recent advances in regenerated cellulose materials, Progress in Polymer Science 53 (2016) 169-206.

[64] Z. Tang, W. Li, X. Lin, H. Xiao, et al., TEMPO-Oxidized Cellulose with High Degree of Oxidation, Polymers 9 (2017) 421.

[65] A.H. Tayeb, E. Amini, S. Ghasemi, M. Tajvidi, Cellulose Nanomaterials-Binding Properties and Applications: A Review, Molecules 23 (2018) 2684.

[66] M. Sevilla, A.B. Fuertes, Graphitic carbon nanostructures from cellulose, Chemical Physics Letters 490 (2010) 63-68.

[67] D. Jariwala, T.J. Marks, M.C. Hersam, Mixed-dimensional van der Waals heterostructures, Nature Materials 16 (2017) 170-181.

[68] X. Sun, Y. Ding, B. Zhang, R. Huang, et al., New insights into the oxidative dehydrogenation of propane on borate-modified nanodiamond, Chemical communications (Cambridge, England) 51 (2015) 9145-9148.

[69] V. Petrakova, V. Benson, M. Buncek, A. Fiserova, et al., Imaging of transfection and intracellular release of intact, non-labeled DNA using fluorescent nanodiamonds, Nanoscale 8 (2016) 12002-12012.

[70] P. Karami, S. Salkhi Khasraghi, M. Hashemi, S. Rabiei, et al., Polymer/nanodiamond composites - a comprehensive review from synthesis and fabrication to properties and applications, Advances in Colloid and Interface Science 269 (2019) 122-151.

[71] S. Osswald, G. Yushin, V. Mochalin, S.O. Kucheyev, et al., Control of sp2/sp3 carbon ratio and surface chemistry of nanodiamond powders by selective oxidation in air, Journal of the American Chemical Society 128 (2006) 11635-11642.

[72] O. Shenderova, A. Koscheev, N. Zaripov, I. Petrov, et al., Surface Chemistry and Properties of Ozone-Purified Detonation Nanodiamonds, The Journal of Physical Chemistry C 115 (2011) 9827-9837.

[73] I.I. Kulakova, Surface chemistry of nanodiamonds, Physics of the Solid State 46 (2004) 636-643.

[74] X. Duan, Z. Ao, H. Zhang, M. Saunders, et al., Nanodiamonds in sp 2 /sp 3 configuration for radical to nonradical oxidation: Core-shell layer dependence, Applied Catalysis B: Environmental 222 (2018) 176-181.

[75] Z. Xu, T. Inoue, Y. Nishina, Y. Kobayashi, Stacking order reduction in multilayer graphene by inserting nanospacers, Journal of Applied Physics 132 (2022) 174305.

[76] M. Zeiger, N. Jäckel, V.N. Mochalin, V. Presser, Review: carbon onions for electrochemical energy storage, Journal of Materials Chemistry A 4 (2016) 3172-3196.

[77] N. Morimoto, T. Kubo, Y. Nishina, Tailoring the Oxygen Content of Graphite and Reduced Graphene Oxide for Specific Applications, Scientific Reports 6 (2016) 21715.

[78] J.S. Lupoi, E. Gjersing, M.F. Davis, Evaluating Lignocellulosic Biomass, Its Derivatives, and Downstream Products with Raman Spectroscopy, Frontiers in Bioengineering and Biotechnology 3 (2015).

[79] C.C. Moura, R.S. Tare, R.O.C. Oreffo, S. Mahajan, Raman spectroscopy and coherent anti-Stokes Raman scattering imaging: prospective tools for monitoring skeletal cells and skeletal regeneration, Journal of The Royal Society Interface 13 (2016).

[80] H.H. Kim, Endoscopic Raman Spectroscopy for Molecular Fingerprinting of Gastric Cancer: Principle to Implementation, BioMed Research International 2015 (2015) 670121.

[81] S. Stankovich, D.A. Dikin, R.D. Piner, K.A. Kohlhaas, et al., Synthesis of graphene-based nanosheets via chemical reduction of exfoliated graphite oxide, Carbon 45 (2007) 1558-1565.

[82] A.C. Gadelha, D.A.A. Ohlberg, C. Rabelo, E.G.S. Neto, et al., Localization of lattice dynamics in low-angle twisted bilayer graphene, Nature 590 (2021) 405-409.

[83] A. Downes, A. Elfick, Raman Spectroscopy and Related Techniques in Biomedicine, Sensors 10 (2010) 1871-1889.

[84] L.G. Cançado, K. Takai, T. Enoki, M. Endo, et al., Measuring the degree of stacking order in graphite by Raman spectroscopy, Carbon 46 (2008) 272-275.

[85] C. Ni, Scanning Electron Microscopy (SEM), in: Q.J. Wang, Y.-W. Chung (Eds.), Encyclopedia of Tribology, Springer US, Boston, MA, 2013, pp. 2977-2982.

[86] H. Fujimoto, Theoretical X-ray scattering intensity of carbons with turbostratic stacking and AB stacking structures, Carbon 41 (2003) 1585-1592.

[87] V. Uvarov, I. Popov, Metrological characterization of X-ray diffraction methods for determination of crystallite size in nano-scale materials, Materials Characterization 58 (2007) 883-891.

[88] C.V. Stan, C.M. Beavers, M. Kunz, N. Tamura, X-Ray Diffraction under Extreme Conditions at the Advanced Light Source, Quantum Beam Science 2 (2018) 4.

[89] G. Li, G. Hong, D. Dong, W. Song, et al., Multiresponsive Graphene-Aerogel-Directed Phase-Change Smart Fibers, Advanced Materials 30 (2018) e1801754.

[90] W. Choi, I. Lahiri, R. Seelaboyina, Y.S. Kang, Synthesis of Graphene and Its Applications: A Review, Critical Reviews in Solid State and Materials Sciences 35 (2010) 52-71.

[91] M. Zhi, C. Xiang, J. Li, M. Li, et al., Nanostructured carbon-metal oxide composite electrodes for supercapacitors: a review, Nanoscale 5 (2013) 72-88.

[92] Y. Zhang, L. Zhang, C. Zhou, Review of Chemical Vapor Deposition of Graphene and Related Applications, Accounts of Chemical Research 46 (2013) 2329-2339.

[93] N. Yousefi, X. Lu, M. Elimelech, N. Tufenkji, Environmental performance of graphene-based 3D macrostructures, Nature Nanotechnology 14 (2019) 107-119.

[94] D. Wang, A critical review of cellulose-based nanomaterials for water purification in industrial processes, Cellulose 26 (2018) 687-701.

[95] A. Hussain, J. Li, J. Wang, F. Xue, et al., Hybrid Monolith of Graphene/TEMPO-Oxidized Cellulose Nanofiber as Mechanically Robust, Highly Functional, and Recyclable Adsorbent of Methylene Blue Dye, Journal of Nanomaterials 2018 (2018) 1-12.

[96] L.M. Malard, M.A. Pimenta, G. Dresselhaus, M.S. Dresselhaus, Raman spectroscopy in graphene, Physics Reports 473 (2009) 51-87.

[97] A.C. Ferrari, D.M. Basko, Raman spectroscopy as a versatile tool for studying the properties of graphene, Nature Nanotechnology 8 (2013) 235-246.

[98] L.G. Cancado, A. Jorio, E.H. Ferreira, F. Stavale, et al., Quantifying defects in graphene via Raman spectroscopy at different excitation energies, Nano Letters 11 (2011) 3190-3196.

[99] C.Y. Su, Y. Xu, W. Zhang, J. Zhao, et al., Highly efficient restoration of graphitic structure in graphene oxide using alcohol vapors, ACS Nano 4 (2010) 5285-5292.

[100] R. Negishi, M. Akabori, T. Ito, Y. Watanabe, et al., Band-like transport in highly crystalline graphene films from defective graphene oxides, Scientific Reports 6 (2016) 28936.

[101] R. Negishi, H. Hirano, Y. Ohno, K. Maehashi, et al., Layer-by-layer growth of graphene layers on graphene substrates by chemical vapor deposition, Thin Solid Films 519 (2011) 6447-6452.

[102] L. Gustavo Cançado, M. Gomes da Silva, E.H. Martins Ferreira, F. Hof, et al., Disentangling contributions of point and line defects in the Raman spectra of graphene-related materials, 2D Materials 4 (2017) 025039.

[103] T.A. Nguyen, J.U. Lee, D. Yoon, H. Cheong, Excitation energy dependent Raman signatures of ABA- and ABC-stacked few-layer graphene, Scientific Reports 4 (2014) 4630.

[104] K.F. Mak, J. Shan, T.F. Heinz, Electronic structure of few-layer graphene: experimental demonstration of strong dependence on stacking sequence, Physical Review Letters 104 (2010) 176404.

[105] L. Song, F. Khoerunnisa, W. Gao, W. Dou, et al., Effect of high-temperature thermal treatment on the structure and adsorption properties of reduced graphene oxide, Carbon 52 (2013) 608-612.

[106] L. Deng, A.E. Lewandowska, R.J. Young, G. Zhang, et al., Catalytic graphitization of electrospun cellulose nanofibres using silica nanoparticles, Reactive and Functional Polymers 85 (2014) 235-238.

[107] A.A. Balandin, S. Ghosh, W. Bao, I. Calizo, et al., Superior thermal conductivity of single-layer graphene, Nano Letters 8 (2008) 902-907.

[108] D.X. Luong, K.V. Bets, W.A. Algozeeb, M.G. Stanford, et al., Gram-scale bottom-up flash graphene synthesis, Nature 577 (2020) 647-651.

[109] K. Uemura, T. Ikuta, K. Maehashi, Turbostratic stacked CVD graphene for high-performance devices, Japanese Journal of Applied Physics 57 (2018) 030311.

[110] M. Brzhezinskaya, O. Kononenko, V. Matveev, A. Zotov, et al., Engineering of Numerous Moire Superlattices in Twisted Multilayer Graphene for Twistronics and Straintronics Applications, ACS Nano 15 (2021) 12358-12366.

[111] B. Ma, R.D. Rodriguez, A. Ruban, S. Pavlov, et al., The correlation between electrical conductivity and second-order Raman modes of laser-reduced graphene oxide, Physical Chemistry Chemical Physics 21 (2019) 10125-10134.

[112] A. Mohapatra, M.S.R. Rao, M. Jaiswal, Thermal transport in turbostratic multilayer graphene, Carbon 201 (2023) 120-128.

[113] M.A. Pimenta, G. Dresselhaus, M.S. Dresselhaus, L.G. Cancado, et al., Studying disorder in graphite-based systems by Raman spectroscopy, Physical Chemistry Chemical Physics 9 (2007) 1276-1291.

[114] J.K. Mathiesen, R.E. Johnsen, A.S. Blennow, P. Norby, Understanding the structural changes in lithiated graphite through high-resolution operando powder X-ray diffraction, Carbon 153 (2019) 347-354.

[115] P. Dasgupta, On use of pseudo-Voigt profiles in diffraction line broadening analysis, FIZIKA A-ZAGREB- 9 (2000) 61-66.

[116] D. Balzar, H. Ledbetter, Voigt-function modeling in Fourier analysis of size-and strain-broadened X-ray diffraction peaks, Journal of Applied Crystallography 26 (1993) 97-103.

[117] K. Gebresellasie, Investigation of asphalt binders by x-ray diffraction using pearson-vii, pseudo-voigt and generalized fermi functions, Memorial University of Newfoundland, 2012.

[118] S.H. Huh, X-ray diffraction of multi-layer graphenes: Instant measurement and determination of the number of layers, Carbon 78 (2014) 617-621.

[119] C. Hontoria-Lucas, A.J. López-Peinado, J.d.D. López-González, M.L. Rojas-Cervantes, et al., Study of oxygen-containing groups in a series of graphite oxides: Physical and chemical characterization, Carbon 33 (1995) 1585-1592.

[120] H. He, J. Klinowski, M. Forster, A. Lerf, A new structural model for graphite oxide, Chemical Physics Letters 287 (1998) 53-56.

[121] I.K. Moon, J. Lee, R.S. Ruoff, H. Lee, Reduced graphene oxide by chemical graphitization, Nature communications 1 (2010) 73.

[122] N. Gupta, S. Walia, U. Mogera, G.U. Kulkarni, Twist-Dependent Raman and Electron Diffraction Correlations in Twisted Multilayer Graphene, The Journal of Physical Chemistry Letters 11 (2020) 2797-2803.

[123] J.S. Roh, T.H. Choi, T.H. Lee, H.W. Yoon, et al., Understanding Gas Transport Behavior through Few-Layer Graphene Oxide Membranes Controlled by Tortuosity and Interlayer Spacing, The Journal of Physical Chemistry Letters 10 (2019) 7725-7731.

[124] Z. Fan, K. Wang, T. Wei, J. Yan, et al., An environmentally friendly and efficient route for the reduction of graphene oxide by aluminum powder, Carbon 48 (2010) 1686-1689.

[125] X. He, L. Feng, Z. Zhang, X. Hou, et al., High-Performance Multifunctional Carbon-Silicon Carbide Composites with Strengthened Reduced Graphene Oxide, ACS Nano 15 (2021) 2880-2892.

[126] K. Kanishka, H. De Silva, H.-H. Huang, S. Suzuki, et al., Rapid and scalable fabrication of reduced graphene oxide conducting films by ethanol-assisted thermal annealing of graphene oxide, Japanese Journal of Applied Physics 58 (2019) SIIB07.

[127] H. Liu, H. Zhang, W. Han, H. Lin, et al., 3D printed flexible strain sensors: from printing to devices and signals, Advanced Materials 33 (2021) 2004782.

[128] W. Shen, R. Yan, L. Xu, G. Tang, et al., Application study on FBG sensor applied to hull structural health monitoring, Optik 126 (2015) 1499-1504.

[129] D. Maurya, S. Khaleghian, R. Sriramdas, P. Kumar, et al., 3D printed graphene-based self-powered strain sensors for smart tires in autonomous vehicles, Nature communications 11 (2020) 5392.

[130] G. Ge, W. Huang, J. Shao, X. Dong, Recent progress of flexible and wearable strain sensors for human-motion monitoring, Journal of Semiconductors 39 (2018) 011012.

[131] Y. Wang, L. Wang, T. Yang, X. Li, et al., Wearable and highly sensitive graphene strain sensors for human motion monitoring, Advanced Functional Materials 24 (2014) 4666-4670.

[132] A. Qiu, P. Li, Z. Yang, Y. Yao, et al., A path beyond metal and silicon: polymer/nanomaterial composites for stretchable strain sensors, Advanced Functional Materials 29 (2019) 1806306.

[133] J. Park, I. You, S. Shin, U. Jeong, Material approaches to stretchable strain sensors, ChemPhysChem 16 (2015) 1155-1163.

[134] M. Chao, Y. Wang, D. Ma, X. Wu, et al., Wearable MXene nanocomposites-based strain sensor with tile-like stacked hierarchical microstructure for broad-range ultrasensitive sensing, Nano Energy 78 (2020) 105187.

[135] Y. Lu, M.C. Biswas, Z. Guo, J.-W. Jeon, et al., Recent developments in bio-monitoring via advanced polymer nanocomposite-based wearable strain sensors, Biosensors and bioelectronics 123 (2019) 167-177.

[136] H. Hosseini, M. Kokabi, S.M. Mousavi, BC/rGO conductive nanocomposite aerogel as a strain sensor, Polymer 137 (2018) 82-96.

[137] X. Zhao, L. Xu, Q. Chen, Q. Peng, et al., Highly conductive multifunctional rGO/CNT hybrid sponge for electromagnetic wave shielding and strain sensor, Advanced Materials Technologies 4 (2019) 1900443.

[138] W. Obitayo, T. Liu, A Review: Carbon Nanotube-Based Piezoresistive Strain Sensors, Journal of Sensors 2012 (2012) 652438.

[139] Y. Cai, J. Shen, Z. Dai, X. Zang, et al., Extraordinarily Stretchable All-Carbon Collaborative Nanoarchitectures for Epidermal Sensors, Advanced Materials 29 (2017) 1606411.

[140] P. Zhang, Y. Chen, Y. Li, Y. Zhang, et al., A flexible strain sensor based on the porous structure of a carbon black/carbon nanotube conducting network for human motion detection, Sensors 20 (2020) 1154.

[141] L. Lu, X. Wei, Y. Zhang, G. Zheng, et al., A flexible and self-formed sandwich structure strain sensor based on AgNW decorated electrospun fibrous mats with excellent sensing capability and good oxidation inhibition properties, Journal of Materials Chemistry C 5 (2017) 7035-7042.

[142] G.-S. Liu, F. Yang, J. Xu, Y. Kong, et al., Ultrasonically patterning silver nanowire–acrylate composite for highly sensitive and transparent strain sensors based on parallel cracks, ACS Applied Materials & Interfaces 12 (2020) 47729-47738.

[143] Y. Gao, F. Guo, P. Cao, J. Liu, et al., Winding-locked carbon nanotubes/polymer nanofibers helical yarn for ultrastretchable conductor and strain sensor, ACS Nano 14 (2020) 3442-3450.

[144] Y.-J. Kim, J.Y. Cha, H. Ham, H. Huh, et al., Preparation of piezoresistive nano smart hybrid material based on graphene, Current Applied Physics 11 (2011) S350-S352.

[145] J. Lv, C. Kong, C. Yang, L. Yin, et al., Wearable, stable, highly sensitive hydrogel–graphene strain sensors, Beilstein Journal of Nanotechnology 10 (2019) 475-480.

[146] Y. Wang, D. Lu, F. Wang, D. Zhang, et al., A new strategy to prepare carbon nanotube thin film by the combination of top-down and bottom-up approaches, Carbon 161 (2020) 563-569.

[147] T. Yang, X. Jiang, Y. Zhong, X. Zhao, et al., A Wearable and Highly Sensitive Graphene Strain Sensor for Precise Home-Based Pulse Wave Monitoring, ACS Sensors 2 (2017) 967-974.

[148] C. Qian, T. Xiao, Y. Chen, N. Wang, et al., 3D Printed Reduced Graphene Oxide/Elastomer Resin Composite with Structural Modulated Sensitivity for Flexible Strain Sensor, Advanced Engineering Materials 24 (2021) 2101068.

[149] Y. Liu, Q. Shi, C. Hou, Q. Zhang, et al., Versatile mechanically strong and highly conductive chemically converted graphene aerogels, Carbon 125 (2017) 352-359.

[150] S. Chun, Y. Choi, W. Park, All-graphene strain sensor on soft substrate, Carbon 116 (2017) 753-759.

[151] A. Mehmood, N.M. Mubarak, M. Khalid, R. Walvekar, et al., Graphene based nanomaterials for strain sensor application—a review, Journal of Environmental Chemical Engineering 8 (2020) 103743.

[152] J. Huang, H. Wang, J.-a. Li, S. Zhang, et al., High-Performance Flexible Capacitive Proximity and Pressure Sensors with Spiral Electrodes for Continuous Human–Machine Interaction, ACS Materials Letters 4 (2022) 2261-2272.

[153] Y.-G. Kim, J.-H. Song, S. Hong, S.-H. Ahn, Piezoelectric strain sensor with high sensitivity and high stretchability based on kirigami design cutting, npj Flexible Electronics 6 (2022) 52.

[154] Y.V. Skrypnyk, V.M. Loktev, Electrical conductivity in graphene with point defects, Physical Review B 82 (2010) 085436.

[155] T.M. Radchenko, A.A. Shylau, I.V. Zozoulenko, Conductivity of epitaxial and CVD graphene with correlated line defects, Solid State Communications 195 (2014) 88-94.

[156] F. Su, G. Chen, P. Huang, Lubricating performances of graphene oxide and onion-like carbon as water-based lubricant additives for smooth and sand-blasted steel discs, Friction 8 (2020) 47-57.

[157] J. Xu, X. Chen, P. Grützmacher, A. Rosenkranz, et al., Tribochemical behaviors of onion-like carbon films as high-performance solid lubricants with variable interfacial nanostructures, ACS Applied Materials & Interfaces 11 (2019) 25535-25546.

[158] A. Vindhyasarumi, K.P. Anjali, A.S. Sethulekshmi, J. S Jayan, et al., A comprehensive review on recent progress in carbon nano-onion based polymer nanocomposites, European Polymer Journal 194 (2023) 112143.

[159] K.N. Kudin, B. Ozbas, H.C. Schniepp, R.K. Prud'homme, et al., Raman Spectra of Graphite Oxide and Functionalized Graphene Sheets, Nano Letters 8 (2008) 36-41.

[160] Y. Pang, H. Tian, L. Tao, Y. Li, et al., Flexible, Highly Sensitive, and Wearable Pressure and Strain Sensors with Graphene Porous Network Structure, ACS Applied Materials & Interfaces 8 (2016) 26458-26462.

[161] C. Yan, J. Wang, W. Kang, M. Cui, et al., Highly Stretchable Piezoresistive Graphene–Nanocellulose Nanopaper for Strain Sensors, Advanced Materials 26 (2014) 2022-2027.

[162] Y.R. Jeong, H. Park, S.W. Jin, S.Y. Hong, et al., Highly Stretchable and Sensitive Strain Sensors Using Fragmentized Graphene Foam, Advanced Functional Materials 25 (2015) 4228-4236.

[163] C. Xiong, M. Li, W. Zhao, C. Duan, et al., Flexible N-Doped reduced graphene oxide/carbon Nanotube-MnO2 film as a Multifunctional Material for High-Performance supercapacitors, catalysts and sensors, Journal of Materiomics 6 (2020) 523-531.

[164] D. Du, P. Li, J. Ouyang, Graphene coated nonwoven fabrics as wearable sensors, Journal of Materials Chemistry C 4 (2016) 3224-3230.

[165] H. Chen, L. Lv, J. Zhang, S. Zhang, et al., Enhanced Stretchable and Sensitive Strain Sensor via Controlled Strain Distribution, Nanomaterials 10 (2020) 218.

[166] S. Baloda, Z.A. Ansari, S. Singh, N. Gupta, Development and Analysis of Graphene Nanoplatelets (GNPs)-Based Flexible Strain Sensor for Health Monitoring Applications, IEEE Sensors Journal 20 (2020) 13302-13309.

[167] R. Negishi, Y. Kobayashi, Extraordinary suppression of carrier scattering in large area graphene oxide films, Applied Physics Letters 105 (2014) 253502.

[168] A.B. Kaiser, C. Gómez-Navarro, R.S. Sundaram, M. Burghard, et al., Electrical conduction mechanism in chemically derived graphene monolayers, Nano letters 9 (2009) 1787-1792.

[169] T. Kobayashi, N. Kimura, J. Chi, S. Hirata, et al., Channel-length-dependent field-effect mobility and carrier concentration of reduced graphene oxide thin-film transistors, Small 6 (2010) 1210-1215.

List of Publications:

1. Z. Xu, S. Nakamura, T. Inoue, Y. Nishina, Y. Kobayashi, "Bulk-scale synthesis of randomly stacked graphene with high crystallinity", Carbon, 185(2021)368-375 doi:10.1016/j.carbon.2021.09.034
2. Z. Xu, T. Inoue, Y. Nishina, Y. Kobayashi, Stacking Order Reduction in Multilayer Graphene by Inserting Nanospacers, Journal of Applied Physics 132(2022)174305-1, doi: 10.1063/5.0103826
3. Z. Xu, Y. Himura, Y. Himura, C. Ishiguro, T. Inoue, Y. Nishina, Y. Kobayashi, Improved performance of strain sensors constructed by highly crystalline graphene with nanospacer, Japanese Journal of Applied Physics, submitted.

List of Conferences

International conferences:

1. Z. Xu, C. Ishiguro, A. F. Ibadurrahman, Y. Nishina, Y. Kobayashi, "Electrochemical properties of 3D graphene sponge fabricated from graphene oxide", 20th International Conference on the Science and Application of Nanotubes and Low-Dimensional Materials (NT19), Würzburg, Germany (July, 21-26, 2019). (Poster)
2. Z. Xu, S. Nakamura, Y. Nishina, and Y. Kobayashi, “Scalable synthesis of highly porous nanocarbon materials by ultrahigh temperature process for graphene oxide and cellulose nanofiber composites”, 19th Int. Conf. on the Sci. and Appl. of Nanotubes and Low-dimensional Materials (NT18), Beijing, China

(July 15-20, 2018). (Poster)

Domestic conferences:

First author:

1. 許 梓釗、中村 槙悟、仁科 勇太、小林 慶裕 : “酸化グラフェン・セルロースナノファイバー複合体の超高温処理による高空隙ナノカーボン材料形成”,第65回応用物理学会春季学術講演会（早稲田大学・ベルサール高田馬場、2018年3月17日～20日）. (Oral)

Co-author:

1. Y. Himura, C. Ishiguro, Z. Xu, T. Inoue, Y. Nishina, Y. Kobayashi, "Stretchable strain sensors fabricated using a highly crystalline reduced graphene oxide/carbon nanotube composite", 2022 MRS Fall Meeting, Boston USA, (Nov.27-Dec.2, 2022).
2. 戸田 和輝、比村 優奈、許 梓釗、井ノ上 泰輝、仁科 勇太、小林 慶裕 : “交互滴下法で堆積した酸化グラフェン・スペーサ材料薄膜の熱処理による3次元積層グラフェン形成”, 2022年第83回応用物理学会秋季学術講演会（東北大学河内北キャンパス＆オンライン、2022年9月20-23日）
3. 戸田 和輝、比村 優奈、許 梓釗、井ノ上 泰輝、仁科 勇太、小林 慶裕 : “ 滴下交互堆積法で形成した3次元積層グラフェン複合薄膜におけるカーボンナノチューブ添加効果”。2022年第69回応用物理学会春季学術講演会（青山学院大学相模原キャンパス＆オンライン、2022年3月22-26日）
4. 比村 優奈、石黒 稚可子、許 梓釗、井ノ上 泰輝、仁科 勇太、小林 慶裕 : “ CNT/グラフェン複合体を用いた歪みセンサの構造最適化によるセンサ特性の向上”，2022年第69回応用物理学会春季学術講演会（青山学院大学相模原キャンパス＆オンライン、2022年3月22-26日）

5. 比村 優奈、石黒 稚可子、許 梓釗、井ノ上 泰輝、仁科 勇太、小林 慶裕：“ 高空隙CNT/グラフェン複合体を用いた伸縮性歪みセンサの作製とCNT添加効果の検証”, 21a-P01-5、2021年第82回応用物理学会秋季学術講演会（オンライン、2021年9月21日）
6. 比村 優奈、石黒 稚可子、許 梓釗、井ノ上 泰輝、仁科 勇太、小林 慶裕：“高空隙 CNT/グラフェン複合体を用いた歪みセンサの作製と CNT 添加効果の検証 ”, P-22、応用物理学会関西支部2021年度第1回講演会（オンライン、2021年4月23日）
7. 石黒 稚可子、比村 優奈、許 梓釗、仁科 勇太、井ノ上 泰輝、小林 慶裕：“スポンジ状グラフェンを用いたフレキシブルひずみセンサーの作製とSiCナノ粒子添加効果の検証”,19p-P02-16、2021年第68回応用物理学会春季学術講演会（オンライン、2021年3月16日～19日）
8. Y. Kobayashi, Z. Xu, Y. Nishina, R. Negishi, "Synthesis and characterization of graphene thin film with turbostratic stacking from graphene oxide", Graphene2019, Rome, Italy (June, 25-28, 2019).
9. 石黒 稚可子、許 梓釗、仁科 勇太、小林 慶裕：“セルロースナノファイバー添加によるグラフェン積層構造への影響と熱伝導解析”,10p-PA8-19、２０１９年第66回応用物理学会春季学術講演会（東京工業大学、2019年3月9日～12日）
10. S. Nakamura, Z. Xu, Y. Nishina, Y. Kobayashi, "Scalable synthesis of highly porous graphene with turbostratic stacking by thermal process of graphene oxide sponge", E-MRS 2018 Spring Meeting, Strasbourg France (June 18-22, 2018)

Acknowledgement

I am deeply grateful to have the opportunity to express my sincere appreciation to the individuals who have played significant roles in my academic journey. Their guidance, support, and contributions have been instrumental in shaping my research and personal growth.

I would like to express my sincere gratitude to Professor Kobayashi for his exceptional mentorship and profound academic insights throughout my research journey. His rigorous thinking and vast knowledge have greatly inspired and guided me in my studies. I am truly grateful for the valuable time and effort he dedicated to nurturing my intellectual growth.

I am also deeply thankful to Assistant Professor Inoue for his attentive guidance and enlightening instruction. His extensive knowledge and patient explanations have been instrumental in enhancing my understanding of the subject matter. His unwavering support and invaluable advice have made a significant impact on my research experience.

Furthermore, I wish to express my sincere thanks to Professor Negishi for his guidance in introducing me to experimental techniques. His insightful suggestions during the research process have been irreplaceable. I am grateful for the opportunities he provided me to broaden my practical skills and expand my horizons in the field.

In addition, I would like to express my gratitude to Professor Nishina for providing the rGO materials and offering valuable insights for my research. His guidance and suggestions have been immensely helpful in shaping my work.

Simultaneously, I wish to express my gratitude to the professors of review of my doctoral dissertation and defense for their invaluable comments on the revision, which greatly enhanced its quality.

Moreover, I am grateful for the support of DKS Co. and Nippon Kayaku Co. for providing essential materials that have played a vital role in conducting my experiments effectively.

I would also like to extend my appreciation to my lab members, Mr Faiz, Ms Himura, Ms Ishiguro, Mr Nakamura, and Mr Tsutsumi, who were part of the rGO group.

Together, we engaged in fruitful academic discussions and successfully resolved numerous experimental challenges, significantly contributing to the progress of my research. Additionally, I extend my gratitude to my other lab members, Mr Bruno, Mr Chou, Mr Ding, Mr Hirai, Mr Ikeda, Mr Kato, Mr Kikudo, Mr Kamei, Mr Li, Mr Liu, Ms Maekawa, Mr Maruoka, Mr Minechi, Mr Mizuno, Mr Nakamura, Mr Niimi, Mr Nishikawa, Mr Nishio, Mr Ohata, Mr Sakamoto, Mr Semba, Mr Shimizu, Mr Shen, Mr Suzuki, Ms Tadano, Mr Toda, Dr Wang, Mr Wei, Ms Yao, and Mr Yura, for their collaboration in tackling various experimental and personal challenges together.

I am humbled and grateful to all those who have supported my research and academic development. Their guidance, knowledge sharing, and support have helped me overcome challenges, broaden my horizons, and make significant progress in my field of study. Without their contributions and assistance, my achievements would not have been possible.